UNIVERSITY OF CALIFORNIA,
IRVINE

Microfluidic Single-Cell Analysis from Phenotype to Genotype

DISSERTATION

submitted in partial satisfaction of the requirements
for the degree of

DOCTOR OF PHILOSOPHY

in Biomedical Engineering

by

Xuan Li

Dissertation Committee:
Professor Abraham P. Lee, Chair
Professor H. Kumar Wickramasinghe
Assistant Professor Jered Haun

2019

DEDICATION

To

my parents, Xiangbin Li and Qiuxiang Ma,

in recognition of their unconditional love and unending support.

TABLE OF CONTENTS

	Page
LIST OF FIGURES	vi
LIST OF MOVIES	viii
ACKNOWLEDGMENTS	ix
CURRICULUM VITAE	x
ABSTRACT OF THE DISSERTATION	xii
Chapter 1: INTRODUCTION	1
Chapter 2: HIGH-THROUGHPUT MICROFLUIDIC SINGLE-CELL ARRAYS	8
Background	8
Chip Design and Rationale	9
Chip Fabrication	10
Cell Suspension and Blood Sample Preparation	11
Results and Discussion	12
Trapping efficiency vs. design parameters	12
Single CTC/WBC trapping with simultaneous RBC filtration	14
Scaling up of the microfluidic trapping array	17
Further optimization of the trapping array	18
Chapter 3: SINGLE-CELL METABOLIC IMAGING VIA FLUORESCENCE LIFETIME IMAGING MICROSCOPY (FLIM)	19
Background	19
Limitation of size-based and surface marker-based CTC screening	19
Warburg effect	20
Fluorescence Lifetime Imaging Microscopy (FLIM)	22
Overview of the FLIM-based single-cell phenotypic analysis platform	24
Instrument Set-up for FLIM	25
Results	26
Phasor-FLIM measurement of WBC and leukemia single-cell arrays	26
Differentiate different leukemia cell lines via multiparametric analysis of phasor-FLIM	29

Rapid single leukemia cell screening from leukemia-cell-spiked blood samples via phasor-FLIM imaging of the high-density trapping array 32
Discussion 35
Chapter 4: IN SITU SINGLE-CELL MRNA PROBING 39
Background 39
Materials and Methods 42
Fabrication of the ultra-thin PDMS membrane-sealed single-cell array 42
Fabrication of the modified AFM probe 44
Details of the apparatus 44
Viability assay 45
Primer design 45
Results 46
Design and operating principle of the platform 46
Characterization of the modified AFM probe 47
On-chip trapping of HeLa cells and single-cell mRNA probing 50
On-chip trapping of CTC/WBC mixtures and cell type identification 55
Discussion 58
Chapter 5: SINGLE-CELL GENE TRANSFECTION VIA DROPLET MICROFLUIDICS 60
Background 60
Materials and Methods 63
Chip fabrication and experimental setup 63
Plasmid preparation 63
Lipofection 64
Flow cytometry 65
Setup of the RT–qPCR 65
Numerical simulation 66
Results and Discussion 67
Platform design 67
Chaotic mixing in micro-droplets 69
Cell deformation at the droplet pinch-off 74
Increased transfection efficiency and consistency for suspension cells 75
Targeted knockout of TP53BP1 81

Chapter 6: SINGLE-CELL PAIRING ARRAY FOR CELL-CELL INTERACTION STUDIES 84
Background 84
Design and Working Principle 85
Materials and Methods 88
Chip fabrication 88
Isolation and culture of human monocyte-derived dendritic cells 88
Hydrogel preparation 88
Results and Discussion 89
Single-cell pairing efficiency 89
Cell-pairs in hydrogel compartments 91
Dendritic cell – cancer cell interaction at the single-cell level 92
Further Improvement of the Chip and Experimental Design 95
Chapter 7: CONCLUSION AND FUTURE PERSPECTIVE 97
BIBLIOGRAPHY 102
APPENDIX A. Mathematical Theory of Phasor-FLIM 112
APPENDIX B. Setup and Characterization of *in situ* mRNA Probing 116
APPENDIX C. Supplementary Analysis for Droplet Transfection 119
APPENDIX D. Detailed Description of the Movies 125

LIST OF FIGURES

Page

Figure 1.1 Comparison between bulk analysis and single-cell analysis. 2

Figure 1.2 Central Dogma in the cell. 3

Figure 1.3 A microfluidic chemostat. 5

Figure 2.1 Design of the microfluidic single-cell trapping array. 10

Figure 2.2 Fabrication procedure of the microfluidic single-cell trapping array. 11

Figure 2.3 Design optimization of the microfluidic single-cell trapping array. 13

Figure 2.4 Trapping single CTCs/WBCs with simultaneous RBC filtration. 16

Figure 2.5 High-throughput microfluidic single-cell trapping arrays. 17

Figure 2.6 Single-cell trapping array with the narrow opening at each trapping unit. 18

Figure 3.1 Warburg effect and NADH in OXPHOS. 21

Figure 3.2 Principle of Phasor-FLIM. 23

Figure 3.3 Schematic representation of the integrated platform for phasor-FLIM based rapid and label-free single-leukemia-cell screening in the microfluidic trapping array. 25

Figure 3.4 Phasor-FLIM screening of leukemia cell lines and WBCs. 29

Figure 3.5 Differentiating leukemia cells and WBCs via the multiparametric approach. 31

Figure 3.6 Screening leukemia cells from normal WBCs in the leukemia cell-spiked blood samples via phasor-FLIM imaging of the single-cell trapping array. 34

Figure 4.1 Schematic diagram of the integrated microfluidic mRNA probing platform. 41

Figure 4.2 Fabrication of the ultra-thin PDMS membrane-sealed single-cell array. 44

Figure 4.3 Mechanism of mRNA extraction by DENT. 49

Figure 4.4 *In situ* mRNA extraction by DENT. 54

Figure 4.5 Identifying SK-BR-3 cancer cells from U937 monocytes in the single-cell array by their marker-genes' expression via *in situ* mRNA probing. 58

Figure 5.1 Chip design and working mechanism. 69

Figure 5.2 Improved lipofection efficiency via droplet chaotic advection in the winding channel. 73

Figure 5.3 Cell deformation after experiencing the shear stress when squeezing through the droplet generation pinch-off. 75

Figure 5.4 Transfection efficiency and consistency. 80

Figure 5.5 Targeted knockout of TP53BP1 in K562 cells through the delivery of pLentiCRISPR.v2-sgTP53BP1 plasmid via droplet lipofection. 83

Figure 6.1 Design and structure of the cell-pairing array. 86

Figure 6.2 Operating principle of the cell-pairing array. 87

Figure 6.3 Pairing efficiency of the cell-pairing array. 90

Figure 6.4 Paired cells in GelMA compartments. 91

Figure 6.5 Phasor-FLIM analysis of dendritic cells paired with K562 cells or in single-cell traps. 95

LIST OF MOVIES

		Page
Movie 2.1	Trap 100 HeLa cells in the single-cell array.	13
Movie 2.2	Simultaneous CTC/WBC trapping and RBC filtration.	15
Movie 4.1	*In situ* mRNA probing from a HeLa cell by DENT.	50
Movie 5.1	Co-encapsulation of single K562 cells, cationic lipids, plasmids.	67
Movie 5.2	Chaotic advection of droplets in the winding channel.	67
Movie 5.3	Cell deformation when passing the droplet pinch-off.	74
Movie 5.4	Simulation of the shear stress at the droplet pinch-off.	74

ACKNOWLEDGMENTS

I would like to express the deepest appreciation to my advisor and committee chair, Professor Abraham P. Lee. I always feel inspired by his passion and interest in keep pursuing new discoveries. Dr. Lee has been a great mentor to me. He has provided me with valuable suggestions every time when I encountered research difficulties, and supported me to present my research and interact with expertise in the field in many international conferences. Without Dr. Lee's guidance and support, this dissertation would not have been possible.

I would like to thank my committee members Professor H. Kumar Wickramasinghe and Professor Jered Haun. Dr. Wickramasinghe's profound knowledge in microscopy and nanofabrication has been a great resource for me during I was working on the single-cell mRNA probing project. Dr. Haun's research on microfluidic tissue dissociation and nanomedicine has inspired me to explore the clinical applications of microfluidic single-cell analysis and also precision medicine.

Great thanks to Dr. Dohyun Lee, the former post-doctoral researcher in our group, and now post-doctoral researcher at MIT. We worked together for three years, and he taught me patiently starting from the most basic microfabrication techniques. I respect his solid understanding of microfluidics and intelligent way of thinking. I would also like to thank my collaborators, Dr. Yinglei Tao, Dr. Ning Ma, and Sudhanshu Agrawal. Their knowledge in their research fields enables the successful proceeding of our collaborative projects. We have developed innovative biomedical platforms, and also friendship. In addition, a thank you to all BioMiNT lab members, especially to Dr. Xiaolin Wang, Dr. Tao Yue, Da Zhao, and Mohammad Aghaamoo. It has been great working with them for the past five years, and they have offered me kind help in various aspects of my research.

This research is funded by the joint funding from the National Science Foundation and Dupont Pioneer, under the grant number IIP-1538813. Acknowledgment to Dr. Yue Yun, the lead of Transformational Technologies at Corteva Agriscience (the agricultural division of DowDuPont), who has been a great supporter and industrial board member for this research.

I thank the following publishers for their permission to use copyrighted materials in my published manuscripts: Elsevier (Chapter 2), Royal Society of Chemistry (Chapter 3 and 4), and WILEY-VCH Verlag GmbH & Co. KGaA, Weinheim (Chapter 5). I would also thank all the co-authors of the manuscripts for their permission to include the above-published materials in this dissertation. Thank Springer Nature for the reprint permission of Figure 1.3 and Figure 3.1B, and American Association for the Advancement of Science for the reprint permission of Figure 3.1A.

Last but not least, sincere thanks to my dear parents. They are both the first generation of college students in their families, and it was them who taught me to respect knowledge and cherish the opportunities to learn. I am grateful for their unconditional love and support.

CURRICULUM VITAE

Xuan Li

EDUCATION

Ph.D. in Biomedical Engineering **2019**
University of California, Irvine Irvine, CA

M.S. in Biomedical Engineering **2016**
University of California, Irvine Irvine, CA

B.S. in Bioengineering **2014**
Beihang University Beijing, China

RESEARCH EXPERIENCE

Graduate Student Researcher **2014-2019**
BioMiNT Lab, University of California, Irvine

Undergraduate Researcher **2013-2014**
National Center of Nanoscience and Technology, China

TEACHING EXPERIENCE

Teaching Assistant – BME 260: Microfluidics and Lab-on-a-Chip Spring 2018
Dr. Abraham P. Lee

Teaching Assistant – BME 160: Tissue Engineering Fall 2016
Dr. Timothy L. Downing

JOURNAL PUBLICATIONS

[1] **Xuan Li**, Yinglei Tao, Do-Hyun Lee, H. Kumar Wickramasinghe and Abraham P. Lee. "*In situ* mRNA isolation from a microfluidic single-cell array using an external AFM nanoprobe." *Lab-on-a-Chip*, 2017, **17**, 1635-1644.

[2] Do-Hyun Lee*, **Xuan Li***, Ning Ma, Michelle A. Digman and Abraham P. Lee. "Rapid and label-free identification of single leukemia cells from blood in a high-density microfluidic trapping array by Fluorescence Lifetime Imaging Microscopy." *Lab-on-a-Chip*, 2018, **18**, 1349-1358.

[3] Do-Hyun Lee, **Xuan Li**, Alan Jiang and Abraham P. Lee. "An integrated microfluidic platform for size-selective single-cell trapping of monocytes from blood." *Biomicrofluidics*, 2018, **12**, 054104.

[4] **Xuan Li**, Mohammad Aghaamoo, Shiyue Liu, Do-Hyun Lee and Abraham P. Lee. "Lipoplex-Mediated Single-Cell Transfection via Droplet Microfluidics." *Small*, 2018, **14**, 1802055.

BOOK CHAPTER

[1] **Xuan Li** and Abraham P. Lee. "High-throughput microfluidic single-cell trapping arrays for biomolecular and imaging analysis." *Methods in Cell Biology*, 2018, **148**, 35-50.

PATENT

[1] US. 9862941 Single-Cell Microfluidic Device.

SELECTED CONFERENCE PUBLICATIONS

[1] **X. Li**, Y. Tao, D.H. Lee, H.K. Wickramasinghe and A.P. Lee. "An Integrated Microfluidic Platform for Single-Cell Trapping and mRNA Extraction." The 20th International Conference on Miniaturized Systems for Chemistry and Life Sciences (μTAS 2016), Dublin, Ireland, Oct. 9-13, 2016, pp 110-111.

[2] D.H. Lee, **X. Li**, N. Ma, M.A. Digman and A.P. Lee. "Label-free Screening and Identification of Single Cancer Cells in Blood using Fluorescence Lifetime Imaging." μTAS 2017, Savannah, U.S., Oct. 22-26, 2017, pp 118-119.

[3] **X. Li**, M. Aghaamoo, S. Liu and A.P. Lee. "Lipoplex-Mediated Efficient Single-Cell Transfection via Droplet Microfluidics." μTAS 2017, Savannah, U.S., Oct. 22-26, 2017, pp 918-919.

[4] **X. Li**, K.P. Jitsiripol and A.P. Lee. "A Microfluidic Single-Cell Pairing Array for Studying Cell-Cell Interactions in Isolated Compartments." μTAS 2018, Kaohsiung, Taiwan, Nov. 11-15, 2018, pp 241-242.

ABSTRACT OF THE DISSERTATION

Microfluidic Single-Cell Analysis from Phenotype to Genotype

By

Xuan Li

Doctor of Philosophy in Biomedical Engineering

University of California, Irvine, 2019

Professor Abraham P. Lee, Chair

Single-cell analysis is of critical importance in revealing population heterogeneity, identifying minority sub-populations of interest, as well as discovering unique characteristics of individual cells. Conventional bench-top methods are limited by their high cost, low throughput, and inadequacy in analyzing small amount of material. Microfluidic platforms, on the contrary, work at the scale comparable to cell diameter, and recent advances in microfluidics have made it possible to automate the processing and analysis of single cells in a high-throughput and low-cost manner.

In this dissertation, a system of microfluidic platforms enabling high-throughput single-cell analysis from phenotype to genotype is developed. The system is built upon a microfluidic trapping array for rapid and deterministic single-cell trapping in highly-packed microwells. It is a serpentine channel with microwells arrayed along each row, wherein cells are delivered to the traps sequentially by the horizontal flow and pushed into traps by the perpendicular stream through the gap area at each trap. 1600 microwells are filled within 3

min with a single-cell occupying efficiency > 80%, while smaller cells/debris are filtered out simultaneously.

Two innovative single-cell analyses from phenotype to genotype are established on this single-cell array: live-cell real-time metabolic imaging via fluorescence-lifetime-imaging-microscopy (FLIM), and single-cell mRNA live-probing by dielectrophoretic nanotweezers (DENT). Rapid trapping and identification (both by FLIM and mRNA probing) of single circulating-tumor-cells (CTCs) from blood have been successfully demonstrated. After characterizing the individual trapped cells, in order to edit aberrant genes for the identified cells of interest, a droplet-microfluidic platform has been developed for efficient single-cell transfection (10X higher efficiency for suspension cells compared to the bulk approach). To explore cell-cell interaction at single-cell level, the single-cell array has also been modified into an easy-to-operate cell-pairing array.

As the trapping efficiency is determined by the channel parameter instead of the flow rate, the single-cell array can be integrated with various sample-processing units operating at different flow rates. The presented microfluidic system enables high-throughput single-cell trapping, label-free metabolic imaging, mRNA extraction without cell lysing, efficient gene transfection, and cell-cell interaction analysis. It is expected to have myriad applications in cancer diagnostics, gene therapy, immunology, etc.

CHAPTER 1: INTRODUCTION

There has been substantial evidence showing the existence of cellular heterogeneity within an isogenic or clonal cell population. For instance, a type of chemotherapy may be effective for most cells in the tumor cell population, but there are always cells escaping from the chemotherapy.[1] Another example would be, stem cells isolated from the same niche exhibit heterogeneous fate outcomes in responding to the same differentiation factor.[2] The cell-to-cell variations are caused by complex factors such as genetic drift, transcriptional events, differences in cell development and cell cycles, and the intrinsic stochastic heterogeneity of signaling pathways.[3, 4] Conventional biochemical or molecular analyses are bulk assays in which the average responses of a cell population are measured and analyzed, and as a result, the unique characteristics of individual cells are concealed. The population-average cannot fully represent each individual cell. As single cells represent the fundamental functional units of life, inevitably, a great number of biological and medical questions can only be addressed by the approach of single-cell analysis. Single-cell analysis provides a wealth of information and reveals the complex heterogeneity of cell populations, not only allowing us to interrogate fundamental cellular mechanisms, but also uncovering the stochastic fluctuations among cell populations, making it crucial in biomedical research (Fig. 1.1).

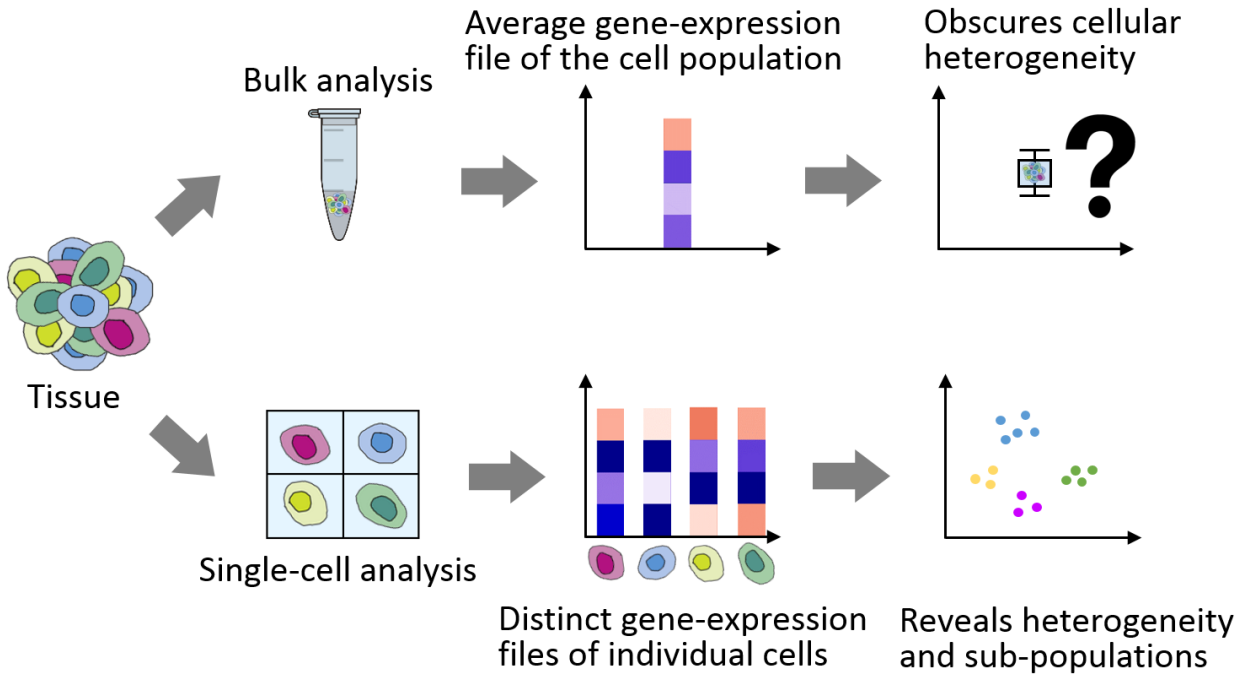

Figure 1.1 Comparison between bulk analysis and single-cell analysis.

Leveraging single-cell analysis, minority sub-populations that are resistant to chemotherapy or have a higher risk of metastasis can be isolated from the heterogeneous tumor cells.[1] Similarly, due to the stochastic effects in the expression level of basal signaling proteins, clonal populations of progenitor cells have diverse differentiation outcomes in response to the same stimuli, which are obscured in bulk assays but are uncovered via analyzing the cell population at the single-cell level.[2] Single-cell analysis also plays an essential role in rare cell-based studies, such as isolating circulating-tumor-cells (CTCs) from peripheral blood cells for cancer diagnostics.[5] CTCs have shown promise as a real-time liquid biopsy to replace conventional tissue biopsies of metastatic tumors for cancer diagnosis, monitoring, and therapeutics.[6] However, CTCs are extremely rare, comprising as few as one cell in a background of 10^9 hematologic cells per milliliter blood of patients with metastatic cancer,[7, 8] and therefore would be masked by the abundant blood cells in bulk

analysis. The isolation and characterization of individual CTCs is of critical importance not only in monitoring intra-tumor heterogeneity, but also in identifying the unique source of the tumor origin.

When analyzing individual cells, the characteristics we can directly observe are their phenotypes, including morphology, metabolic pattern, functional and developmental behaviors, etc. Phenotype is determined by genotype, the genomic makeup of a cell, together with inherited epigenetic factors and non-inherited environmental factors. The information in cells flows according to Central Dogma,[9] from genotype to gene transcription and then protein expression levels, and ultimately results in cellular phenotypes (Fig. 1.2). Phenotypic analyses, e.g., imaging and metabolic assays, are typically straightforward and less-harmful to cells. However, quantitative results are difficult to obtain. Genomic and gene-expression analyses, e.g., sequencing and qPCR (quantitative polymerase chain reaction), provide us quantitative and comprehensive results, but the assay procedures are more complex with advanced instrumentation, and usually require cell lysing. To fully understand cellular mechanisms and heterogeneity, a complete analysis of an individual cell, from its phenotype to genotype, is essential.

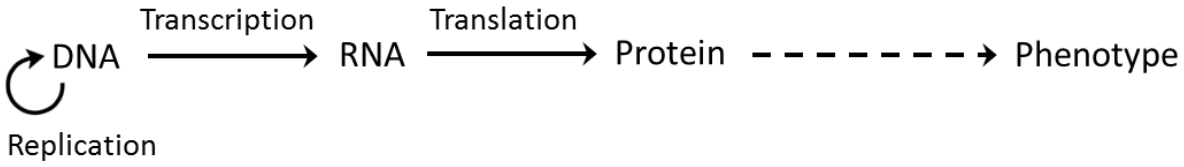

Figure 1.2 Central Dogma in the cell.

Highly sensitive and quantitative detection of multiple components and high throughput analysis of a large number of individual cells remain the key challenges to realize single-cell analysis. Optical tweezers and patch-clamps enable the precise manipulation of

single cells and highly sensitive measurement. However, both methods require high skills to operate and are low-throughput. As it requires the data from a large number of individual cells to draw a statistically meaningful conclusion, high-throughput single-cell processing and analyzing technologies are necessary. One conventional high-throughput approach for single-cell analysis is flow cytometry, which can detect and sort individual cells with desired properties. Nevertheless, flow cytometry does not permit dynamic monitoring of cell response as data are only collected at a single time point. Single-cell sequencing and other molecular level approaches reveal in-depth genomic/transcriptomic information, but with bench-top instrumental setup, they are limited by their high cost, low efficiency, and difficulties in analyzing low amount of starting materials.

Over the past two decades of interdisciplinary research and development, microfluidics has emerged as a power solution overcoming the above limitations of conventional single-cell analysis. What is microfluidics? It is both the science and technology of systems that process or manipulate small ($10^{-9} \sim 10^{-18}$ liters) amounts of fluids, using microminiaturized devices containing channels in microscale.[10] The superiority of microfluidics for single-cell analysis lies in that the channel dimension and sample volume are comparable to the size of a single cell. Therefore, it is more suitable for single-cell handling compared to bench-top instruments. What is more, microfluidic platforms (e.g., Fig. 1.3) require small reagent volumes, which leads to reduced cost, and attains high analysis efficiency because of the scaling law. Multiple microfluidic units of different functions can be integrated on a chip, together with micro-electro-mechanical (MEMS) and optical sensors, so that a micro-total-analysis system (μTas) can be established. As this is like shrinking a laboratory with multiple functional areas down to a chip, microfluidic platforms are also

called ‘lab-on-a-chip’ platforms. With parallelization and automation, microfluidic chips can be scaled up and achieve a high-throughput. A variety of microfluidic platforms have been developed to analyze single cells from phenotype to genotype, such as high-density trapping arrays for single-cell imaging,[11] on-chip single-cell real-time PCR with a whole-process integration,[12] droplet barcode-based single-cell sequencing,[13] and so on.

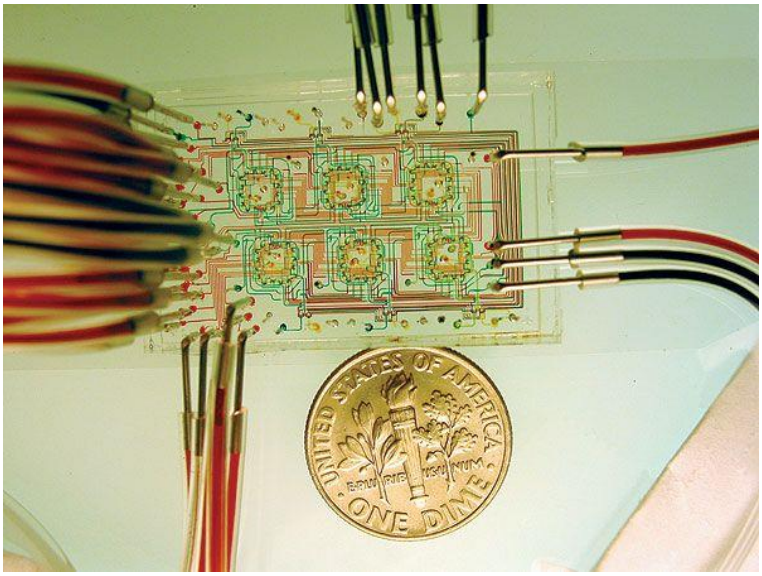

Figure 1.3 A microfluidic chemostat.
An example of microfluidic devices, a microfluidic chemostat for microbial growth analysis with a high density of pneumatic valves. Reprinted with permission from Springer Nature © 2009.

The first step in microfluidic single-cell analysis is the rapid and specific isolation of single cells from a cell population. Although numerous high-performance microfluidic devices have been established for target cell isolation and enrichment, e.g., affinity-based capturing,[14] magnetic isolation,[15] hydrodynamic separation,[16] the sacrifice of purity of recovered cells remains a significant challenge, especially for cells with size overlap to each other. Also, such platforms consist of complicated microfluidic networks and hinder the integration with downstream single-cell characterization techniques. In terms of single-cell analysis, either in the phenotypic level or genotypic level, current mainstream methods, e.g.,

single-cell sequencing,[17] single-cell PCR/RT-qPCR,[12] single-cell transcriptome profiling,[18] single-cell Western Blot,[19] usually require cell lysing and complicated purification procedures. As these methods necessitate destroying the cells, they are not suitable for either comparing the gene expression of single cells before and after external stimulation, or retrieving the stimulated cells for further studies. Last but not least, there is a lack of efficient, safe, and controlled approach for genetically editing the identified single cells of interest. While cationic lipids achieve intracellular DNA delivery without causing genomic disruption or cell damage like viral-vectors or electroporation do, their transfection efficiency, however, is generally not as high. In particular, the lipoplex-mediated transfection (lipofection) efficiency is extremely low for suspension cells such as lymphatic and hematopoietic cells used in immunotherapy.[20, 21] The reported transfection efficiency for suspension cells was typically less than 5% in the literature when following the standard lipofection protocol.[22-26]

Accordingly, this dissertation is set out to develop a system of microfluidic platforms enabling high-throughput single-cell analysis from phenotype to genotype in an easy-to-operate and cell-safe manner. The system is built upon a microfluidic trapping array for rapid and deterministic single-cell trapping in highly-packed microwells. The trapping array consists of 1600 microwells which are filled in less than 3 min with a single-cell occupying efficiency > 80%, and enables rapid trapping of single CTCs and white blood cells (WBCs) with simultaneous filtration of red blood cells (RBCs). As the trapping efficiency is determined by the channel parameter instead of the flow rate, this trapping array can be integrated with different microfluidic sample-processing units operating at different flow rates for various single-cell analyses.

Two innovative and cell-friendly single-cell analyses from phenotype to genotype are established on this single-cell trapping array: live-cell real-time metabolic imaging via fluorescence-lifetime-imaging microscopy (FLIM), and single-cell mRNA live-probing by dielectrophoretic nanotweezers (DENT). Rapid trapping and identification (both by FLIM and mRNA probing) of single CTCs from blood have been successfully demonstrated. After characterizing the individual trapped cells, in order to edit aberrant genes for the identified cells of interest, a droplet-microfluidic platform has been developed for efficient single-cell transfection (10X higher efficiency for suspension cells compared to the bulk approach). To explore cell-cell interaction at single-cell level, the single-cell array has also been modified into an easy-to-operate cell-pairing array.

The presented microfluidic system enables high-throughput single-cell trapping, label-free metabolic imaging, mRNA extraction without cell lysing, efficient gene transfection, and cell-cell interaction analysis. It is expected to have myriad applications in cancer diagnostics, gene therapy, immunology, etc.

CHAPTER 2: HIGH-THROUGHPUT MICROFLUIDIC SINGLE-CELL ARRAYS

Background

The rapid isolation and capturing of single cells is the first step in single-cell analysis, for which a variety of microfluidic platforms have been developed. Droplet microfluidics-based single-cell analysis enables the capturing of single cells in isolated and monodispersed micro-capsules.[27] However, as the droplets keep drifting in the collection pool, it is difficult to track the target cell over time. What is more, the single-cell encapsulation efficiency is relatively low with the majority of droplets being empty due to Poisson distribution. Electric field-based single-cell trapping, e.g., dielectrophoresis (DEP), achieves precise manipulation of individual cells, and single-cell arrays can be established using electrode arrays.[28] Nevertheless, long-time monitoring of the single cells is still not suitable as the exposure in electric field results in potential damage to cell viability and normal functionality. Besides, the fabrication procedure of electrode arrays is complex and requires high expertise. Microfluidic trapping arrays based on physical trapping structures realize single-cell trapping by the passive hydrodynamic force. The physical arrays consist of various designs of microwells with a dimension comparable to the target cell diameter. As the single cells are kept in the microwells by hydrodynamic pressure and physical constrictions, they are locked in fixed positions without active forces which may damage the cell. Therefore, this type of platform is suitable for long-term tracking of the target cells. Di Carlo et al. have demonstrated a single-cell culture array consisting of U-shaped microwells,[29] however, the capturing of single cells was still a stochastic process, in which a large population of cells entered into the microwells randomly. Levario et al. have developed a microfluidic array for

large-scale trapping and orienting of Drosophila embryos,[30] however, it required complex design and the traps were not highly packed. Here we have developed a serpentine-shaped single-cell trapping array in which cells are trapped sequentially and deterministically. The single-cell trapping array is in a highly-packed format, which enables rapid imaging of 100 single cells at the same time. The cell suspension is introduced by a syringe pump in an easy-to-operate manner, and the single-cell occupying efficiency is independent of the flow rate, so that the trapping array can be easily integrated with other microfluidic sample-processing or analyzing units which operate at various flow rates.

Chip Design and Rationale

The design principle of our high-density single-cell trapping array was inspired by Chung et al.[11] For a 100-trap single-cell array, it consists of a 5-row serpentine channel with 20 grooves arrayed along the channel edge of each row (Fig. 2.1A). As illustrated in Fig. 2.1B, for each trapping unit, the height of the trap (h_T) is smaller than the height of the delivery channel (H), resulting in a gap area ($h_G = H - h_T$). The trapping principle relies on the two hydrodynamic flows – the horizontal delivery flow and the perpendicular trapping flow. While cells are delivered to the traps sequentially by the horizontal delivery flow, there is a perpendicular stream flowing through the gap area at each trapping unit, crossing each row of the delivery channel and pushing cells into traps. The width (w) and the length (L_T) of each trap are the same as target cell diameter, so that once a cell occupies a trap, it physically excludes another cell from trapping at the same spot, which ensures that only one cell is trapped at each trapping unit. At the turning zone of each row, there are dummy traps with

L_T smaller than cell diameter, which does not trap cells but helps generate the perpendicular flow for cell focusing.

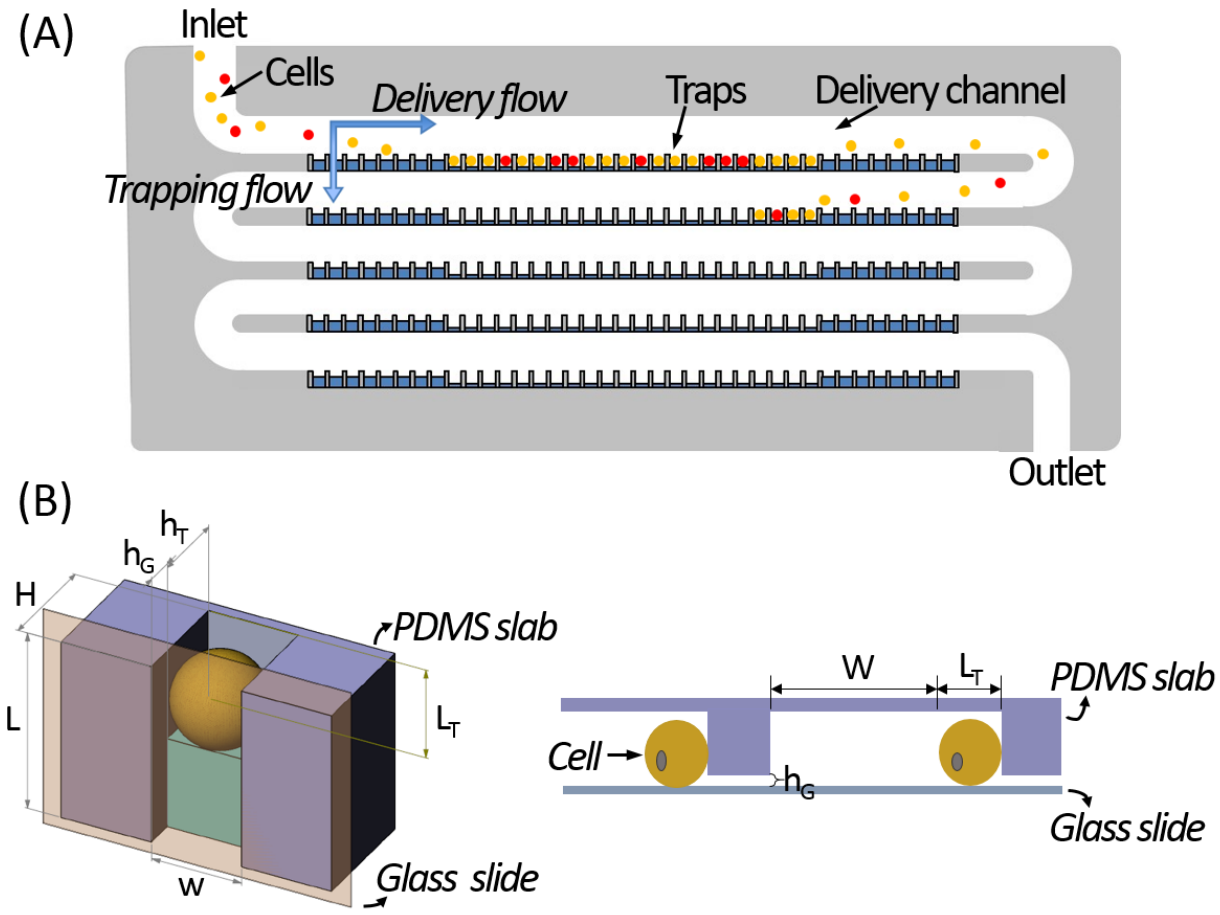

Figure 2.1 Design of the microfluidic single-cell trapping array.
(A) Schematic design of the serpentine-shaped single-cell trapping array, with the delivery flow and the perpendicular trapping flow illustrated by the arrows. (B) The trimetric view (left) and side view (right) of a trapping unit in the array.

Chip Fabrication

The microfluidic trapping array was fabricated in polydimethylsiloxane (PDMS, Sylgard 184, Dow Corning) via soft lithography, and it consisted of a filter region and a serpentine-shaped single-cell trapping channel. A master mold was produced by patterning SU-8 photoresist (MicroChem) on a silicon wafer using standard two-layer photolithography (Fig. 2.2A).

Liquid PDMS mixed with the curing agent (ratio of 10:1) was cast on the mold and cured for 3 hr in a convection oven at 65 °C for complete cross-linking. The PDMS microchannel was then irreversibly sealed with a glass slide after exposure to oxygen plasma for 60 s (Fig. 2.2B).

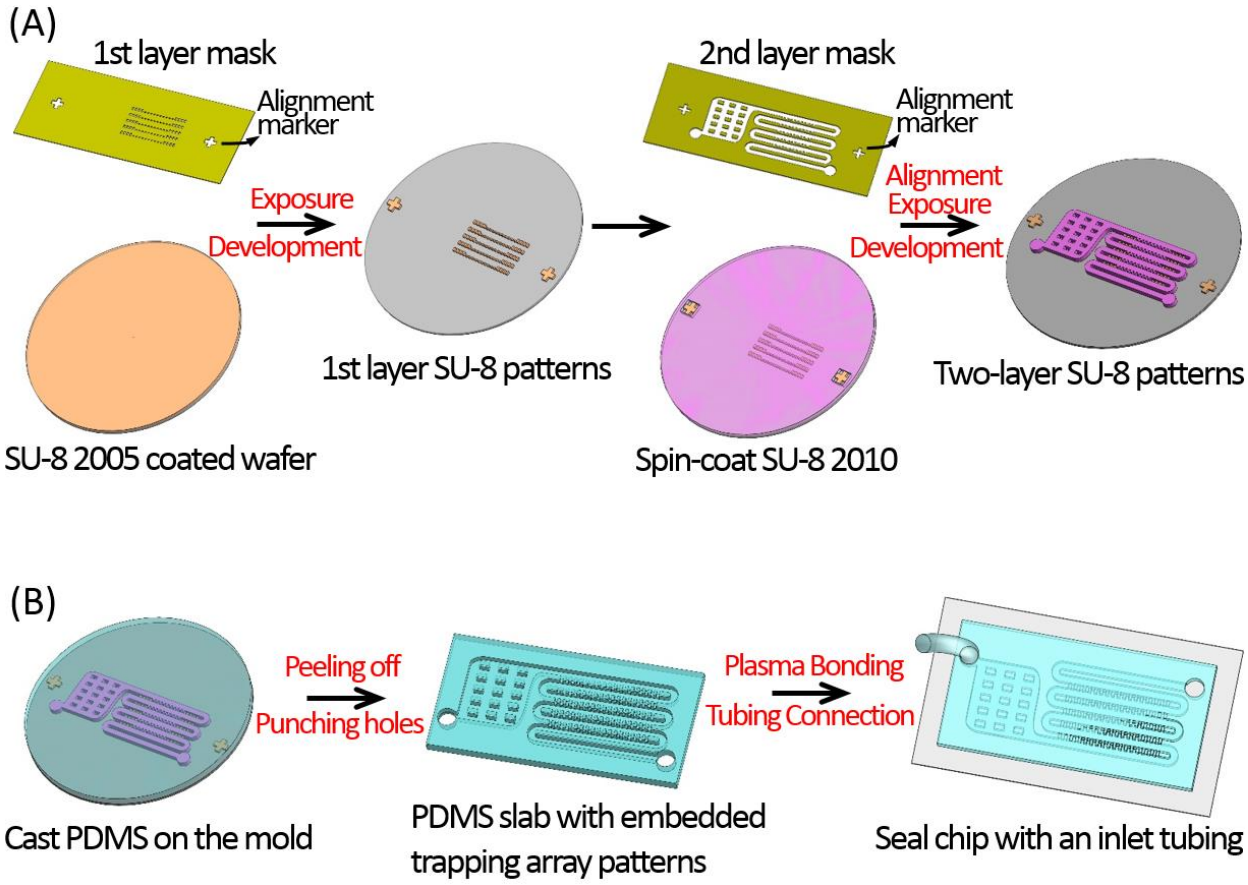

Figure 2.2 Fabrication procedure of the microfluidic single-cell trapping array.
(A) Fabrication of the master mold by two-layer photolithography. (B) Fabrication of the sealed PDMS device by soft-lithography, oxygen plasma bonding, and tubing connection.

Cell Suspension and Blood Sample Preparation

6 different types of cell suspensions were processed by the single-cell analysis platform developed in this thesis. All the cell lines were purchased from American Type Culture Collection (ATCC). HeLa (human adenocarcinoma cell line) cells were cultured in DMEM medium (Gibco) supplemented with 10% fetal bovine serum (FBS, Gibco) and 1%

penicillin/streptomycin (1000 U/mL, Gibco). THP-1 (human acute monocytic leukemia cell line), Jurkat (human acute T cell leukemia cell line), K562 (human chronic myelogenous leukemia cell line), and U937 (human monocyte cell line) cells were cultured in RPMI1640 medium supplemented with 10% FBS. In particular, for THP-1 cells, 0.05 mM 2-mercaptoethanol (Sigma) was added as a metabolic supplement. SK-BR-3 (human breast cancer cell line) cells were cultured in McCoy's 5A medium (ATCC) supplemented with 10% FBS and 1% penicillin/streptomycin. Cells were passaged every 2-3 days following standard protocols and cultured in a humidified incubator at 37 °C with 5% CO_2.

The human blood samples were collected, with informed consent, from healthy donors at UCI General Clinical Research Center with Institutional Review Board (IRB) approval. Vacutainer tubes (BD Bioscience) containing EDTA as an anticoagulant were used for collection.

Results and Discussion

Trapping efficiency vs. design parameters

According to our experimental observation, the single-cell occupying efficiency is not related to the flow rate, but related to the flow resistance ratio of the horizontal flow ($R_{horizontal}$) and the perpendicular flow ($R_{vertical}$), which can be controlled by optimizing the ratio of the delivery channel width (W) to the trap width (w) under the fixed channel height (H) and trap height (h_T). A smaller W/w will lead to more empty traps, while a bigger W/w can cause cell clogging. Based on empirical optimization, a W/w of 4 resulted in the best single-cell occupying efficiency (Fig. 2.3A), which was 94±4% calculated from 12 independent

experiments tested using HeLa cells. For this optimized design, the trap width (w) and length (L_T) were set to be 15 μm (similar to the average cell diameter of HeLa cells), the delivery channel height (H) was 18 μm, the gap height (h_G) was 4 μm, and the delivery channel width (W) was 60 μm (four times of the estimated target cell diameter). The scanning electron microscopic (SEM) image illustrating the detailed structure of a finished single-cell trapping array is shown in Fig. 2.3B. With a HeLa cell concentration of 1×10^6 cells per mL, and a flow rate of 2 μL/min, 100 HeLa cells were trapped sequentially and deterministically (Fig. 2.3C) within 20 s (Movie 2.1).

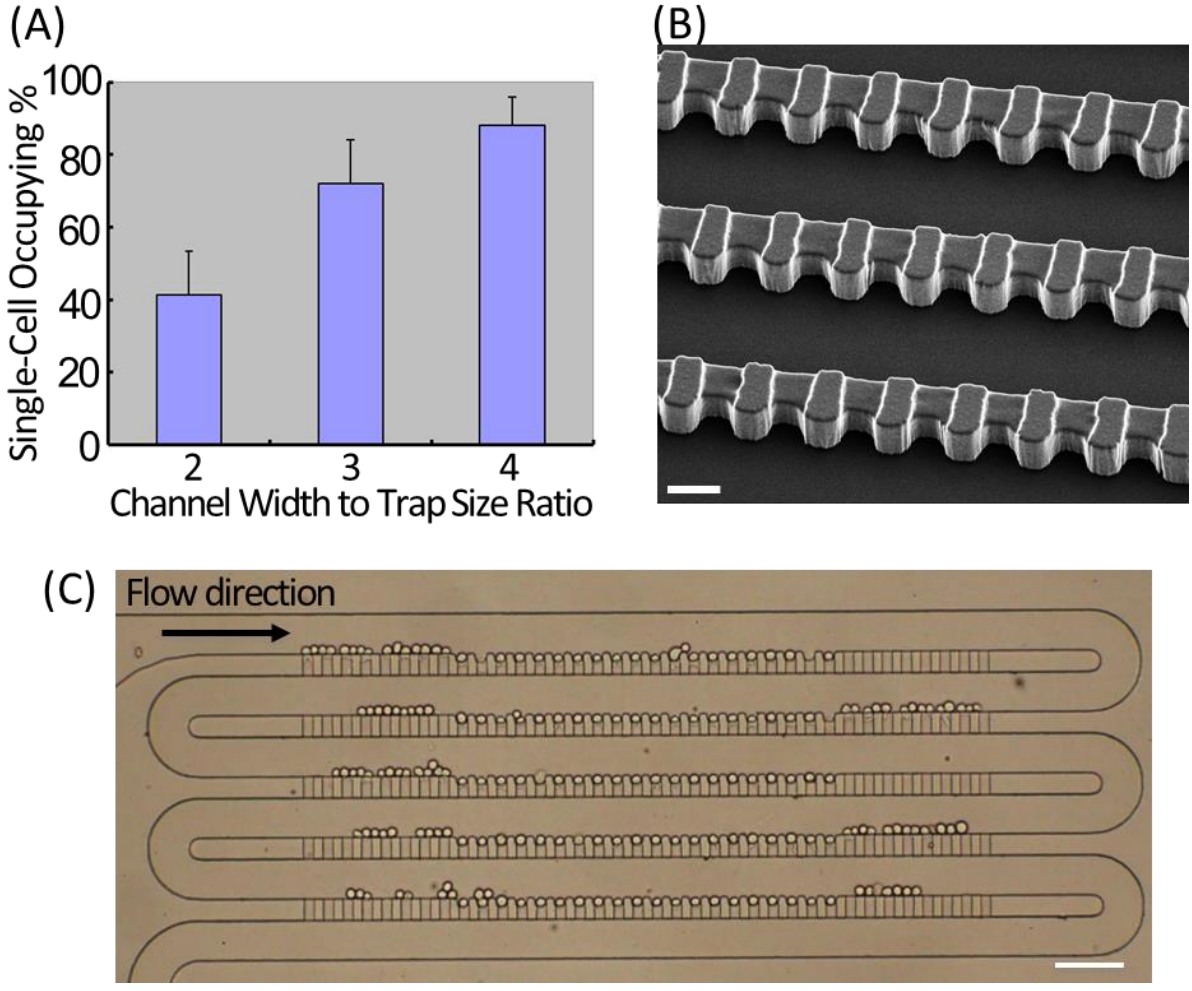

Figure 2.3 Design optimization of the microfluidic single-cell trapping array.
(A) Single-cell occupying efficiency at 3 tested W (delivery channel width) to w (trap width) ratios.

(B) SEM image of the optimized trapping array for 15-μm mammalian cells. Trap width (w) and length (L_T) were 15 μm, the delivery channel height (H) was 18 μm, the gap height (h_G) was 4 μm, and the delivery channel width (W) was 60 μm. Scale bar: 20 μm. (C) Bright-field image of trapping 100 single HeLa cells in the optimized the single-cell trapping array. Scale bar: 100 μm.

Single CTC/WBC trapping with simultaneous RBC filtration

The gap area (h_G) at each trapping unit not only results into the perpendicular flow pushing cells into the traps, but also deforms and migrates smaller cells to pass through the trapping array and continuously filtered out. For example, normal WBCs and leukemia cells are in the size range of 8 to 20 μm, larger than RBCs which have a disk shape with a diameter of ~6.2–8.2 μm and a thickness at the thickest point of 2–2.5 μm.[31] Therefore, while leukemia cells cannot be separated from WBCs purely by size, RBCs can be successfully filtered out through the microfluidic trapping arrays (Fig. 2.4A). The height of h_G is critical in determining the WBC/leukemia capturing efficiency, as larger h_G leads to WBCs/leukemia cells squeezing through the gap area during RBC filtration, and smaller h_G would prohibit both RBC passing through and WBC/leukemia trapping.

We first tested the percentage of single-cell occupied traps according to different h_G of 0, 1.9, 3.3 and 5.5 μm, respectively (Fig. 2.4B). When h_G was 0, we did not observe any cell trapping within the microwell arrays, as there was no penpendicular flow through the gap area to push the cells into the microwells. When the h_G was much smaller than the RBC diameter (e.g., $h_G \sim 1.9$ μm), RBCs were stuck at the trap and could not migrate through the gap area, resulting in a large number of traps filled with multiple cells. On the contrary, when the h_G was much higher than the RBC diameter and even approaching to the WBC diameter (e.g., $h_G \sim 5.5$ μm), not only RBCs were filtered through the gap area, leukemia cells and WBCs were also squeezed through the gap area instead of being trapped in the microwells. The

optimal h_G found from the experiments was 3.3 μm, with a single-cell trapping efficiency of 73.48% and a complete removal of RBCs in diluted blood samples. Based on these observations, we chose the optimal $h_G \sim 3.3$ μm to operate the chips for WBC/leukemia isolation applications. Fig. 2.4C shows the bright-field microscopic image of trapping WBCs and leukemia cells (K562) in the microwell arrays with $h_G = 3.3$ μm. After turning off the sample flow and introducing PBS, all RBCs were removed toward the outlet and only leukemia cells and WBCs were remained in the microwell arrays (Fig. 2.4D). Whole blood samples need to be diluted before introducing into the trapping array, as cell cloggings and aggregations were observed when testing with un-diluted whole blood samples. There exists a trade-off between the single-cell trapping efficiency with the dilution ratio (Fig. 2.4E), as well as the flow rate (Fig. 2.4F). We chose to introduce 2% hematocrit blood under 0.2 mL/h for implementing both the throughput and the single-cell isolation performance (Movie 2.2).

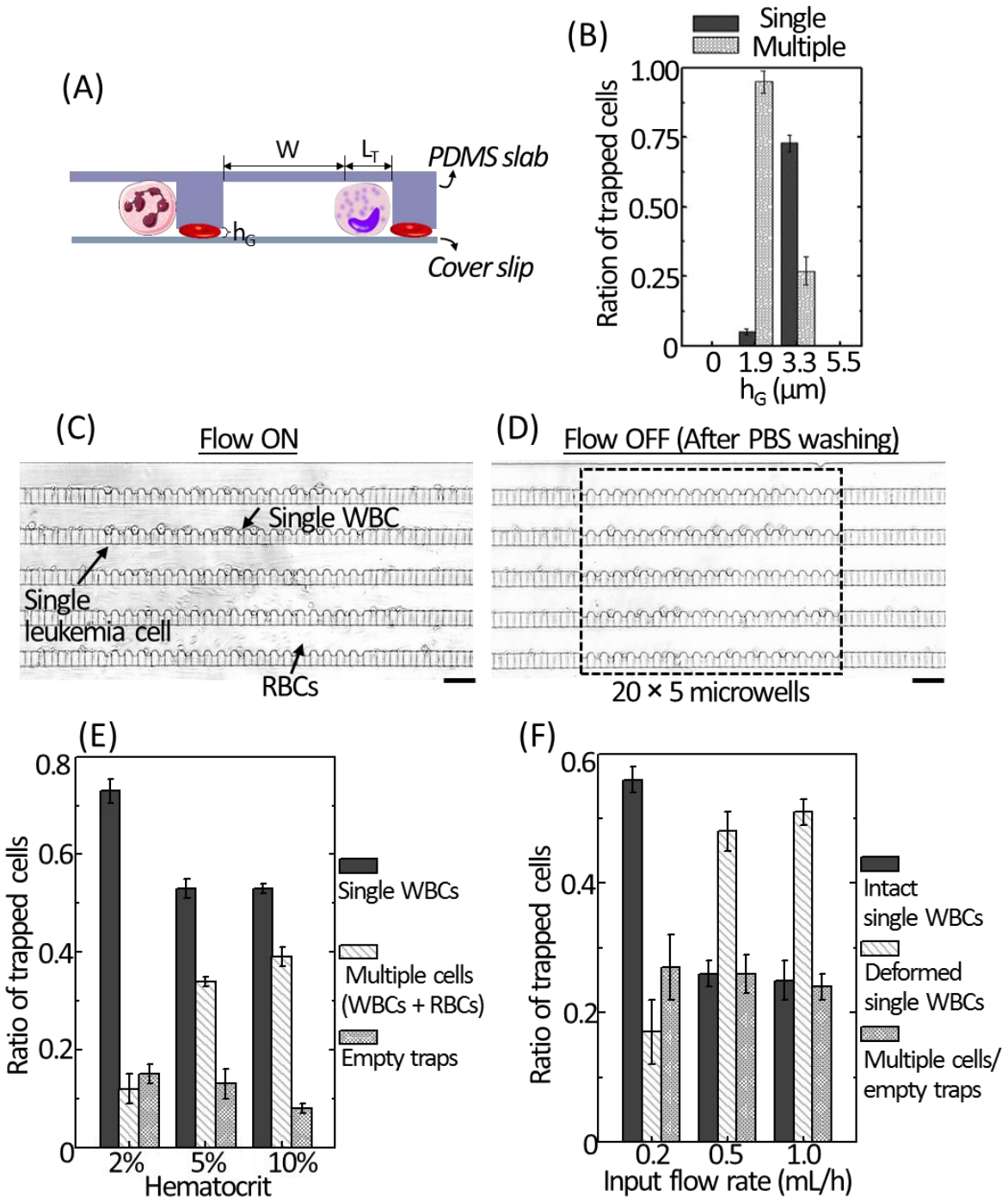

Figure 2.4 Trapping single CTCs/WBCs with simultaneous RBC filtration.
(A) Working principle of single CTC/WBC trapping and RBC filtration. (B) The percentage of the single-cell occupied traps according to different heights of the gap area (h_G), i.e., 0, 1.9, 3.3 and 5.5 μm. (C) Bright-field screen shot during single CTC/WBC trapping of 2% hematocrit blood at 0.2 mL/h input flow rate. (D) Bright-field image of the cell trapping array after washed with PBS. All RBCs were washed out, with only single CTCs/WBCs left in the trapping array. (E) Plot showing the single-cell and multiple-cell occupancies at varying hematocrits. (F) Plot showing the percentages of trapped intact singles, deformed singles and multiple WBCs at varying flow rates. Scale bars: 50 μm.

Scaling up of the microfluidic trapping array

We have scaled up the original 100-trap single-cell array by parallelization to accommodate 16×100 single-cell traps (Fig. 2.5A), which can be filled within 3 min at a flow rate of 0.2 mL/hr. To enable the processing of larger volume samples for high-throughput analysis, a 3-inch chip of 12 channels with 6400 traps each radially arrayed is developed (Fig. 2.5B). This high-throughput version has a single inlet and two ring outlets consisting of 76800 single-cell traps in total, and can be filled within 5 min at a flow rate of 0.3 mL/hr.

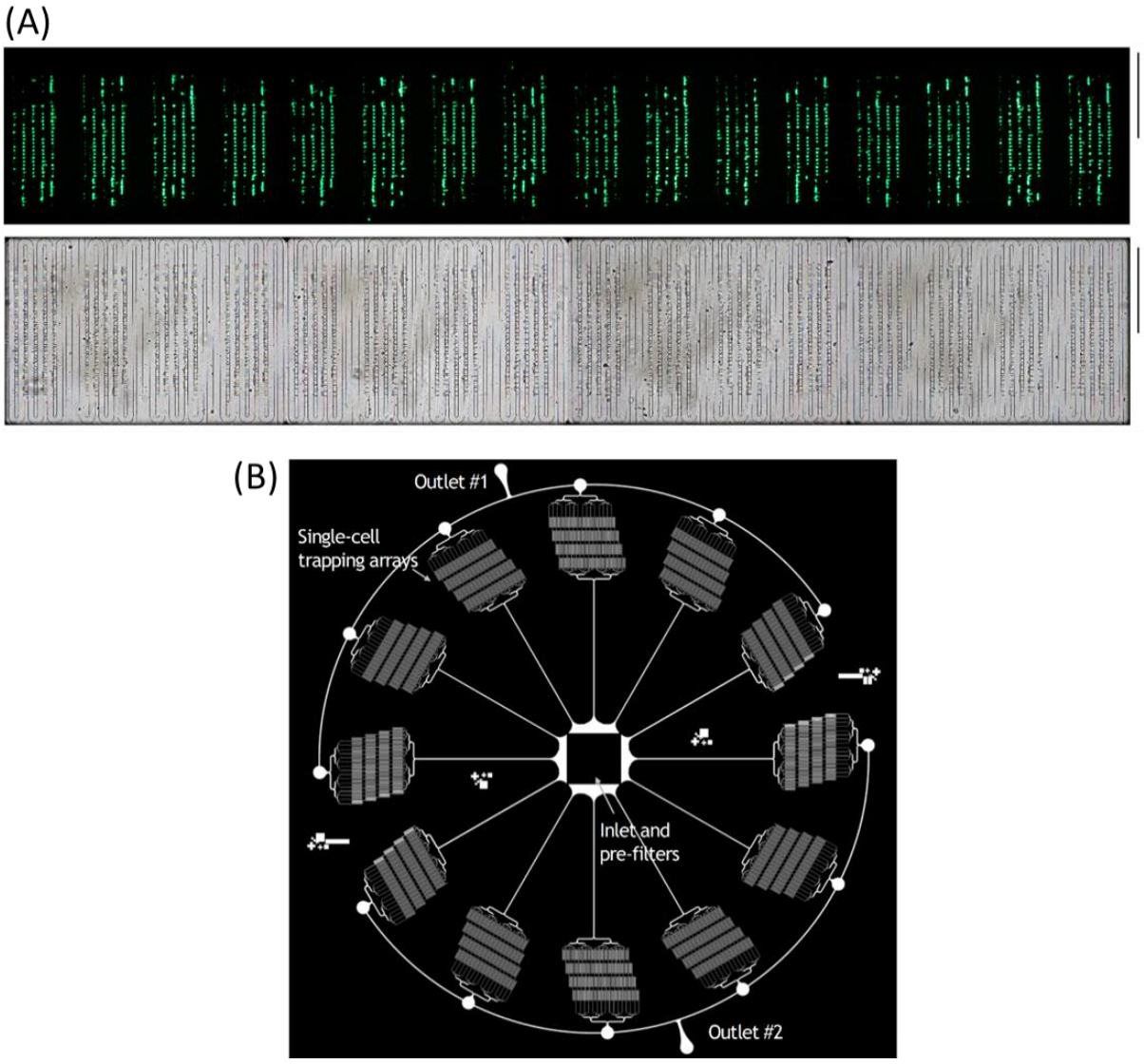

Figure 2.5 High-throughput microfluidic single-cell trapping arrays.
(A) Bright-field (top) and fluorescent (bottom) images of K562 cells trapped in the scaled-up

microfluidic trapping array consisting of 16 identical arrays of highly packed 100 single-cell traps. Scale bar: 1 mm. (B) Schematic illustration of a paralleled device with 12 individual channels radially arrayed with a single inlet and two ring outlets consisting of 76800 single-cell traps in total.

Further optimization of the trapping array

When detaching the single-cell trapping array from the syringe pump upon completion of the cell trapping, the instant back pressure generated when pulling out of the tubing can cause the trapped cells released from the microwells. This situation can be successfully avoided if we wait to pull the tubing out ~10 min after the flow stops. As at this time, the pressure between the syringe pump and the single-cell trapping array reaches equilibrium and the cells start to settle down in the chip. However, the tubing still needs to be pulled out in a gentle manner. One solution to avoid the releasing of trapped cells when pulling the tubing out instantly is to modify the trapping unit with a narrow opening, as illustrated in Fig. 2.6. As mammalian cells have intrinsic deformability, cells can squeeze through the narrow openings into the traps when pushed by the forward flow, and relax back to round shape after enter in. When trapping is completed, cells are locked by the narrow openings, and as a result, the back pressure generated by pulling out the tubing will not lead to cell release.

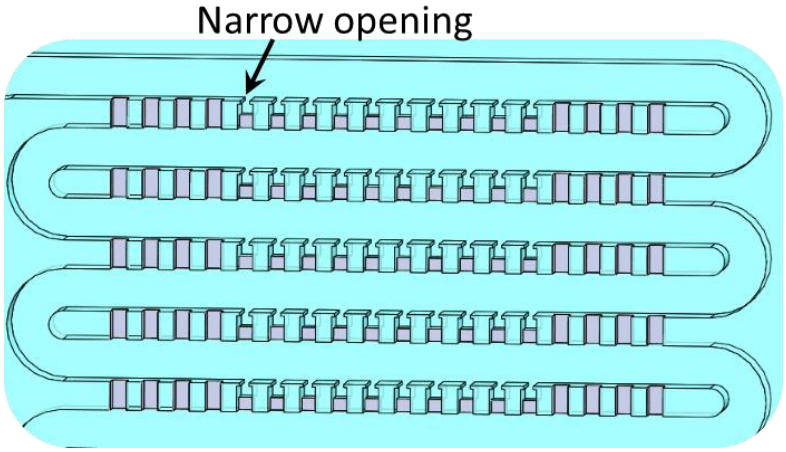

Figure 2.6 Single-cell trapping array with the narrow opening at each trapping unit.

CHAPTER 3: SINGLE-CELL METABOLIC IMAGING VIA FLUORESCENCE LIFETIME IMAGING MICROSCOPY (FLIM)

After single CTCs/WBCs are captured in the highly-packed microfluidic trapping array, the single-cell analysis was established starting from the phenotypic level. The metabolic patterns of the trapped single cells were characterized via a label-free approach, by integrating the trapping array with Fluorescence Lifetime Imaging Microscopy (FLIM).

Background

Limitation of size-based and surface marker-based CTC screening

Microfluidic technology is a powerful tool to process blood samples and isolate CTCs and leukemia cells in a high-throughput, low cost, and portable manner. In fact, a variety of high-performance microfluidic platforms have been established for the isolation and enrichment of CTCs from blood as liquid biopsy, including inertial separation,[32] surface acoustic waves,[33] dielectrophoretic sorting[34] and deterministic chromatography.[35] These techniques are particularly powerful when CTCs have an apparent larger diameter than WBCs. However, in the case of separating leukemia cells from blood, the low purity of recovered leukemia cells remains a significant challenge because the size of leukemia cells exhibit overlap with the size of leukocytes.[36] Alternatively, cancer cells can be sorted based on surface markers expressed predominantly on cancer cells, such as the epithelial cell adhesion molecule (EpCAM). However, the capture efficiency would be heavily dependent on the EpCAM expression level of cancer types and patients.[14, 37] Also, the recovery of biomarker-conjugated cells from the antibody-coated surface induces leukemia cell damage

and requires additional trivial steps for culture and enumeration.[38] Jackson and Li et al. separated the peripheral blood to search for circulating leukemic cells[39] and lymphoblasts[40] within the antibody-immobilized microfluidic channel, respectively, but still needed a time-consuming labeling process and have typically yielded low sample purities (<1%), causing challenges in downstream analysis. To overcome these difficulties in the discrimination and isolation of leukemia cells, the development of label-free technologies to identify and discriminate leukemia cells at a single-cell level has become critical for improving CTC-based diagnosis.[41, 42]

Warburg effect

Apart from morphology and surface markers, another distinct representative for cells' characteristics is their metabolic patterns. And the intrinsic fluorescence of cells generated from endogenous proteins and metabolites enables label-free screening of cancer cells from normal differentiated cells. In 1924, Otto Warburg observed that cancer cells convert glucose by glycolysis regardless of the existence of oxygen.[43] In explanation, differentiated cells like WBCs, mainly rely on oxidative phosphorylation (OXPHOS) in ATP production, whereas cancer cells mainly rely on glycolysis (Fig. 3.1A). Warburg effect is the major metabolic difference between cancer and normal differentiated cells, and there are many pathways behind it. On the one hand, glycolysis generates ATP faster to facilitate rapid tumor cell proliferation; on the other hand, many oncogene mutations up-regulate glycolysis and down-regulate OXPHOS. The reduced form of nicotinamide adenine dinucleotide (NADH) is one of the main coenzymes involved in OXPHOS and glycolysis. As NADH is auto-fluorescent and has emission when excited at 740 nm using two-photon excitation, it is a label-free and cell-

safe marker in reporting metabolic changes associated with cell carcinogenesis and differentiation. The mechanism of NADH-based cell state differentiation is that, as NADH binds to NADH-dehydrogenase only in OXPHOS instead of glycolysis (Fig. 3.1B),[44] cancer cells have a higher ratio of free/enzyme-bound NADH compared to normal differentiated cells as cancer cells mainly rely on glycolysis instead of OXPHOS.

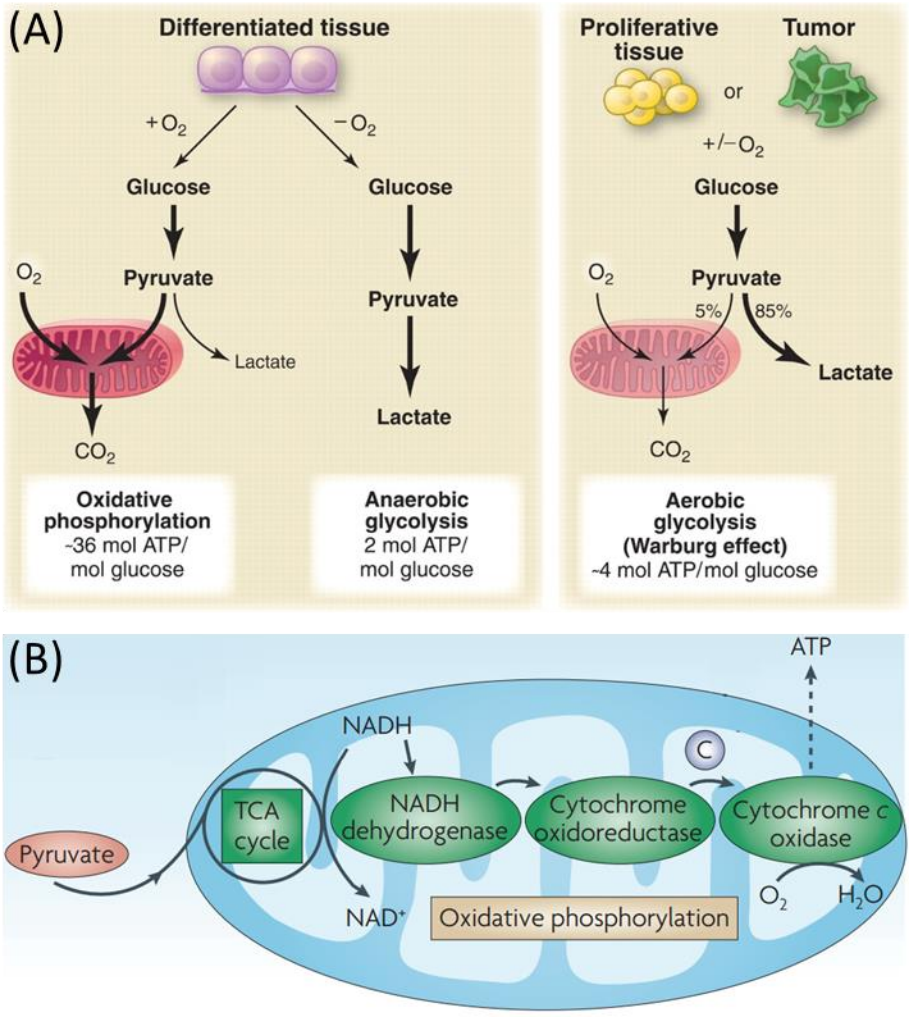

Figure 3.1 Warburg effect and NADH in OXPHOS.
(A) Schematic explanation of the Warburg effect. In the presence of oxygen, differentiated tissues metabolize glucose by OXPHOS. When oxygen is limiting, cells can metabolize glucose by anaerobic glycolysis and bypassing mitochondrial OXPHOS. Warburg observed that cancer cells tend to convert most glucose via glycolysis regardless of whether oxygen is present (aerobic glycolysis). Reprinted with permission from the American Association for the Advancement of Science © 2009. (B) NADH binds to NADH-dehydrogenase inside the mitochondria during OXPHOS. Reprinted with permission from Springer Nature © 2009.

Fluorescence Lifetime Imaging Microscopy (FLIM)

The widespread adoption of multiphoton fluorescence imaging and microscopy has allowed progressive improvements in label-free and non-invasive detection of cellular metabolism and functional analysis with minimal photo-damage and maximized resolution. Although both free and enzyme-bound NADH have similar emission wavelengths at around 480 ± 60 nm, they have different fluoresce intensity decay times, or we say, fluorescence lifetimes (τ). The emission of every fluorophore undergoes exponential decay in nano-second time range upon excitation (Fig. 3.2A and B), and τ is the time when the intensity reduces to 1/e of the original emission intensity. τ is the unique property of every fluorophore and is independent of concentration. The development of fluorescence lifetime imaging microscopy (FLIM) has enabled precise detection and quantification of different fluorophores. Free NADH has a τ of 3.2 ns, and enzyme-bound NADH has a τ around 0.4 ns depending on the specific structure of the enzyme.[45] Given that cancer cells exhibit increased glycolysis and therefore a higher ratio of free/enzyme-bound NADH compared to normal differentiated cells, single CTCs could be discriminated from normal WBCs by FLIM.

The phasor algorithm (phasor-FLIM) has been established for fluorescence lifetime data analysis allowing straightforward interpretation of live tissue's metabolic patterns regarding their physiological relevant fluorophores.[46] In phasor-FLIM, the fluorescence lifetime information of each pixel in the live tissue's fluorescent image is directly transformed into one point in the phasor plot through Fourier transformation. The sine component of the fluorescence intensity decay curve of that pixel is transformed into its s axis coordinate, and the cosine component is transformed to its g axis coordinate in the phasor plot (Fig. 3.2C and D). The detailed theory and mathematical transformation process

are explained in Appendix A. Free and enzyme-bound NADH locate at different locations in the phasor plot, and a cell is located along the line linking free and enzyme-bound NADH depending on its metabolic status (Fig. 3.2E). Phasor-FLIM is a label-free and fit-free imaging technique, and has been demonstrated to sensitively identify metabolic states of stems cells, normal differentiated cells, and cancer cells both in vitro and in live settings.[47]

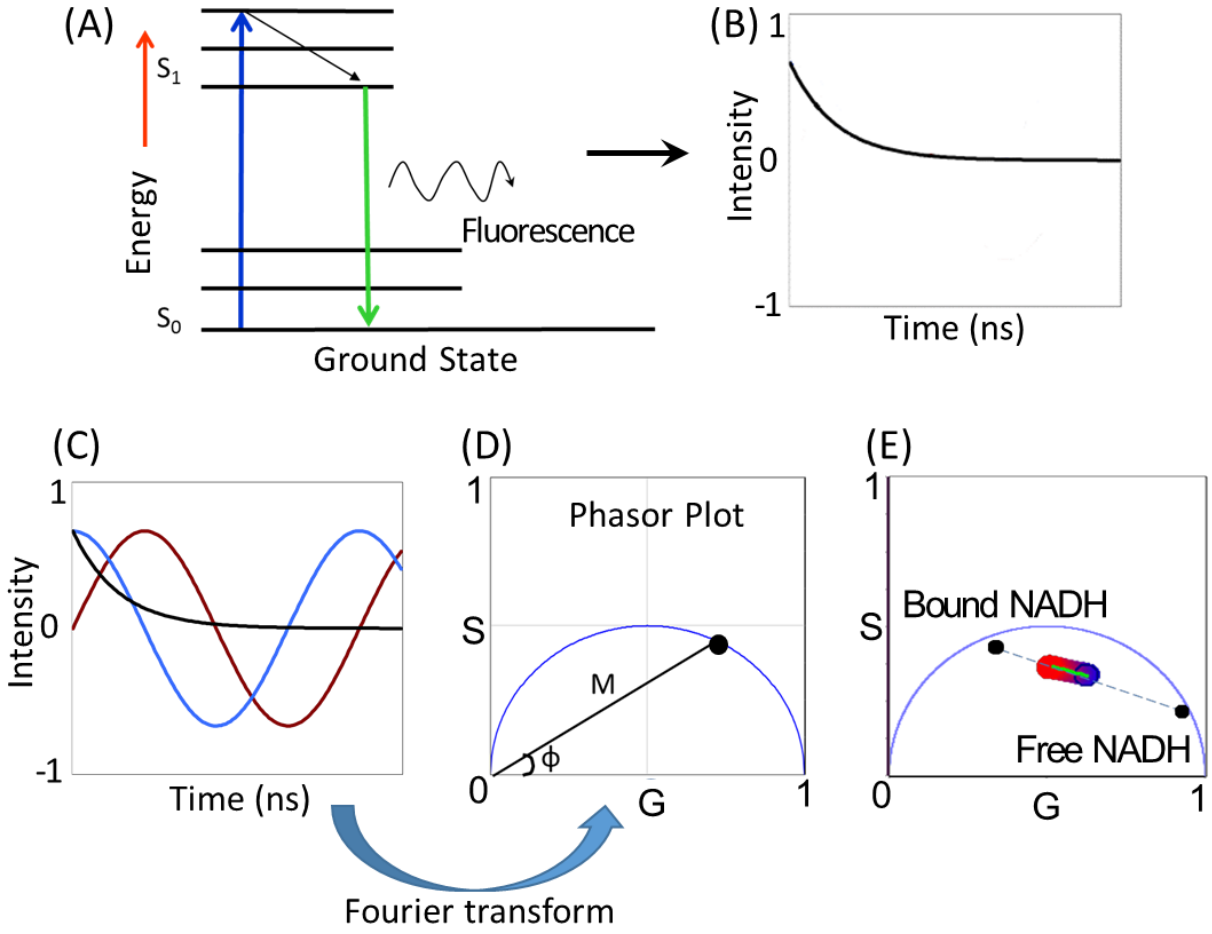

Figure 3.2 Principle of Phasor-FLIM.
(A) Mechanism of the excitation/emission of a fluorophore. (B) The fluorescence emission intensity of a fluorophore undergoes exponential decay in nanosecond time scale. (C) The exponential decay curve can be Fourier transformed into one point in the phasor plot shown in (D). The sine component corresponds to the S axis in the phasor plot, and the cosine component corresponds to the G axis. (E) Free NADH and enzyme-bound NADH have different auto-fluorescence lifetimes and are located at different positions in the phasor plot. A cell is located in the line connecting these two points depending on its free/bound NADH ratio.

Overview of the FLIM-based single-cell phenotypic analysis platform

As illustrated in Fig. 3.3, in this thesis, phasor-FLIM is adopted to characterize cells in the single-cell array, so that to screen CTCs from normal WBCs based on their metabolic differences, in a rapid, label-free, and noninvasive manner for liquid biopsy-based diagnosis. Leukemia cell-spiked blood sample is used to demonstrate the feasibility of this integrated platform. The blood sample is first processed via a microfluidic trapping array with 1,600 traps that are filled within 3 min. Thereafter, upon FLIM imaging, each endogenous fluorescence lifetime signature can be distinguished by its distinct location in the phasor plot. We have demonstrated that the quantification of free versus bound NADH of isolated single cells presents an opportunity to functionally distinguish metabolically active leukemia cells from normal WBCs in blood. With the combination of single-cell microfluidic trapping and phasor-FLIM, this integrated platform achieves high-throughput screening at single-cell resolution based on NADH auto-fluorescence, enabling the detection of metabolically active leukemia cells compared to normal WBCs. To quantify the differences between lifetime distributions of each cell type, we established a multiparametric analysis as described in Ranjit et al.,[48] which compared between the two spectra comprised of the phasor histogram and distribution calculated from leukemia cells and normal WBCs for quantitative separation and statistical calculation. To the best of our knowledge, the presented platform is the first to realize high-density single-cell trapping with simultaneous RBC filtering and to achieve rapid label-free screening of single leukemia cells through non-invasive metabolic imaging. Compared to conventional biochemical or biomolecular-based diagnostics, the phasor-FLIM based screening opens up new opportunities of using metabolic imaging for in-vitro

diagnostics, which overcomes the limitation of complicated sample processing, high-cost, and cytotoxicity.

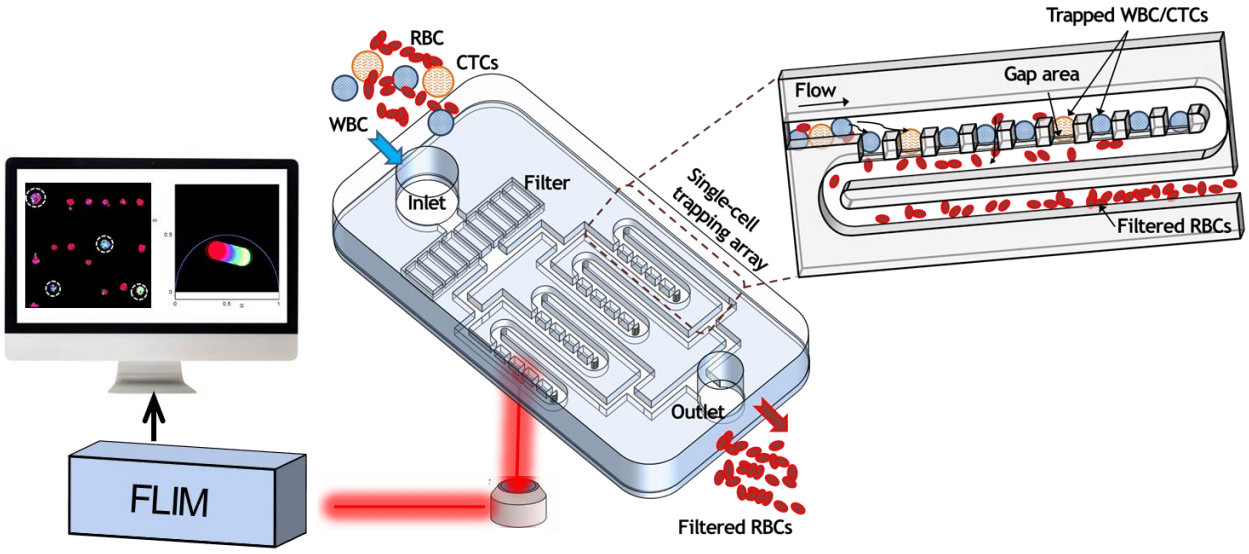

Figure 3.3 Schematic representation of the integrated platform for phasor-FLIM based rapid and label-free single-leukemia-cell screening in the microfluidic trapping array.

Instrument Set-up for FLIM

Fluorescence lifetime images of the WBC/leukemia single-cell arrays were acquired utilizing a Zeiss LSM710 microscope coupled with a Ti:Sapphire laser system (Mai Tai Spectra-Physics, Newport, CA) and an ISS A320 FastFLIM unit (ISS, Champaign, IL). SimFCS software, developed at the Laboratory of Fluorescence Dynamics (LFD), University of California, Irvine, was used to control the system for FLIM data acquisition. The single-cell array was placed in the 37 °C, 5% CO_2 environment during imaging to ensure cell viability, and was excited via two-photon excitation at a wavelength of 740 nm with a laser power of ~5 mW. A 40 × 1.2 NA oil-immersion objective (Carl Zeiss, Oberkochen, Germany) was used, and a dichroic filter (690 nm) separated the fluorescence signal from the laser light. For FLIM image acquisition, fluorescence was detected by a photomultiplier (H7422P-40;

Hamamatsu) using a bandpass filter of 460/840 nm, which covers the emission wavelength of free and protein-bound NADH. Images in the size of 256 × 256 pixels were acquired at the scan speed of 25.21 μs per pixel, and the scanning was continued until 100 counts in the brightest pixel of the images were collected. FLIM calibration of the system was performed by measuring the known lifetime of Coumarin 6 (Sigma-Aldrich, St. Louis, MO) dissolved in ethanol which has a single exponential decay of 2.5 ns. Typically, the acquisition time of one selected region of interest in the single cell array, which can include as many as 100 single cells, was less than 1 min. The acquired FLIM data of the single-cell array was analyzed in the phasor approach using SimFCS software.

Results

Phasor-FLIM measurement of WBC and leukemia single-cell arrays

Single cells of 4 different populations, WBC (Fig. 3.4A), THP-1 (Fig. 3.4B), Jurkat (Fig. 3.4C), and K562 (Fig. 3.4D), were trapped in separate microfluidic single-cell arrays under the input flow rate of 0.2 mL/h, respectively, and were excited via two-photon excitation at 740 nm. The transmission images of the single-cell arrays, the magnified images of the selected regions of interest (ROI), and the NADH auto-fluorescence intensity images of the ROI were shown in Fig. 3 from the panel (i) to (iii). We then applied phasor transformation to the acquired FLIM data and plotted the phasor-FLIM pixel plots of the single-cell arrays as shown in Fig.3 panel (iv). The fluorescence intensity decay at each pixel of the FLIM image was transformed into a single point in the phasor plot (as defined in the Background section), in which the s and g coordinates for every pixel of the image, corresponding to the Fourier sine

and cosine components of the fluorescence decay curve, were plotted on the y and x-axis in the phasor plot where the x coordinate spans from 0 to 1 and the y spans from 0 to 0.5. Based on the pure chemical phasor fingerprints and the linear combination rule,[49] signatures of the trapped single WBCs and leukemia cells mainly fall between the signatures of the known intrinsic fluorescence biomarkers excited at this wavelength, free and enzyme-bound forms of NADH, which have a fluorescence lifetime shift from ~0.4 ns at the free stage to 3.2 ns at the bound stage. To further visualize the difference of the phasor-FLIM signatures between different cell populations and the cellular heterogeneity within the same population, we plotted the average s and g values of individual cells of WBC (blue square), Jurkat (orange circle), THP-1 (cyan triangle) and K562 (green diamond) in the scatter diagram of Fig. 3.4E. As shown, the distribution of cell phasors of the WBCs is significantly different from the group of leukemia cells. A comparison of data pairs demonstrated statistically significant differences in cell phasors for each cell types ($p = 3.60 \times 10^{-53}$, Student's t-test, $^*p < 0.05$). Leukemia cells are shifted toward the lower right direction in the phasor plot compared to WBCs, demonstrating a shorter lifetime, and therefore indicating a higher ratio of free to bound NADH. This can be explained by the Warburg effect, in which rapid-proliferating tumor-like cells, i.e., leukemia cells, have stronger glycolysis in glucose metabolism to support fast ATP consumption and biosynthesis of macromolecules, therefore have a higher ratio of free/bound NADH; while differentiated cells such as WBCs have stronger OXPHOS and have a higher bound/free NADH ratio. The phasors of the three leukemia cell lines also show inner-population heterogeneity in the scatter plot.

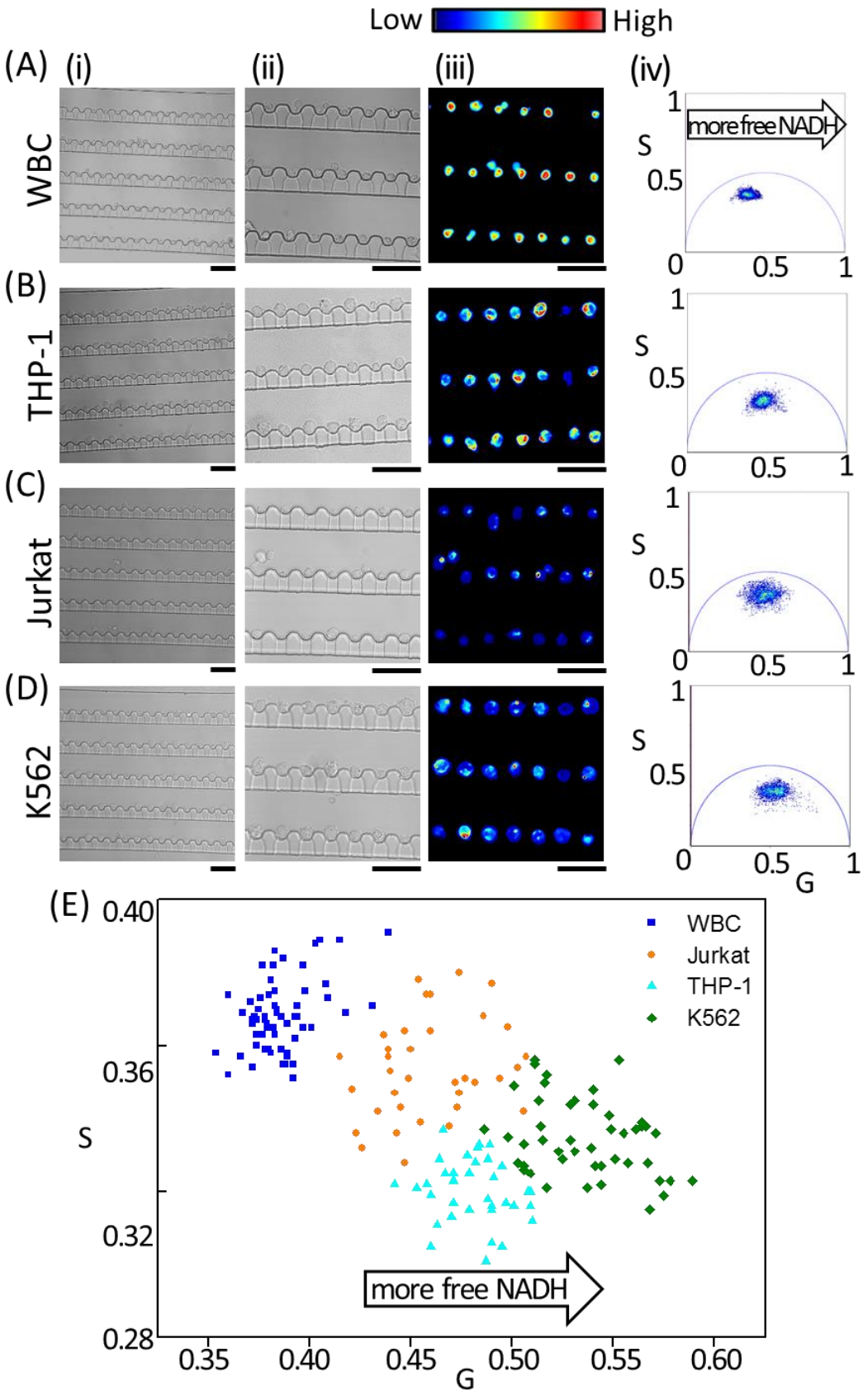
Low
High
(A)
(i)
(ii)
(iii)
(iv)
WBC
more free NADH
S
G
(B)
THP-1
(C)
Jurkat
(D)
K562
(E)
WBC
Jurkat
THP-1
K562
more free NADH
0.40
0.36
0.32
0.28
0.35
0.40
0.45
0.50
0.55
0.60
0
0.5
1

Figure 3.4 Phasor-FLIM screening of leukemia cell lines and WBCs.
(i) Bright-field images, (ii) magnified bright-field images of the selected regions of interest (ROI), (iii) NADH auto-fluorescence emission intensity images, and (iv) corresponding lifetime phasor plots of the single-cell arrays of (A) WBCs, (B) THP-1, (C) Jurkat, and (D) K562 cells. Scale bars: 50 μm. (E) Scatter plot of the g and s phasor values of trapped single cells based on their NADH auto-fluorescence phasor-FLIM signature. A total number of 65 WBCs (blue), 35 THP-1 cells (cyan), 35 Jurkat cells (orange), and 46 K562 cells (green) were measured and plotted. While the heterogeneity between individual cells among the sample population is observed, all the leukemia cells shift towards the right compared to WBCs, indicating a higher free-to-bound NADH ratio and a more glycolytic state.

Differentiate different leukemia cell lines via multiparametric analysis of phasor-FLIM

While the single-cells' average phasor values of 3 types of leukemia cell lines (THP-1, Jurkat, and K562) were located closely in the scatter plot, they can still be quantitatively differentiated by a multiparametric analysis,[48, 50] or we say distance analysis, that splits every cell's phasor points into four equidistance segments based on the height/intensity of the 3D phasor distribution and calculates the average coordinates (g and s) in each segment (Fig. S3). A spectrum of 8 parameters specific to the phasor distribution of each cell is created based on the above, and quantitative separation can be applied to the spectra of two different groups, the control (C) and the test (T). The average spectrum of each group and the deviation of each member from the average are calculated: if the spectrum of an unknown cell is equal to the average of C then the separation index (SI) is equal to −10; if it is equal to the average of T then SI = +10; and if the spectrum is at equal distance from C and T then SI = 0.[48, 50] Cells with a negative or a positive SI value are counted for the control or the test group, respectively, an SI histogram can be plotted based on the number of counts at each SI value. The detailed mathematical explanation of the multiparametric separation is explained in Appendix A. We can also plot the true positive rate against the false positive rate for each separation to get its Receiver-Operating-Characteristic (ROC) curve and calculate the Area-

Under-the-Curve (AUC) value, as a quantitative illustration of the separation's specificity and sensitivity. [48]

As is shown in Fig. 3.5A, three training sets that separate each 2 of the three leukemia cell lines are established using multiparametric analysis of the cell-line specific phasor distributions, with the SI histograms and ROC curves plotted, which can be used as a library for further identification of specific leukemia types in patients' blood. The AUC values of each two comparisons are all higher than 0.950 ($AUC_{THP\text{-}1\text{-}Jurkat}$ = 0.957, $AUC_{K562\text{-}THP\text{-}1}$ = 0.981, and $AUC_{K562\text{-}Jurkat}$ = 0.987), suggesting a statistically powerful separation between each of the two leukemia cell lines with sufficient sensitivity and specificity (Fig. 3.5B). Importantly, this classification is performed at the single-cell level rather than as a population metric and across three samples. This multiparametric analysis can also be adopted to broadly separate WBCs from leukemia cells. In Fig. 3.5C, WBCs are considered as the C group, and all three types of leukemia cells are the T group. While the SI of T group is broadly distributed, indicating the heterogeneity of the leukemia cell population, it does not overlap with the SI distribution of WBCs, and the AUC = 1.000, which means that leukemia cell lines can be clearly differentiated from WBCs according to the multiparametric scheme, confirming the scatter plot in Fig. 3e (Fig. 3.5D).

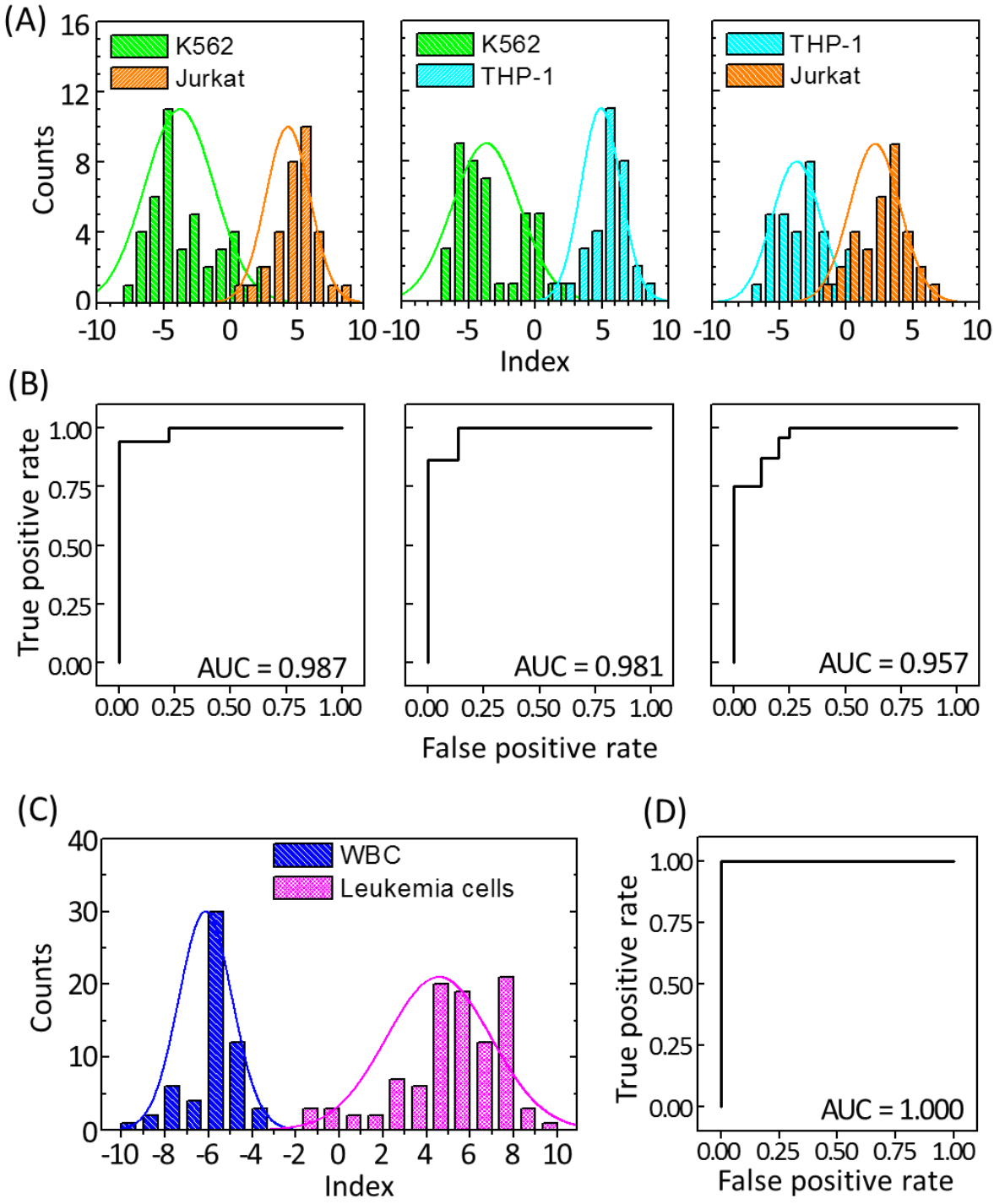

Figure 3.5 Differentiating leukemia cells and WBCs via the multiparametric approach.
(A) The Separation Index (SI) histograms of K562 versus Jurkat (right), K562 versus THP-1 (middle), and THP-1 versus Jurkat (right) demonstrate the efficiency of the multiparametric analysis to distinguish different leukemia cell lines from each other. The SI histogram was plotted based on the number of cell counts against separation index. The SI has a value from −10 to +10. (B) ROC curves constructed by comparing the SI values of two different types of leukemia cells. Values shown here

are the AUC values. (C) The SI histogram of WBCs (blue) and the combined leukemia cell population (red) of THP-1, Jurkat, and K562 cells. (d) ROC curves for the comparison between WBCs and the combined leukemia cell population.

Rapid single leukemia cell screening from leukemia-cell-spiked blood samples via phasor-FLIM imaging of the high-density trapping array

After identification of the difference in the phasor-FLIM fingerprints of single WBCs and leukemia cell lines (THP-1, Jurkat, and K562), we conducted the rapid label-free single leukemia cell screening in leukemia-cell-spiked human blood samples. THP-1, Jurkat, and K562 cells were spiked into human blood at a 1 to 5 ratio to WBCs, separately, in order to mimic the blood sample of patients with different types of leukemia, and the diluted whole blood samples (2% hematocrit) were introduced into the high-density single-cell arrays under the flow rate of 0.3 mL/h (Fig. 3.6(i)). Then we collected the NADH auto-fluorescence emission of trapped single cells (Fig. 3.6(ii)) and the fluorescence lifetime data at 740 nm, two-photon excitation and plotted the lifetime maps (Fig. 3.6(iii)) by 1) linking the higher bound/free-NADH-ratio group (red cursor) and the higher free/bound-NADH-ratio group (green cursor) in the phasor plot of all the trapped single cells (Fig. 3.6D), and 2) color-coding: the color scale from red/pink to white/cyan represents a linear increase of free to protein-bound NADH ratio (Fig. 3.6E).[51] Different types of the spiked single leukemia cells were clearly distinguished from normal WBCs as highlighted in the white-dashed circles in the lifetime maps (Fig. 3.6(iii)), as the spiked leukemia cells had more components in the white and blue color, while normal WBCs consisted of more red and pink color components. The significant shift toward a higher free/bound NADH ratio and shorter lifetime region of leukemia cells compared to WBCs is because the leukemia cells are in a rapid proliferating stage and utilize more glycolysis to facilitate rapid generation of ATP and biosynthesis of

macromolecules, while WBCs use OXPHOS as the major metabolic mechanism to digest glucose more completely but generate ATP slower. Another non-negligible result revealed in the lifetime map is the cell-to-cell heterogeneity among the same population, which represents the unique metabolic pattern of each specific cell, and can be further analyzed to separate sub-populations of interest. For example, subgroups of WBCs, e.g., neutrophils, eosinophils, basophils, lymphocytes, and monocytes, might be able to be differentiated based on their fluorescence patterns via single-cell phasor-FLIM. Apart from color-coding based screening from the lifetime maps, a more quantitative screening of single-leukemia cells can be achieved by loading the phasor-FLIM information to the multiparametric separation training sets that were established in Fig. 4a. As is shown in the SI histogram in Fig. 3.6F, in which the phasor-FLIM signatures of the single cells (dotted white circle) were compared with WBCs (C group) and the combined population of three leukemia cell lines (T group), and all the circled cells were calculated to have positive SI index values, confirming their identity as leukemia cells. Also, different types of spiked leukemia cells have different SI values within the T group, and the type of a potential known leukemia cell can be further identified by loading its information to the training sets of leukemia cell comparison (Fig. 3.5B). As the FLIM data collection of each laser scanning area containing 100 single-cell traps takes less than 1 min, the leukemia cell screening of the total 1,600 traps could be achieved within 16 min.

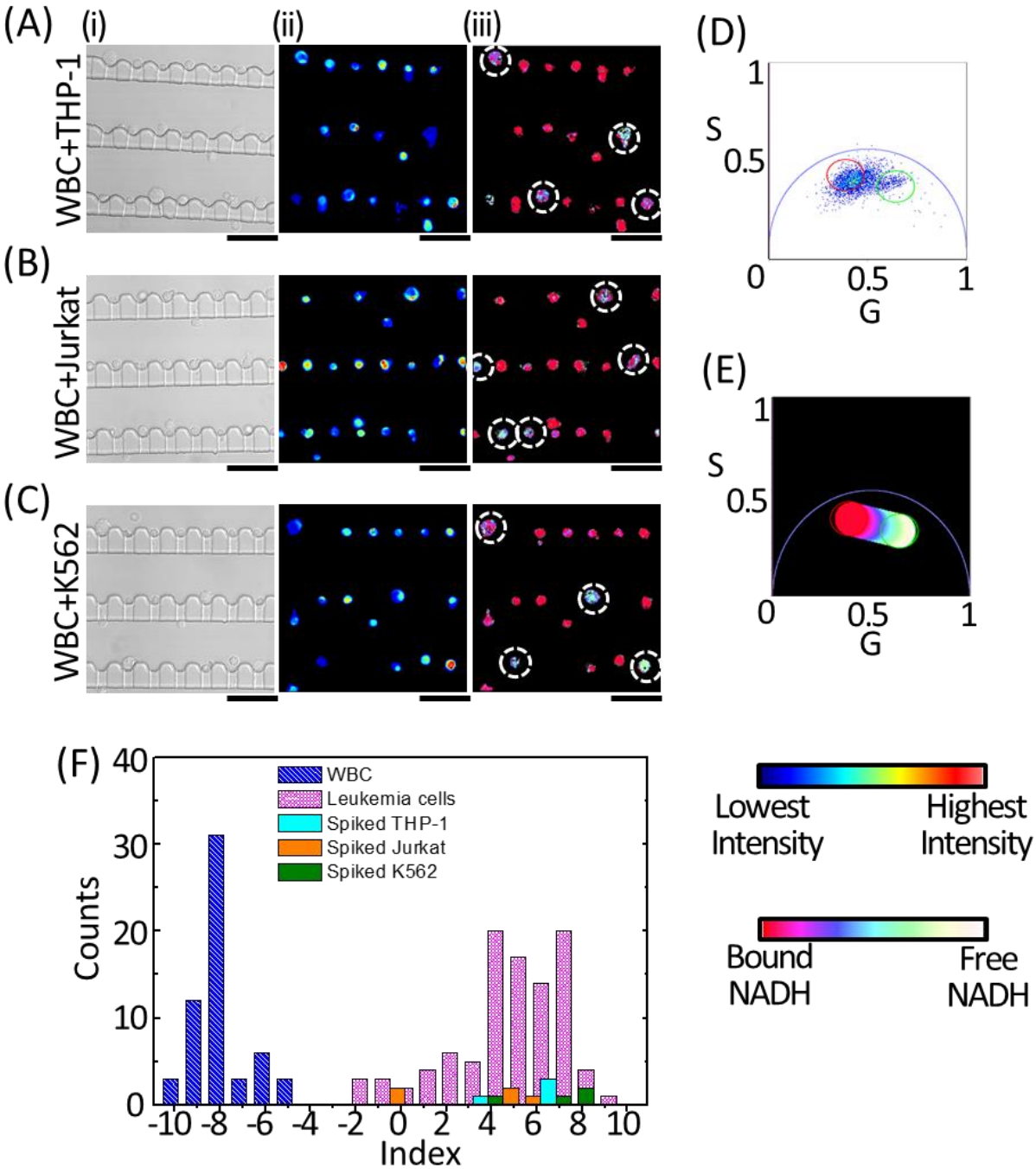

Figure 3.6 Screening leukemia cells from normal WBCs in the leukemia cell-spiked blood samples via phasor-FLIM imaging of the single-cell trapping array.
Panel (i) shows the bright-field images and panel (ii) presents the NADH auto-fluorescence intensity images of the THP-1 (A), Jurkat (B), and K562 (C) cell-spiked blood samples, respectively. The phasor-FLIM information of all the trapped single cells is plotted in (D), where the higher bound/free-NADH-ratio group (red cursor) and the higher free/bound-NADH-ratio group (green cursor) are linked and color-coded: the color scale from red/pink to white/yellow represents a linear increase of free to protein-bound NADH ratio (E). Based on the above, the NADH lifetime maps of the leukemia cell-

spiked blood samples are plotted in panel (iii). Leukemia cells demonstrate a significant shift toward a higher free/bound NADH ratio and shorter lifetime indicating a higher glycolytic state (F). Scale bars: 50 μm.

Discussion

Here we have shown that our microfluidic single-cell phasor-FLIM platform is capable of trapping both leukemia cells and WBCs while filtering out RBCs, and differentiating the similar sized leukemia cells and normal leukocytes by mapping their metabolic fingerprints without any labeling required. The quantitative separation of leukemia cells and WBCs, as well as between different leukemia cell lines, was achieved via the established multi-parametric scheme comparing the 8 parameter-spectra of the phasor-FLIM signatures.

Microfluidic single-cell phasor-FLIM is particularly relevant to the separation of tumor cells from blood where tumor cells may not be easily discriminated from leukocytes based on size alone. Most microfluidic platforms that separate tumor cells from leukocytes based on size differences lose the majority of smaller sized tumor cells, therefore here we chose to not introduce a size bias in leukemia cell trapping, but to rely on the distinct metabolic difference between normal differentiated cells, i.e., WBCs, and rapidly proliferating tumor cells such as leukemia cells. As is shown in Fig. 3.4 and Fig. 3.6, there exists a significant difference in the phasor-FLIM signatures between leukemia cells and WBCs, as leukemia cells have shorter fluorescence lifetime and a higher ratio of free to bound NADH, because of their dependence on glycolysis. Also, quantitative separation is achieved (Fig. 3.5) based on the multiparametric scheme comparing the 8 parameter-spectra of the phasor-FLIM distributions. Both of the above demonstrate that phasor-FLIM based screening is a label-free and robust leukemia cell identification approach, and our platform

is the first demonstration to discriminate single leukemia cells from WBCs using phasor-FLIM based on the difference of free/bound NADH ratio.

This platform could potentially be useful for differentiating single activated or non-activated T cells because recent work claims that the Warburg effect is a key process that assists T cell survival and proliferation after activation, as well as producing the effector cytokines.[43] The stimulation of CD8+ T cells boosts rapid production of reactive oxygen species (ROS) which has its unique fluorescence lifetime signature in the bottom-left portion of the phasor plot.[52] In addition, the activated T cells express a functional phagocyte-type NADPH oxidase, which would shift the FLIM signature towards longer lifetime range.[53] Both of the two aspects lead to a more complex change in FLIM signatures during T cell activation, and should be different from that of tumor cells, which simply shifts towards the shorter lifetime caused by glycolysis. There has been substantial research reporting that leukemic cells are highly glycolytic even though cells reside within the bloodstream which has higher oxygen tension than cells in most normal tissues.[54] To expedite leukemia detection and improve personalized therapy, it is crucial to quickly screen the abnormal leukocytes that might allow determination of effective treatment to be made in real time at the bedside. The presented microfluidic isolation platform based on metabolic imaging has advantages over conventional flow cytometry. Fluorescence-activated cell sorting (FACS) is a representative approach in flow cytometry to categorize heterogeneous samples in a high-throughput manner and is used routinely in clinical diagnosis. But it requires a time and effort consuming process to fluorescently tag cells with expensive antibodies that could potentially lead to irreversible cell damage and change in intrinsic cell properties. In addition, it requires high expenses and needs skilled operating staff. Moreover, the photostability of the fluorophores

with time becomes a critical concern along with the broad emission spectra and narrow excitation range of the fluorescent tags. Also, clinical deployment of single leukemia cell monitoring, on the other hand, would require sampling within minutes. Recent FACS machines allow single-cell retrieval to negate the issue of requiring subsequent characterization of the sorted populations, but still, have a slower throughput than bulk recovery.

The phasor-FLIM signature heterogeneity within the WBC or leukemia cell population is another non-negligible finding which requires further interpretation and is useful in identifying minority sub-populations. As we know, peripheral WBCs consist of several subpopulations such as lymphocytes, monocytes, neutrophils, eosinophils, and basophils. Phenotypic and functional analysis of single peripheral WBCs present valuable clinical information based on their numbers, compositions, and functional responses, for example, (i) the production of interferon gamma (IFN-γ) by T-cells which correlates with the immune response against tuberculosis infection, (ii) bacterial infections often cause an increased neutrophil count, while the increased number of lymphocytes is often due to the viral infections and auto-immune disorders, and (iii) the peripheral blood lymphoblast percentage is an important index for diagnosis and prognosis of acute lymphoblastic leukemia (ALL). Thus the differential counting of WBCs from smaller quantities of blood is crucial for point-of-care diagnosis. Label-free isolation and non-invasive differential discrimination of single leukocytes via phasor-FLIM will facilitate in vitro analysis of immune responses of single WBCs as an alternative of conventional WBC counting and phenotyping.

The existence of a highly tumorigenic subpopulation of leukemia cells, especially leukemic stem cells (LSCs), in heterogeneous tumor mass plays a critical role in tumor

development and metastasis. The presented single-cell phasor-FLIM screening platform could potentially be applicable to screen single LSCs from the tumor population and explore tumor heterogeneity and differential responses to drugs. After phenotyping, the single cells of interest can be cultured within the microfluidic device, or further analyzed *in situ* for genotypic information, or even retrieved from the trapping array upon adapting various techniques such as optical DEP,[55] pipetting,[56] and laser-based manipulation.[57]

CHAPTER 4: IN SITU SINGLE-CELL MRNA PROBING

While FLIM successfully screens single CTCs out based on their metabolic patterns, it does not tells us the unique and specific characteristics of cancer cells at the genotypic level. In this chapter, we dig the information of single cancer cells much deeper, from phenotype to genotype. The mRNA molecules of specific cells in the single-cell trapping array is extracted out *in situ* by a dielectrophoretic nanotweezer (DENT), so that the marker-gene expression of an arbitrary cell is evaluated while maintaining the cell viability.

Background

Rather than simply counting CTCs, the single-cell genotypic analysis reveals in-depth information of cancer cell behavior and heterogeneity according to marker-genes' expressions. However, most of the developed methods, e.g., single-cell sequencing,[17] RNA sequencing,[1] single-cell RT-qPCR[12] and droplet PCR,[58] require cell lysing and complicated purification procedures to isolate genetic materials from the target cells. As these methods necessitate destroying the cells, they are not suitable for either comparing the gene expression of single cells before and after external stimulation, or retrieving the stimulated cells for further studies.

Atomic force microscopy (AFM) has evolved from a near-field microscopy technique to a unique set of tools extensively used for manipulating and characterizing biomolecules with nanometer resolution.[59, 60] In Guillaume-Gentil et al., an AFM probe with a triangular aperture near the apex connected to the microfluidic channels in the cantilever (FluidFM) was developed to withdraw cytoplasmic fluid containing mRNAs from a single cell.[61]

However, as this method was not mRNA specific and a substantial volume of cytoplasmic content needed to be aspirated out to obtain valid RT-qPCR results, many other molecules, e.g., proteins, enzymes, electrolytes, would also be extracted, possibly affecting normal cellular functions. Nawarathna et al. reported a technique capable of extracting mRNA species specifically from a single living cell using an electrode-coated AFM probe.[62] The probe was modified into a tapered coaxial probe that served as a dielectrophoretic nanotweezer (DENT), wherein the application of an alternating-current (AC) field between the inner and outer electrodes of the co-axial cable generated dielectrophoretic (DEP) force to attract various mRNA molecules toward the probe-end. While DENT avoided the removal of cytosol as in FluidFM, but the probing processes were still performed on an opening cell-culture dish, thus the culture media would be prone to evaporation, and cells could be easily contaminated leading to false-positive readings from the surrounding media. If sealed microfluidic systems were incorporated with the single-cell mRNA probing technique, cells would be protected from contamination and evaporation, and leveraging the tremendous upstream sample preparation and downstream analytical capability of microfluidics, the integrated platform will be a powerful tool for various biomedical analyses.

In this chapter, we aim to develop a microfluidic single-cell analysis platform that integrates the high-efficiency single-cell trapping array and with a DENT probe capable of measuring mRNA expression levels of each target living cell (Fig. 4.1). The injected cells flow inside the microchannels and are trapped individually at a rate of 100 single-cell trappings per 20 s, and then a modified AFM probe is controlled mechanically to penetrate through an ultra-thin PDMS membrane to extract mRNAs non-destructively from single target cells. The

extracted mRNA molecules then undergo RT-qPCR to reveal the single-cellular expression levels of target genes.

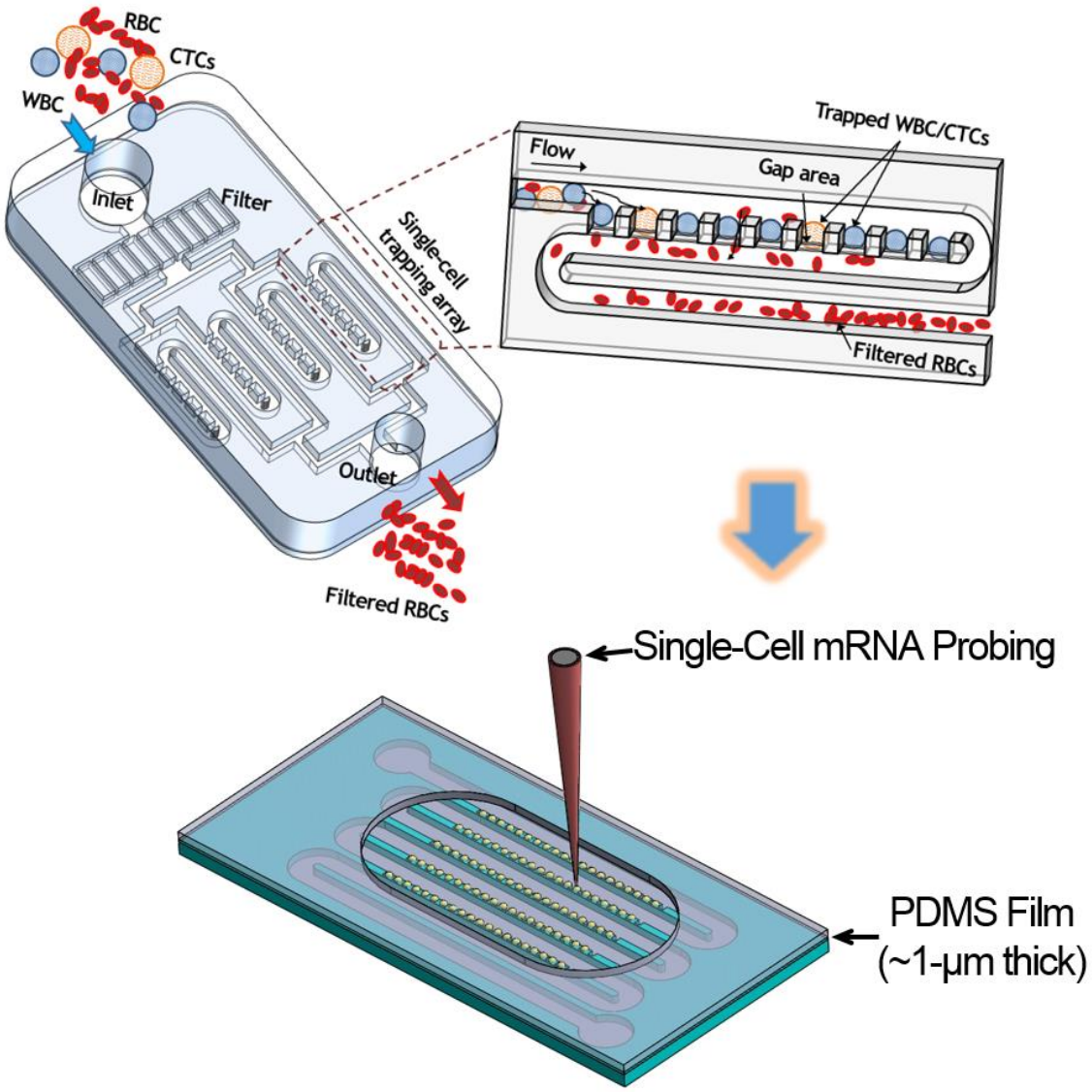

Figure 4.1 Schematic diagram of the integrated microfluidic mRNA probing platform.

To demonstrate the platform, 100 live human carcinoma (HeLa) cells were trapped in the single-cell array, and the single-cellular expression levels of 3 housekeeping genes, ACTB (beta-actin), GAPDH (glyceraldehyde 3-phosphate dehydrogenase), and HPRT (hypoxanthine phosphoribosyltransferase), were analyzed quantitatively based on the RT-

qPCR results of the probed-out mRNAs from the trapped single HeLa cells. Microfluidic trapping and *in situ* single-cell mRNA extraction from a mixture of SK-BR-3 (human breast cancer cell line) and U937 cells (human monocyte cell line) were also demonstrated. SK-BR-3 cell line represents a common type of CTCs found in a patient's peripheral blood, while U937 cell line represents the WBC background of a typical pre-enriched CTC sample. The presented platform facilitates the entrapment of single target cancer cells without complicated microfluidic networks, and is the first to extract mRNAs from single cells of interest *in situ* with minimal impact on cell viability from a closed microfluidic environment.

Materials and Methods

Fabrication of the ultra-thin PDMS membrane-sealed single-cell array

The device assembly procedure is illustrated in Fig. 4.2A. Bond-detach lithography[63] was used to seal the PDMS microfluidic device with an ultra-thin PDMS membrane. The ultra-thin PDMS membrane was fabricated by spin coating and heat curing of PDMS pre-polymer mixture's hexane diluent on a Teflon (Teflon® diluted in Fluorinert™ FC-40 at a 1:5 ratio) coated silicon wafer. Teflon coating efficiently reduced the adhesion of PDMS to silicon wafer to facilitate an easy peeling off of the sealed device; while diluting PDMS pre-polymer mixture in hexane reduced its viscosity, so that a much thinner membrane could be produced at similar spin coating parameters.[64] Fig. 4.2B summarizes the resulting membrane thickness according to the ratio of hexane to PDMS pre-polymer at the spin coating condition of 5000 rpm for 5 min. The final thickness of the PDMS membrane used in the platform was chosen to be 1 μm (measured by Dektak 3 Profilometer), which was fabricated by spin

coating PDMS and hexane mixture at a mass ratio of 1 to 2. Optical image of the ultra-thin PDMS membrane and a finished device are shown in Fig. 4.2C and D. The spin-coated PDMS membrane was left in a 120 °C oven for 45 minutes to evaporate the hexane and in a 65 °C oven for 1 day to ensure curing. The microfluidic trapping array was fabricated in PDMS by soft lithography, and it was irreversibly sealed with the ultra-thin PDMS membrane after exposure to oxygen plasma for 60 s.

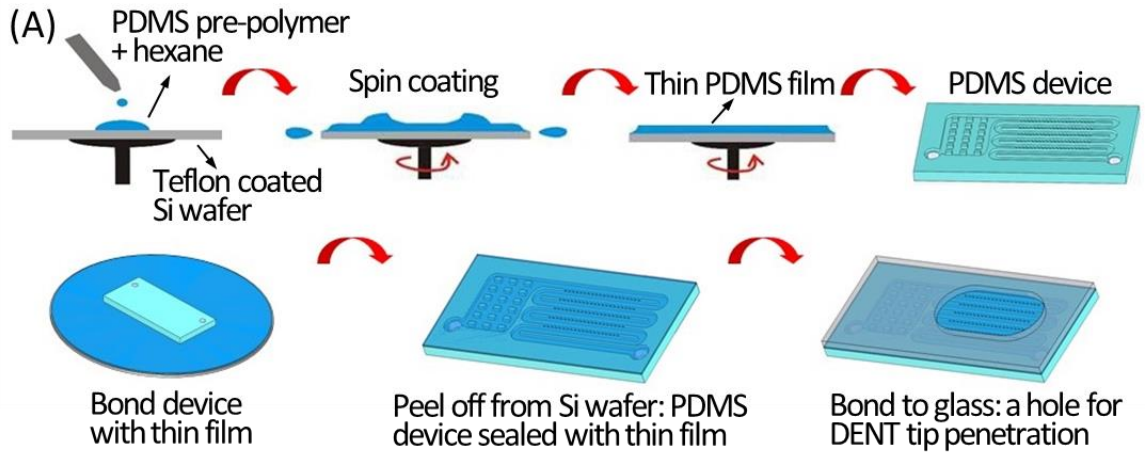

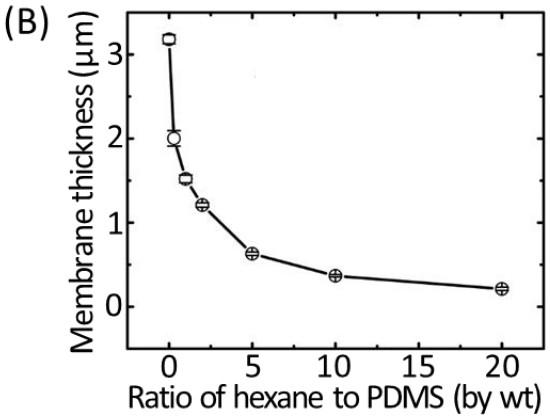

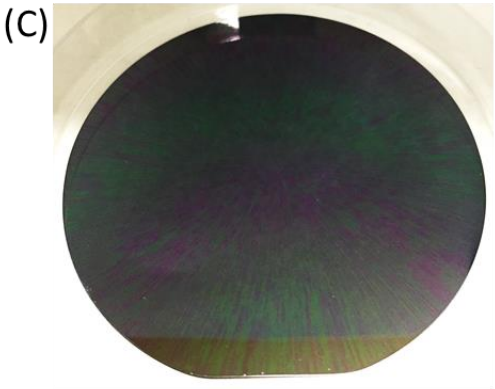

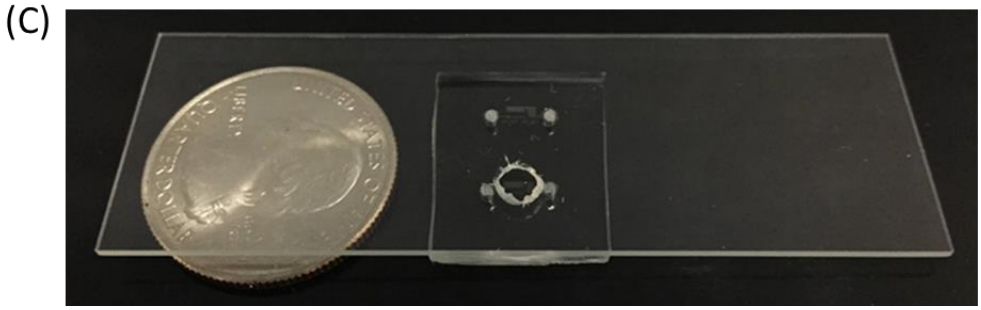

Figure 4.2 Fabrication of the ultra-thin PDMS membrane-sealed single-cell array.
(A) Fabrication procedure of the ultra-thin PDMS membrane-sealed single-cell trapping array. (B) The thickness of the PDMS membrane according to different hexane-to-PDMS ratios at the spin coating condition of 5000 rpm for 5 min. (C) Optical image of an ultra-thin PDMS membrane spin-coated on a silicon wafer. (D) A finished device with a through-hole on the glass substrate.

Fabrication of the modified AFM probe

A DENT probe was built using a commercially available (ATEC-NC, Nanosensors), highly doped (resistivity 4–6 Ω cm) silicon AFM probe (k ~ 45 N/m). The fabrication process started by growing a 40-nm-thick SiO_2 layer on the AFM probe in a conventional dry oxidation furnace. The SiO_2 layer served to electrically insulate the entire silicon probe including the AFM cantilever. Then a 10-nm-thick chromium adhesion layer followed by a 20-nm-thick gold layer were deposited on top of the SiO_2 layer by ion-beam sputtering to serve as the outer electrode. In the final step, we cut the end of the Au-coated tip using Focused Ion Beam (FIB) to expose the inner silicon core with a width of 300 nm. Alternatively, considering the low throughput and high cost of FIB cutting, we developed a mechanical cutting process by hitting just the tip-end with the sharp edge of a Si_3N_4 wafer during AFM scanning, with details described in Appendix B.

Details of the apparatus

The as-fabricated DENT probe was mounted on a probe-holder with electrical connection for mRNA extraction (Fig. S3A). The inner Si core was connected to the silver paint at the bottom of the holder, and the outer Au layer was connected to a thin piece of copper electrode on top of the holder via a spring contact. This copper electrode was connected with the AC power supply, and it helped to fasten the DENT probe. The detailed setup of the integrated microfluidic-nanoprobing platform is shown in Appendix B. The apparatus was

built upon an inverted microscope (Olympus IX71) with a CCD camera (Photometrics), equipped with an add-on upright imaging system consisted of a 40x lens tube with motorized zoom/focus function and a USB camera (Thorlabs). A 3D-printed microfluidic chip holder was attached to the motorized x-y translation stage (Thorlabs) with a calculated moving resolution of 200 nm in the x-y plane. The probe-holder was controlled by a stepper motor (Thorlabs) with a calculated moving resolution of 50 nm in the z direction for penetration. A LabVIEW controlled graphic user interface was developed to facilitate operation.

Viability assay

To validate the viability of the mRNA-extracted cells after probing, a live assay was performed by flowing 2 μM Calcein AM (Sigma-Aldrich) through the microfluidic trapping array for 15 min after 12 hr on-chip culturing of the probed cells, and measuring the green fluorescence intensity.

Primer design

The mRNA sequences of ACTB, GAPDH, HPRT, CD45, EpCAM, and HER2 were checked in GenBank, and their primers were designed using the online PrimerQuest® Tool (Integrated DNA Technologies). All the primers were designed to be intron-spanning to preclude the amplification of genomic DNA. The sequences of the above primers were as follows:

ACTB,

5’-TCATCACCATTGGCAATGAG-3’ (forward) and 5’-ACTCCATGCCCAGGAAGGA-3’ (reverse);

GAPDH,

5’-TCCACTGGCGTCTTCACC-3’ (forward) and 5’-GGCAGAGATGATGACCCTTTT-3’ (reverse); HPRT,

5’-TGACCTTGATTTATTTTGCATACC-3’ (forward) and 5’-CGAGCAAGACGTTCAGTCCT-3’ (reverse); CD45,

5’-CGGCTGACTTCCAGATATGAC-3’ (forward) and 5’-GCTTTGCCCTGTCACAAATAC-3’ (reverse); EpCAM,

5’-CGCAGCTCAGGAAGAATGTG-3’ (forward) and 5’-TGAAGTACACTGGCATTGACG-3’ (reverse); and HER2,

5’-AAAGGCCCAAGACTCTCTCC-3’ (forward) and 5’-CAAGTACTCGGGGTTCTCCA-3’ (reverse). All the primers were purchased from Integrated DNA Technologies. DNA oligomers (Integrated DNA Technologies) with the same sequences as the target genes’ amplicons were used to construct standard curves for the calibration of molecule numbers from RT-qPCR results.

Results

Design and operating principle of the platform

Fig. 4.1 shows the schematic of the platform, which is a membrane-sealed microfluidic chip for single-cell trapping, integrated with a modified AFM probing system (DENT) for the extraction of mRNA molecules from a specific living cell.

After cells are trapped in the microwell array, the microfluidic device is placed onto the upright microscope. As illustrated in Fig. 4.3A, the DENT tip is accurately aligned with the target cell and penetrates through the ultra-thin PDMS membrane to extract mRNA

molecules from cytoplasm upon the application of AC electric field. Applying AC field between the inner Si core and outer metal layer creates a large gradient of the electric field square (∇E^2) at the probe-end, resulting in a dielectrophoretic attractive force ($F_{DEP} = [(V\alpha)/2]\nabla E^2$; V, particle volume; α, polarizability) strong enough to attract mRNA molecules toward the probe-end.[62] The probe is then retracted from the device, and mRNA molecules are released from the tip to perform RT-qPCR for quantitative gene expression analysis.

Characterization of the modified AFM probe

The as-fabricated DENT probes were examined by scanning electron microscopy (SEM) to ensure sufficient sharpness before each cell probing experiment (Fig. 4.3B). The original silicon probe was in a pyramid shape with a length of 15 μm. It served as the inner electrode with a resistivity of 4 ~ 6 Ω cm, and a force constant of ~ 45 N/m. The SiO_2 layer, grown on the probe surface by conventional dry oxidation furnace with a thickness of 40 nm, served to electrically insulate the entire silicon probe including the AFM cantilever and handling chip. A 10-nm-thick Cr adhesion layer followed by a 20-nm-thick Au layer were deposited on top of the SiO_2 layer, which served as the outer electrode. The pinpoint of the modified AFM probe was cut with FIB to expose the high-dope silicon core, resulting in an equilateral triangular probe-end surface with a side length of around 300 nm (Fig. 4.3B bottom). The 3D distribution of the gradient of the electric field square (∇E^2) at the probe-end was calculated by the finite element method (FEM) solver (COMSOL Multiphysics), and when a 1.5 Vpp, 10 MHz AC field was applied between the Si core and Cr/Au outer electrode, the calculated ∇E^2 at the probe-end was plotted in Fig. 4.3C in logarithmic scale. The largest ∇E^2, ~ 1024 V^2/m^3, was distributed in the oxide part in between the inner core and the outer electrode. As the

DEP force is given by $F_{DEP} = [(V\alpha)/2]\nabla E^2$, where V is the volume of particle and α is the polarizability, the edge of the probe-end would have more extracted mRNA molecules compared to the center of the probe-end surface. This calculated ∇E^2 of our experimental setup was larger than published values for RNA manipulation in suspension,[65] probably because the complex composition of cytoplasm affected the polarizability of mRNA molecules inside the cell. The strength of the DEP force damped from the probe-end, therefore mRNAs would move from cytosol to the probe-end due to the positive DEP effect. Theoretically, if the applied AC voltage was high enough, the entire cytosol volume would be subjected a DEP force strong enough to drive mRNA movement, so all mRNA molecules in the cytosol could be concentrated at the probe-end. The applied frequency, i.e., 10MHz, was selected according to previous publications[62, 66] with experimental modifications as the mRNA sensitive frequency. This high frequency also reduced the potential electrolysis damage.

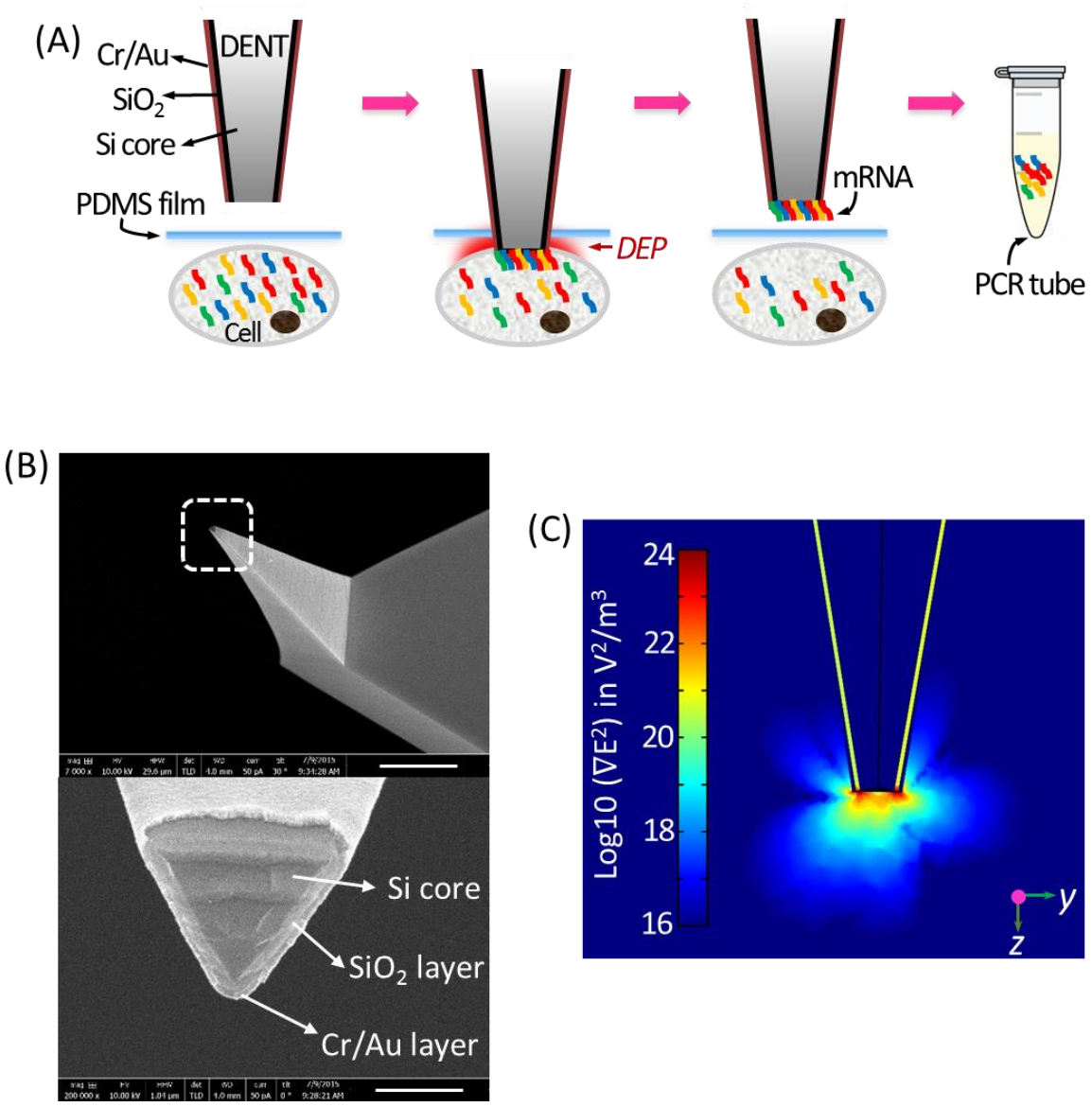

Figure 4.3 Mechanism of mRNA extraction by DENT.
(A) The process of single-cell mRNA extraction using DENT. Application of AC field between the inner Si core and the outer metal layer creates a large electric field gradient at the probe-end, generating a dielectrophoretic attractive force to attract mRNA molecules towards the probe-end. The probe is then retracted from the device, and mRNA molecules are released from the tip to perform RT-qPCR for quantitative gene expression analysis. (B) Left: SEM image of the modified AFM probe (scale bar: 5 μm); Right: zoom-in image of the probe-end (scale bar: 200 nm). (C) Logarithmic scale color plot showing the simulation result (COMSOL Multiphysics) of the gradient of the electric field square (∇E^2), once the probe is inserted into the cell with an applied AC field of 1.5 Vpp in amplitude and 10 MHz in frequency.

On-chip trapping of HeLa cells and single-cell mRNA probing

For initial proof of concept, we started with probing single HeLa cells in the ultra-thin membrane-sealed single-cell array. The bright-field microscopic images recording the procedure of single-cell mRNA extraction using the DENT probe are shown in Fig. 4.4A. The cell-trapping array was mounted on the motorized translation stage, and was moved in the x-y plane to align the target cell with the tip-end of the DENT probe. The probe was controlled to move down along z direction until the contact between the tip-end and the PDMS film led to localized membrane deformation, with wrinkles near the tip-end observed under the microscope. Short AC pulses were then applied to the stepper motor to move the probe further down (along the z direction) in 500-nm pulse-steps for penetration (Movie. 4.1). As the target cell was in close contact with the PDMS film, and the cell membrane thickness was less than 10 nm, once punching through the PDMS film, the DENT probe would penetrate through the cell membrane and insert into the cytoplasm. The penetration was stopped when the probe punched through both the PDMS sealing film and the cell membrane, which could be indicated by a clear relaxation of the cantilever bending. Once the probe inserted into the cell, the AC field between inner and outer electrodes was turned on, and mRNAs were attracted toward the tip-end by DEP force. After 75 s,[62, 66] the probe was retracted from the cell, the AC field was turned off, and the extracted mRNA molecules were released for RT-qPCR to obtain the cell's gene expression fingerprint. The self-sealing capability of the ultra-thin PDMS film was such that no punctured hole or leakage was observed under the microscope after retracting the probe from the cell-trapping array (Fig. 4.4A and Movie 4.1). Also, there was no leakage when cell staining solution or PBS buffer was pumped into the single-cell array after probing, at the flow rate of 2 μL/min for several hours.

To verify that the tip was inserted into the cytoplasm, it was penetrated into a Calcein AM-stained HeLa cell, and fluorescence molecules of Calcein AM were successfully detected at the tip-end under an upright fluorescence microscope (Fig. 4.4B).

Fig. 4.4C shows the fingerprint of the expression levels of three housekeeping genes in a single HeLa cell under the applied AC field of 1.5 Vpp, 10 MHz: ACTB, a high-abundant gene; GAPDH, a medium-abundant gene; and HPRT, a low-expression gene ($<10^2$ copies per cell). For each target gene, 10% of the total cDNA product was transferred into the qPCR reaction volume, and SYBR-Green was used as the detection dye. With this current RT-qPCR setup, the expression levels of 10 different genes can be analyzed for each single cell. However, more genes can be analyzed by increasing the efficiency of the qPCR assay, so that less amount of cDNA product is used for each gene. Also, sequence-specific fluorescent probes can replace SYBR-Green as the reporting dye, therefore different genes can be quantified at the same time.

As the applied voltage increased, the extracted number of mRNAs dramatically increased because of the stronger DEP force and higher mRNA extraction efficiency associated with the increased voltage (Fig. 4.4D). Using qPCR, the cycle threshold (Ct) presents a relative measurement of the amount of a target gene: a lower Ct indicates a greater amount of the target gene. Under the AC field of 1.1 Vpp, 10 MHz, small numbers of ACTB (mean Ct = 31.4, SD = 1.1) and GAPDH (mean Ct = 32.3, SD = 0.7) mRNAs were successfully extracted without HPRT reading. At the applied voltage of 1.5 and 1.9 Vpp, all three types of mRNAs were successfully extracted, but more ACTB and GAPDH were extracted than HPRT because of their intrinsic difference in expression levels. The control group, probing the empty trap inside the microfluidic channel, showed a negative reading

with no amplification. The Ct value was higher compared to that of probing single cells in the media cultured in the petri dish reported in Nawarathna et at.,[62] where detached cells and debris from surrounding cells could stick on the tip when it dipped into the media. As the trapped cells were in close contact with the sealing film and were isolated by the physical traps, probing single cells in the microfluidic trapping array avoided the false-positive readings and cross-contamination. The absolute numbers of extracted mRNAs under an applied voltage from 1.1 to 1.9 Vpp (Fig. 4.4E) were calculated based on the Ct values of the RT-qPCR experiments and the standard curves generated using the synthetic oligomers of known concentrations, and the mRNA capturing efficiency at different probing voltages was compared with the standard cell-lysing mRNA extraction method (Appendix B). The average extracted copy number of ACTB from a single HeLa cell was 220 ± 100 at 1.1 Vpp, 2580 ± 690 at 1.5 Vpp, and 5440 ± 940 at 1.9 Vpp, respectively. The average extracted copy number of GAPDH was 100 ± 30 at 1.1 Vpp, 740 ± 380 at 1.5 Vpp, and 2940 ± 870 at 1.9 Vpp, respectively. As for the HPRT, although there was no reading at 1.1 Vpp, 40 ± 10 molecules were captured at 1.5 Vpp, and 90 ± 40 molecules were extracted out at 1.9 Vpp. These results show that the presented approach has tunable target signal intensity according to the applied voltage, and the numbers of extracted mRNAs correlates with the genes' expression levels. The ability to probe and detect the low-copy-number gene HPRT's mRNA molecules is critical as it benefits the analysis of target genes with low expression levels.

A cell viability assay was performed to see if the mRNA-extracted cell was still alive in the microfluidic channel. Fig. 4.4F shows the bright-field and fluorescent images of mRNA-extracted cells by DENT stained with Calcein AM. We stained the mRNA-extracted cells with Calcein AM after 12 hr on-chip culture. Bright-field and fluorescent images of single cells

showed that live cells were distinguishable clearly by their intact morphology and bright green fluorescence. The viability of mRNA-extracted cells probed under the application of lower voltages such as 1.1 and 1.5 Vpp was ~ 70%, which was similar to the viability of non-probed cells. However, the mRNA-extracted cells probed under the application of higher voltages like 1.9 Vpp had much weaker green fluorescence signal, which was because a large number of mRNA molecules were extracted by the DENT tip, affecting the cell metabolism. No cell adhesion or proliferation was observed during the culturing of mRNA-extracted cells, and most of the non-probed cells did not adhere to the microchannel bottom or proliferate, either. One possible explanation was that the channel height was only ~18 μm, too small to supply enough nutrition and space for growing cells. In fact, most microfluidic devices which allow on-chip cell culture have a channel height over 100 μm.[67, 68] Although DENT caused a physical disturbance to the cell membrane, at the applied voltage of ~ 1.5 Vpp, cells maintained intact morphology and viability after probing, with substantial mRNA extraction efficiency achieved. Therefore, we chose this field strength for further marker-gene expression analysis.

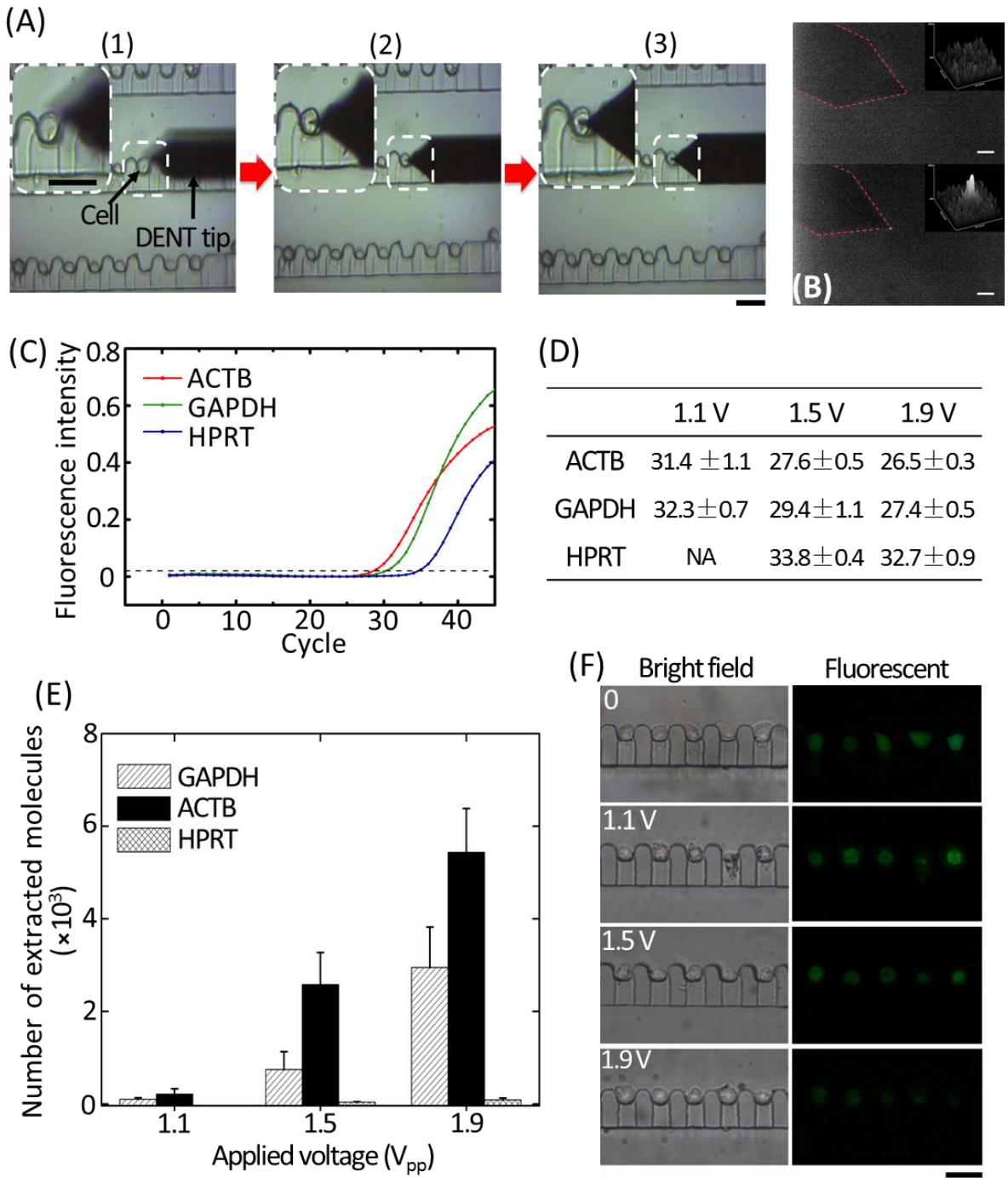

	1.1 V	1.5 V	1.9 V
ACTB	31.4 ±1.1	27.6±0.5	26.5±0.3
GAPDH	32.3±0.7	29.4±1.1	27.4±0.5
HPRT	NA	33.8±0.4	32.7±0.9

Figure 4.4 *In situ* mRNA extraction by DENT.
(A) Bright-field images capturing the single-cell mRNA probing process. White dashed box indicates the cell of interest. The probe was moved downward toward a target cell, penetrated through the PDMS membrane and inserted into the target cell to extract mRNAs by DEP force. Scale bar: 30 μm. (B) Fluorescent images of the DENT probe before (up) and after (down) penetration into a Calcein AM-stained HeLa cell, with a 5 μm × 5 μm fluorescence intensity plot of the probe-end on the top-right corner. Scale bar: 10 μm. (C) RT-qPCR results of three housekeeping genes' mRNAs extracted from the target single HeLa cell at the applied AC field of 1.5 Vpp, 10 MHz. The threshold intensity

was 0.02 indicated by the dashed line. (D) The quantified Ct values of extracted mRNA molecules of 3 the target genes (ACTB, GAPDH, and HPRT) from single HeLa cells by single-cell probing at three different applied AC voltages (1.1, 1.5 and 1.9 Vpp), with a constant frequency of 10 MHz. 10% of the cDNA product was used for the quantification of each gene. (E) The calculated absolute numbers of extracted mRNAs under an applied voltage from 1.1 to 1.9 Vpp based on the above Ct values of the RT-qPCR experiments and standard curves. (F) Bright-field and fluorescent images of mRNA-extracted cells stained with Calcein AM after on-chip culturing for 12 hr, respectively.

On-chip trapping of CTC/WBC mixtures and cell type identification

In order to develop a microfluidic CTC screening/analysis platform, we tested the feasibility of identifying single cancer cells from the normal blood cell population by selective mRNA extraction using DENT. A mixture of SK-BR-3 and U937 cells with a concentration of 1×10^6 cells per mL was introduced into the trapping array, mimicking a blood sample that underwent primary CTC enrichment (Fig. 4.5A). After SK-BR-3 and U937 cells were trapped in the microwell array, we performed *in situ* mRNA probing from these two different types of single cells (Fig. 4.5B and C). SK-BR-3, a human breast cancer cell line, expresses EpCAM (epithelial cellular adhesion molecule) as a CTC marker,[69] and over-expresses HER2 (human epidermal growth factor receptor 2) as a breast cancer cell marker.[70] Whereas U937 is a human monocyte cell line, representing the dominant type of WBCs in human blood. It expresses CD45 as a leucocyte marker,[71] does not express EpCAM,[72] and should have a much lower HER2 expression level compared to breast cancer cells.[73] The averaged single-cell mRNA probing results matched with the above marker-gene expression status reported in the literature. With the applied AC field of 1.5 Vpp, 10 MHz, mRNAs of EpCAM (Ct = 33.0, SD = 1.5) and HER2 (Ct = 27.1, SD = 1.0) were successfully extracted from SK-BR-3 cells by the DENT tip without CD45 reading. Whereas for U937 cells, CD45 (Ct = 32.6, SD = 1.0) was extracted, but there was no EpCAM reading and a much lower HER2 reading (Ct = 36.1, SD = 1.3). ACTB from both of the two types of cells was quantified by RT-qPCR as the

positive control. Based on the mRNA expression results plotted in Fig. 4.5B and C, although the two types of cells were in a similar size range and could not be differentiated easily from the optical images, the RT-qPCR fingerprint of a specific single cell's mRNAs extracted by DENT revealed its specific gene expression levels and cell identity. Fig. 4.5D shows the gene-expression heatmap[74] representation of 12 single cells probed at the SK-BR-3/U937 cell mixture single-cell array. There still existed obvious differences in gene expression between SK-BR-3 and U937 cells, and also cellular heterogeneity within the same population. With the ability to plot gene expression profiles of target cancer cells, it might be possible to identify the tissue origin of CTCs by the detection of organ-specific metastatic signatures from the cells, which is helpful to localize small, occult metastatic lesions and to guide further diagnostic and therapeutic strategies.

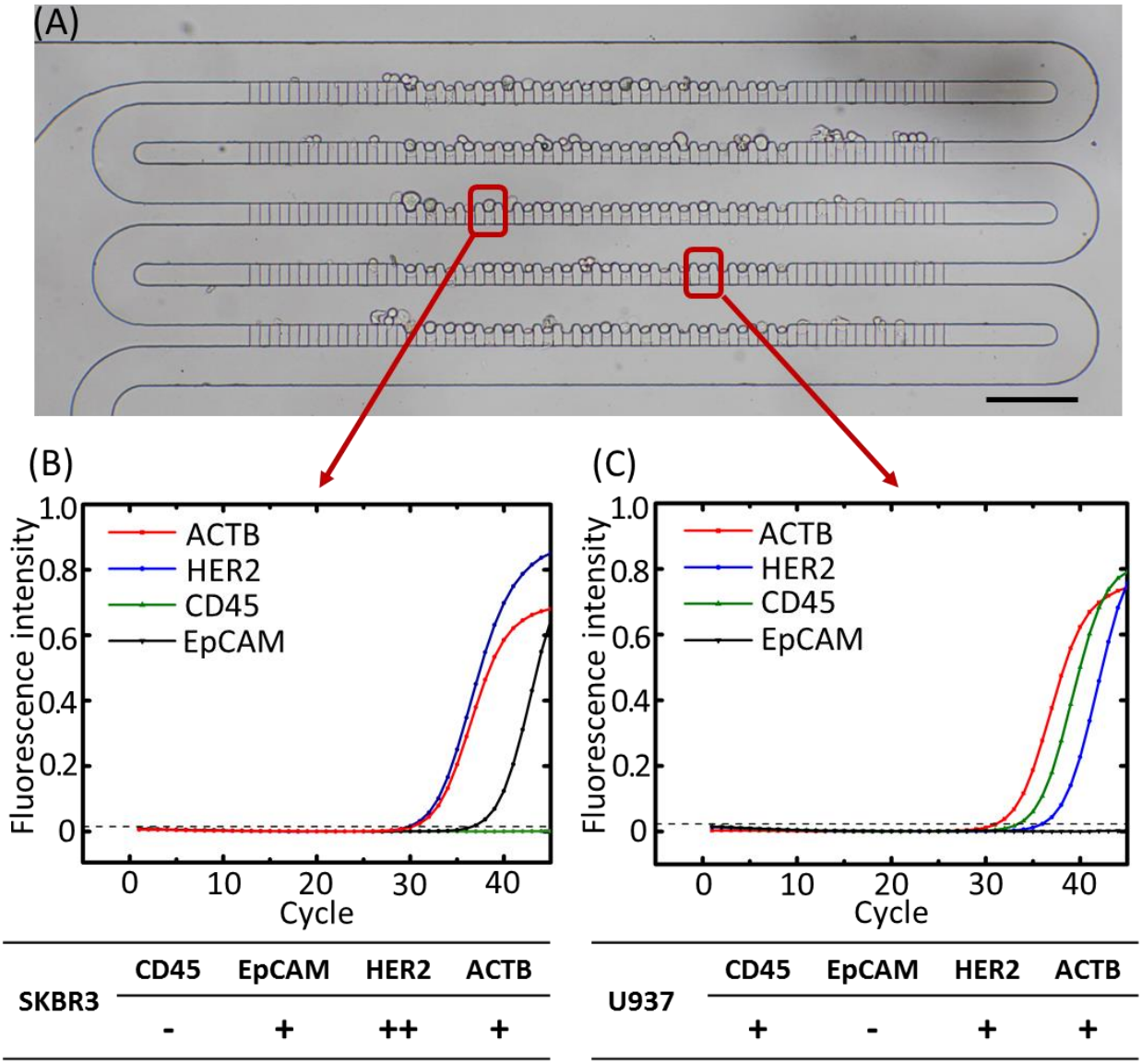

SKBR3	CD45	EpCAM	HER2	ACTB
	-	+	++	+

U937	CD45	EpCAM	HER2	ACTB
	+	-	+	+

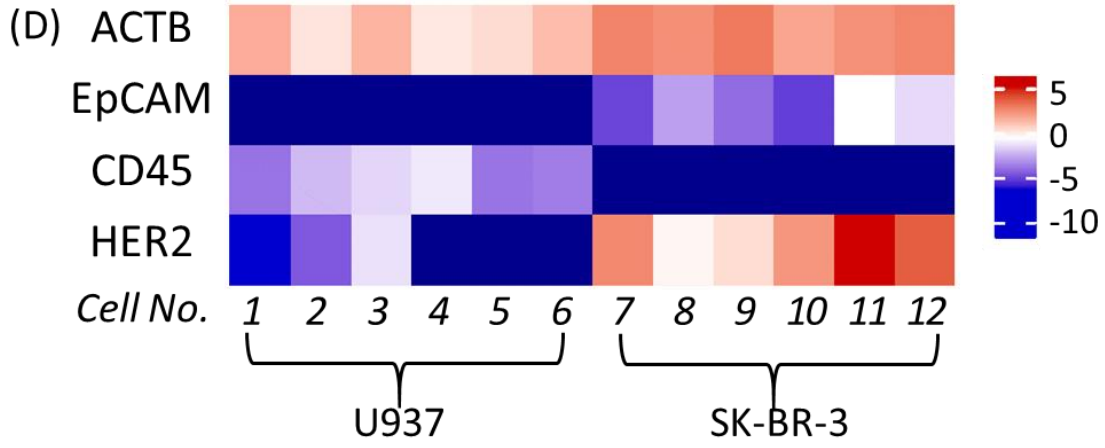

Figure 4.5 Identifying SK-BR-3 cancer cells from U937 monocytes in the single-cell array by their marker-genes' expression via *in situ* mRNA probing.
(A) A mixture of SK-BR-3 and U937 cells are trapped in the single-cell array. The RT-qPCR fingerprints of the 4 target mRNAs (CD45, EpCAM, HER2 and ACTB) extracted by DENT from a trapped SK-BR-3 cell and a trapped U937 cell are shown in (B) and (C), respectively. (D) Gene-expression heatmap of trapped single SK-BR-3/U937 cells based on the RT-qPCR results of extracted mRNAs. All single-cell Ct values were normalized with the average gene-expression values as described in Thomsen et al.[74]

Discussion

To summarize, we utilized DENT to extract mRNAs and quantified various marker-genes' expressions of target single cells within the microfluidic trapping arrays. As the microfluidic device was sealed by an ultra-thin PDMS membrane (≤ 1-μm-thick), external equipment such as an AFM nanoprobe, was able to penetrate into the microfluidic trapping array and access a specific cell without cross-cell contamination and media evaporation. This technique opens up new opportunities in the integration of microfluidic systems with various external elaborate instruments such as micro-pipettes and micro-injectors, so that more complicated manipulations and analyses of single cells could be performed inside a closed microfluidic environment. Samples can be processed – filtered, sorted, and enriched – before entering the 'single-cell analysis' region on the chip. After analyzing, as the cells can retain viability, they can be released for further analysis and culturing by reversing the flow, making it possible to move beyond static snapshots of gene-expression profiles to understand how profiles change over time, e.g., real-time tracking of cell response to drug treatment. Specifically, DEP-based mRNA extraction using DENT is a non-destructive method that does not require cell lysing or mRNA purification, and is sensitive enough to detect the expression level of low-copy-number genes (e.g., HPRT) within a single living cell. In addition, as it works at the

frequency specific for mRNAs and avoids the removal of cytosol, cells are protected from losing essential molecules.

Benefited from the multi-step-integration feature of lab-on-a-chip systems, different sample-processing units can be integrated with this ultra-thin PDMS membrane-sealed single-cell array. For example, the presented microfluidic design can be easily combined with a variety of microfluidic modules for erythrocytes removal with high enrichment of CTCs, like blood filtration by inertial microfluidics,[16] dielectrophoretic cell sorting,[34] CTC capturing by antibody labeling,[14] or immunomagnetic cell separators.[15] This capability is notably important when genetic profiling of the patient-derived CTCs from whole blood is required.

Continuous monitoring of the cells' response to stimuli (e.g., drug screening) at the single-cell level by long-term on-chip culturing and repeated mRNA probing would be of significant interest. The current array configuration is not suitable for long-term culturing, and a next step would be modifying the trapping array with a higher channel height to provide sufficient space and nutrition supply for long-term on-chip culturing of the probed cells.

A limitation of this approach is that only one probe penetrates into one cell each time, which limits the throughput of single-cell mRNA extraction. However, a high-density array of DENTs could be fabricated by adapting the microneedle array[75] fabrication techniques, e.g., DUV (deep ultraviolet) photolithography, DRIE (deep reactive ion etching) and crystalline wet etching. In this way, hundreds of DENT probes can penetrate into hundreds of single cells each time with the combination of an automated micromanipulator, which allows for high-throughput single-cell transcriptomic analysis.

CHAPTER 5: SINGLE-CELL GENE TRANSFECTION VIA DROPLET MICROFLUIDICS

Upon accomplishing the phenotypic and genotypic characterization of CTCs at the single-cell level, the next step comes to genetically modify the cancer cells to correct aberrant genes. In this chapter, we report a novel droplet-based microfluidic platform that enables efficient single-cell transfection.

Background

Gene therapy, the delivery of nucleic acids into patient cells to correct aberrant genes, has been rapidly gaining momentum as a revolutionizing modality for the treatment of cancer, infectious diseases, and hereditary disorders. In 2017, the U.S. Food and Drug Administration (FDA) approved the first ever gene therapies, Kymriah and Yescarta, for the treatment of children's advanced leukemia and adult lymphoma, indicating that gene therapy has evolved from a promising vision to a practical solution to cancer.[76] Both of the two therapies genetically edit the T cells extracted from a patient to express chimeric antigen receptors (CARs), and infuse them back to the patient to kill cancer cells.

A key limitation in gene therapy development remains the lack of an efficient, safe, and controllable method for intracellular delivery of exogenous materials. Viral vectors infect the host cell and integrate their carried genetic materials into the cell's genome, which attains high transfection efficiency, but leads to side effects due to immunogenicity and the risk of disrupting the vital parts of the host cell genome.[77] Electroporation creates transient pores on cell membrane by high-voltage pulses to deliver DNA into cells, which is the most

efficient physical transfection method, but the high-voltage electrical pulses generally result in a high cell death rate.[78] Non-viral vectors such as cationic lipids, self-assemble with negatively charged nucleic acids into nanoparticles called lipoplexes (cationic lipid-nucleic acid complexes) by electrostatic interaction, and mediate gene transfection via endocytosis.[79] Cationic lipids avoid immunogenicity, mutagenesis, and cell-damage compared to viral vectors or electroporation, their transfection efficiency, however, is generally not as high. In particular, the lipoplex-mediated transfection (lipofection) efficiency is extremely low for suspension cells such as lymphatic and hematopoietic cells used in immunotherapy.[20, 21] The reported transfection efficiency for suspension cells was typically less than 5% in the literature when following the standard lipofection protocol.[22-26] It has been suggested that after binding to the cell membrane, the lipoplexes are subsequently taken into the cells by endocytosis, and for cells in the suspension state, this is a very inefficient process.[24, 80] The lipoplex internalization is also inhibited by the sulphated proteoglycans on the cell membrane of hematopoietic cells.[81-83]

Apart from target cells' endocytic capability, another major determinant of lipofection efficiency is the size of the lipoplexes.[84-86] Although formed using the same cationic lipid and DNA concentration and composition, the lipoplex size varies, as the spontaneous electrostatic assembly is affected by various factors: the charge ratio of cationic lipid to DNA, the order in which components are mixed, the mixing rate and time, the media composition, etc.[87-89] Conventional bulk lipoplex preparation processes by hand shaking or vortexing yield a large size distribution of lipoplexes due to lack of control of the many variables, which adversely affects the lipofection efficiency and consistency, since a significant fraction of the lipoplexes are either too large or too small for intracellular

delivery.[89, 90] What is more, as lipoplex is typically used at low concentrations (e.g., 1 μg per 100 μL) to minimize cytotoxicity, the diffusion limitation in the bulk volume hinders lipoplex-cell interaction, which also limits the transfection efficiency.

On contrary to the bulk process, droplet microfluidics[91] isolates reagents in monodisperse picoliter liquid capsules and manipulates them at a throughput of thousands of droplets per second. Upon co-confinement in picoliter micro-reactors, the high surface-area-to-volume ratio and shorter diffusion distance at the microscale facilitate high reaction efficiency.[92] In addition, the rapid mixing of droplet contents by chaotic advection in winding channels enables reagents to have a higher chance of collision and allows complete mixing on sub-millisecond timescales,[93] which is suitable for monodisperse nanoparticle synthesis.[94, 95] Droplet microfluidics has also emerged as an effective tool for single-cell analysis, as it provides an isolated compartment for the single cell and its surrounding environment, enables quantitative control of the reagents because of monodispersity, and allows for efficient and high-throughput processing of tens of thousands of single cells.[27]

Here, we present a droplet microfluidics-based single-cell transfection platform for lipoplex-mediated efficient and consistent plasmid delivery for suspension cells: single cells were co-encapsulated with cationic lipids and plasmids in monodisperse micro-droplets and subjected to chaotic advection in the winding channel. In this platform, the chaotic mixing generated uniform lipoplexes for effective gene delivery, the co-confinement of a single-cell and lipoplexes in a picoliter-droplet together with chaotic advection resulted in intensive lipoplex-cell collision, and the membrane permeability was increased due to the shear stress exerted on the cell when it passed through the pinch-off at the droplet generation junction. Using our platform, the pcDNA3-EGFP plasmid delivery efficiency improved from ~5% to

~50% for all of the three tested suspension cell lines, i.e., K562 (human chronic myelogenous leukemia cell line), THP-1 (human acute monocytic leukemia cell line), Jurkat (human acute T cell leukemia cell line), with significantly reduced cell-to-cell variation, compared to the bulk approach. Efficient targeted-gene knockout of the TP53BP1 gene for K562 cells via the CRISPR (clustered regularly interspaced short palindromic repeats)-CAS9 (CRISPR-associated nuclease 9) mechanism[96] was also realized through this platform. Lipoplex-mediated single-cell transfection via droplet microfluidics is expected to have broad applications in gene therapy by providing high transfection efficiency and low cell-to-cell variation for hard-to-transfect suspension cells.

Materials and Methods

Chip fabrication and experimental setup

The presented single-cell droplet-lipofection device was fabricated via soft lithography following a similar procedure as explained in Chapter 2. The SU-8 master mold patterned by photolithography had a height of 30 μm. To secure the channel hydrophobicity, the sealed chip was baked at 120 °C overnight. All the reagents were introduced into the microfluidic chip through polymer tubings (Tygon) and syringe pumps (Harvard Apparatus).

Plasmid preparation

The pcDNA3-EGFP vector (Addgene plasmid #13031) encoding EGFP (enhanced green fluorescence protein) was propagated in Escherichia coli (*E.coli*), extracted, and purified using the QIAprep Spin Miniprep Kit (Qiagen). The plasmid was dissolved in EB buffer

(Qiagen) and stored at -20 °C until use. For targeted gene knockout, the 20-bp sgRNA sequence targeting the 2nd exon of the TP53BP1 gene is CAGAATCATCCT-CTAGAACC. The above sgTP53BP1 sequence was cloned into the pLentiCRISPR v2 vector encoding the *S. pyogenes* CAS9 protein, and the re-constructed plasmid was purchased from GenScript. Every time before the transfection experiment, the plasmid concentration was measured by the absorbance at 260 nm using a NanoDrop Spectrophotometer (ND-2000, ThermoFisher).

Lipofection

A day before transfection, cells were re-suspended in 10 mL fresh media at 5×10^5 viable cells/mL in a T-75 flask, to maintain the cells in the logarithmic (Log) growth phase. Before transfection, cells were washed once with Opti-MEM reduced serum medium (ThermoFisher) and re-suspended in Opti-MEM at 10^7 cells/mL. For lipofection via droplet microfluidics, the cell suspension was added with 2 μg per 100 μL of pcDNA3-EGFP plasmid and introduced into the microfluidic chip via one inlet; cationic lipid Lipofectin® (ThermoFisher) was diluted in Opti-MEM at a concentration of 4 μL per 100 μL and introduced through the other inlet. The two co-flowing aqueous phases were sheared by FC-40 (Fluorinert™, Sigma-Aldrich) with 5% 1H, 1H, 2H, 2H-perfluoro-1-octanol (Sigma-Aldrich) into single-cell encapsulating droplets and experienced chaotic mixing in the winding channel. The emulsion was collected and centrifuged at 500 rpm for 30 s to separate the aqueous phase containing cells and lipoplexes from the oil phase. For lipofection via the conventional bulk method, DNA suspension (2 μg DNA per 100 μL Opti-MEM) was added to Lipofectin suspension (4 μL Lipofectin per 100 μL Opti-MEM), gently vortexed and added to the cell suspension.

For both of the lipofection methods, the cells and lipoplexes were incubated at 37 °C, 5% CO_2 for 24 hr, and thereafter, the cells were re-suspended in complete growth media for another 24 hr before transgene expressing investigation.

Flow cytometry

For quantitative analysis of the transfection efficiency and the cell viability, cells were washed and re-suspended in PBS supplemented with 2% FBS at a concentration of 2×10^7 cells/mL 48 hr after initial experiment. 1 μg/mL propidium iodide (Sigma-Aldrich) was added for dead cell staining. The cell suspension was analyzed using the ImageStream Mark II Imaging Flow Cytometer (Amnis Corporation) at 60× magnification under the laser excitation of 488 nm, 150 mW. The data containing the single-cell bright-field and fluorescent images of each individual cell were analyzed using the IDEAS® software package (Amnis Corporation).

Setup of the RT–qPCR

The *S. pyogenes* CAS9 enzyme generates double-strand breaks at the sgRNA targeted locus, which can lead to gene knockout so that the mRNA at this locus will not be transcribed. Here, the TB53BP1 knockout efficiency was analyzed by RT-qPCR using the Cells-to-CT™ 1-Step Power SYBR® Green Kit (ThermoFisher) following the manufacturer's protocol. Firstly, 1,000 transfected K562 cells were lysed in the lysing buffer. Thereafter, for a reaction volume of 20 μL, 2 μL cell lysate, 10 μL qRT-PCR Mix, 0.16 μL RT Mix, 200 nM forward primer, and 200 nM reverse primer were added. A Chromo4 qPCR instrument (Bio-Rad) was used with the following thermal cycling setup: 48 °C for 30 min (reverse transcription), 95 °C for 10

min (polymerase activation), 45 cycles of 94 °C for 15 s and 60 °C for 1 min (amplification). The melting curves were generated by increasing the temperature from 60 °C to 95 °C and holding for 10 s after each 0.5 °C temperature increment. The forward primer sequence was 5'-GGTTCTAGAGGATGATTCTG-3', and the reverse primer sequence was 5'-TTCAGGATTGGACACAAC-3'.

Numerical simulation

Numerical modeling was adopted to analyze the chaotic mixing of droplets passing through the straight/winding channel, and the shear stress at the flow-focusing droplet generation junction. 2D transient modeling of fluid flows for both analyses was performed using COMSOL Multiphysics. Specifically, the level-set multiphase model was employed to accurately track the interface between the aqueous and the oil phases. The density and viscosity of the oil phase were set as 1.855 g/mL and 3.40 mPa·s according to the propriety of FC-40;[97] while the values of 1.007 g/mL and 0.74 mPa·s were chosen for the aqueous phase according to the property of Opti-MEM.[98] The surface tension between the two phases and the contact angle were set at 0.01 N/m and 135°, respectively.[99] Triangular mesh elements were mainly used for meshing the geometries. For studying the chaotic advection in the winding channel, a total of 100,000 triangular elements were used, whereas a total of 20,000 mesh elements were utilized to analyze the shear stress at the flow-focusing droplet generation junction. For both studies, the mesh was refined near the walls of the microchannel for better accuracy.

Results and Discussion

Platform design

The design of the droplet microfluidics-based single-cell lipofection platform is illustrated in Fig. 5.1A, wherein the two co-flowing aqueous phases, one for cell and plasmid suspension and the other for cationic lipid solution, are pinched off at a flow-focusing geometry. At this junction, single cells are co-encapsulated with cationic lipids and plasmids in monodisperse micro-droplets (Figure 5.1B) and experience chaotic mixing in the winding channel. While undergoing chaotic mixing, plasmid and cationic lipid self-assemble into lipoplexes (Figure 5.1C) which enter the co-encapsulated single cell through endocytosis (Figure 5.1D). The concentrations of the suspension cells (10^7 cells/mL), plasmids (2 μg per 100 μL), and cationic lipids (4 μg per 100 μL) were set based on the manufacturer's protocol. 1% (v/v) of Pluronic F-68 was added to the cell suspension to avoid cell aggregation. The composition of the oil phase, FC-40 with 5 % 1H, 1H, 2H, 2H-perfluoro-1-octanol (v/v), was optimized so that the droplets were able to stay apart during the chaotic advection, but were easy (500 rpm, 30 s) to fuse together and separate into two phases for cell and lipoplex collection. It is important to use fluorocarbon oil (i.e., FC-40) as the encapsulation phase instead of hydrocarbon oil (e.g., mineral oil), as explained in Chen et al., fluorocarbon oil has higher gas permeability and much lower solubility of organic molecules, permitting high cell viability and little loss of the transfection reagents into the oil phase.[27] At a flow rate of 1.2 μL/min for the two aqueous phases, and 6.0 μL/min for the oil phase, the resulting single cell-lipoplex co-encapsulating droplets had a diameter of 52 μm (Figure 5.1D and E). See the high-speed videos recording the co-encapsulation and chaotic mixing in the supporting information (Movie 5.1 and Movie 5.2). The droplet production was in the dripping regime

with a production rate of 0.85 kHz, where droplet breakup was shear-dominated and the fluid interface was detached from the channel surface.[27, 100] Due to the limitation imposed by statistics for random cell loading,[100] the single-cell encapsulation efficiency of our platform was ~18%. A higher single-cell loading efficiency could be achieved if our platform is coupled with inertial cell ordering in a curved channel,[101] or inertial cell focusing in a long, high-aspect-ratio microchannel,[102] or one-cell-to-one-droplet releasing by the hydrodynamic micro-vortices at the droplet pinch-off interface.[103]

The cationic lipid we used here is Lipofectin, a widely adopted non-viral vector for mammalian cell transfection, which consists of a mixture of positively charged lipid N-(1-(2,3-dioleyloxy)propyl)-n,n,n-trimethylammonium chloride (DOTMA), and helper lipid dioleoyl-phophotidylethanolamine (DOPE) at a 1:1 (w/w) ratio.[104] Cationic lipids form lipoplexes spontaneously with polyanionic nucleic acids upon electrostatic interaction, and the resulting complexes interact with the cell membrane and are internalized through endocytosis. Upon endosomal maturation, a fraction of DNA escapes and enters the nucleus to elicit gene expression. Alternatively, DNA is degraded within the lysosome.[79, 81] The fusogenic behavior of DOTMA results in functional intracellular delivery of polynucleotide in a manner that bypasses degradative enzymes present in the lysosomal compartment.[36] DOPE facilitates the intracellular release of DNA, as its amine group interacts with DNA phosphate groups, making lipoplex more susceptible to disassembly;[105] besides which, it rapidly fuses with the endosomal lipid bilayer, promoting DNA endosomal escape.[106]

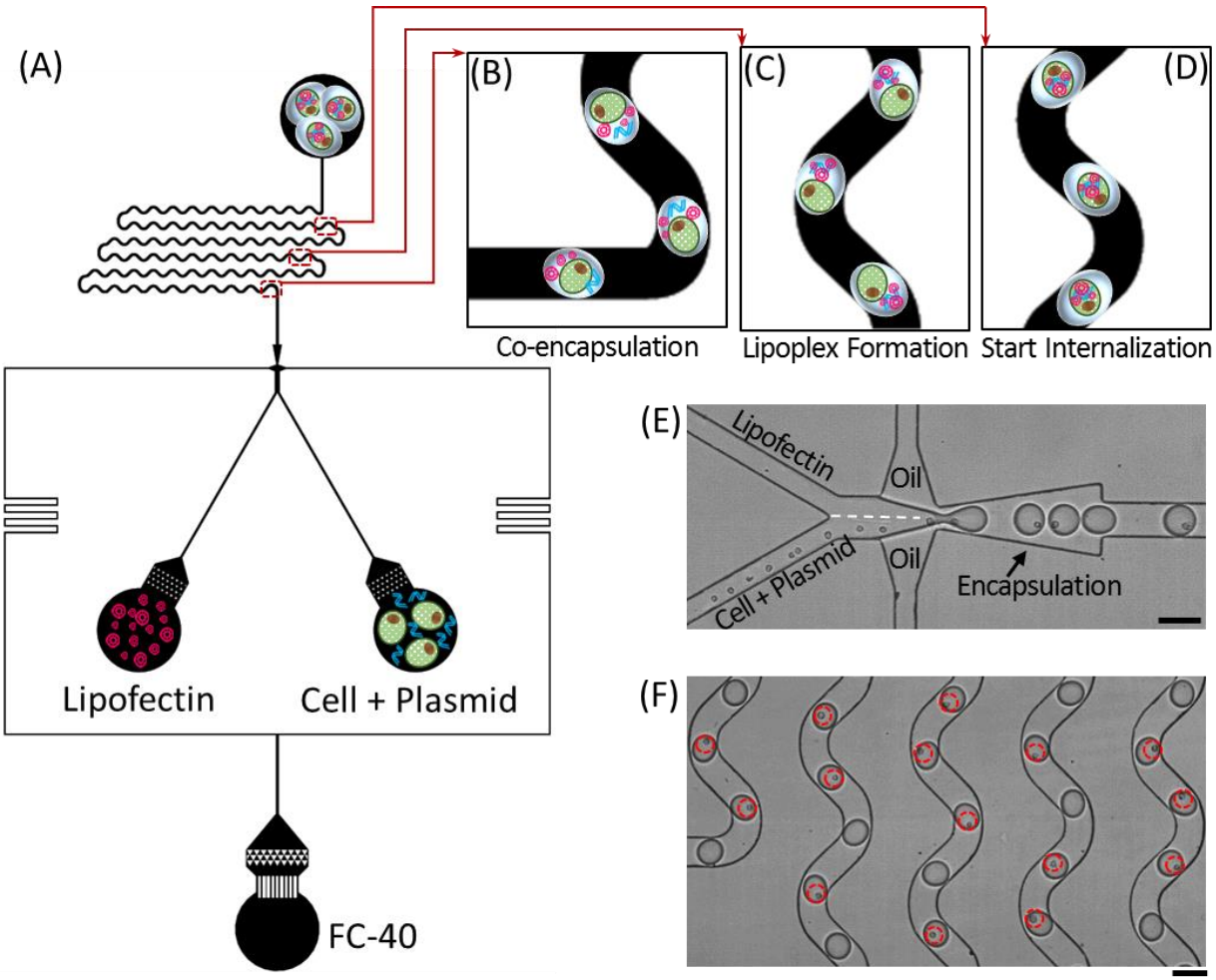

Figure 5.1 Chip design and working mechanism.
(A) Schematic illustration of the droplet microfluidics-based single-cell lipofection platform. The zoom-in views of the circled regions are shown in the upper right corner: a single-cell is co-encapsulated with plasmids and Lipofectin (B), thereafter negatively-charged plasmids and positively-charged Lipofectin self-assemble into lipoplexes during chaotic advection (C), which enter the co-encapsulated single cell by endocytosis (D). (E) Droplet generation and the co-encapsulation of single K562 cells with plasmids and Lipofectin in picoliter-droplets. (F) Bright-field snap-shot of droplets' chaotic advection in the winding channel. The encapsulated single K562 cells are highlighted by red circles. Scale bars: 100 μm.

Chaotic mixing in micro-droplets

Chaotic advection is induced in the unsteady, time-dependent flows inside the droplets that moving through a winding microchannel, which results in rapid mixing on a millisecond timescale.[107-109] The motion of a droplet, co-encapsulating dye and PBS, in the winding

channel of our platform at the same experimental flow rate, was captured by Phantom high-speed camera, and the two-color interface was blurred within 15 ms (Fig. 5.2A). Due to the chaotic mixing inside micro-droplets, the lipoplexes generated from our platform were monodisperse with a mean diameter of 277 nm, which was in the proper size range for internalization by endocytosis.[87, 88] The avoidance of the non-uniformity of lipoplexes prepared via bulk preparing processes (e.g., hand shaking or vortexing) was confirmed by dynamic light scattering (DLS, Fig. 5.2B). As a result, the proportion of lipoplexes that were too large or too small for intracellular delivery was minimized. K562 cells were transfected with pcDNA3-EGFP plasmid using both droplet microfluidics-prepared lipoplexes and vortexing-prepared lipoplexes following the standard lipofection protocol, and analyzed by flow cytometry 48 hr after transfection. As shown in the fluorescence intensity (x-axis) versus cell count (y-axis) histogram of every 1,000 live transfected K562 cells (Fig. 5.2C), cells transfected with droplet microfluidics-prepared lipoplexes (yellow) demonstrated a clear shift towards a higher fluorescence intensity, compared to cells transfected with vortexing-prepared lipoplexes (purple). The EGFP transfection threshold, i.e., the vertical line in the histogram, was defined such that less than 1% of cells in the negative control group (cells transfected with pcDNA3.1 plasmid, a vector without any fluorescence protein-encoding sequences, following the standard lipofection protocol) fell into the effective EGFP transfection region in the histogram (Appendix C), to compensate for auto-fluorescence, surface binding, and endocytosis. Based on 3 repeating experiments transfecting K562 cells following the standard lipofection protocol, the transfection efficiency was 9.0±1.2% when using droplet microfluidics-prepared lipoplexes, which was significantly higher than

4.8±0.9% when using vortexing-prepared lipoplexes (Fig. 5.2D), verifying the importance of the lipoplex monodispersity on transfection efficiency.

When a droplet is moving in a straight channel, due to the equal shearing interaction between the flow and the side walls, two steady and symmetrical vortices are induced within the left and the right (along the flow direction) halves of the droplet (Fig. 5.2E). This results in poor mixing since the streamlines from each half do not cross each other.[107, 108] However, when a droplet is moving in a winding channel, because of the asymmetric shear experienced by the droplet at each turning portion, two asymmetric vortices fold and stretch the fluid inside the droplet, as illustrated by numerical simulation (Figure 5.2F). Thus, chaotic advection and rapid mixing occur inside droplets because crossing of the streamlines becomes possible at each turn. The effectiveness of chaotic advection can be quantified by striation thickness (S_t), the distance over which mixing has to occur by diffusion. For a droplet passing through a winding channel, the striation thickness decreases exponentially according to $s_t(n) = s_t(0) \times 2^{-n}$, as explained in the Baker's Transformation, where n is the number of stretching, folding and reorienting cycles, $s_t(0)$ is the initial striation thickness, and $s_t(n)$ is the striation thickness after n cycles.[93, 107] To compare the lipofection efficiency via droplet chaotic mixing in winding channel versus droplet mixing in straight channel, K562 cells were transfected with pcDNA3-EGFP plasmids using both our droplet-lipofection platform and a modified platform with the winding channel replaced by an equal-length straight channel (Appendix C). As shown in the flow cytometry histogram (Fig. 5.2G), the EGFP positive cells transfected via the platform with a straight mixing channel had a broader fluorescence intensity distribution, which was suggested to be caused by the insufficient droplet mixing. As summarized in Fig. 5.2D, the transfection efficiency using the straight

channel droplet-lipofection platform was 10.3±1.6%, which was higher than bulk lipofection (4.8±0.9%), but was much lower than cells transfected through our platform with a winding channel (51.8±3.3%). The results indicate that chaotic mixing in the winding channel is necessary for achieving the optimum transfection efficiency and consistency. Apart from that, the chance of cell-lipoplex collision was also significantly increased due to the confinement of a single cell with lipoplexes inside picoliter-volume micro-droplets and the intensive chaotic mixing, which overcame the diffusion limitations in the bulk volume.

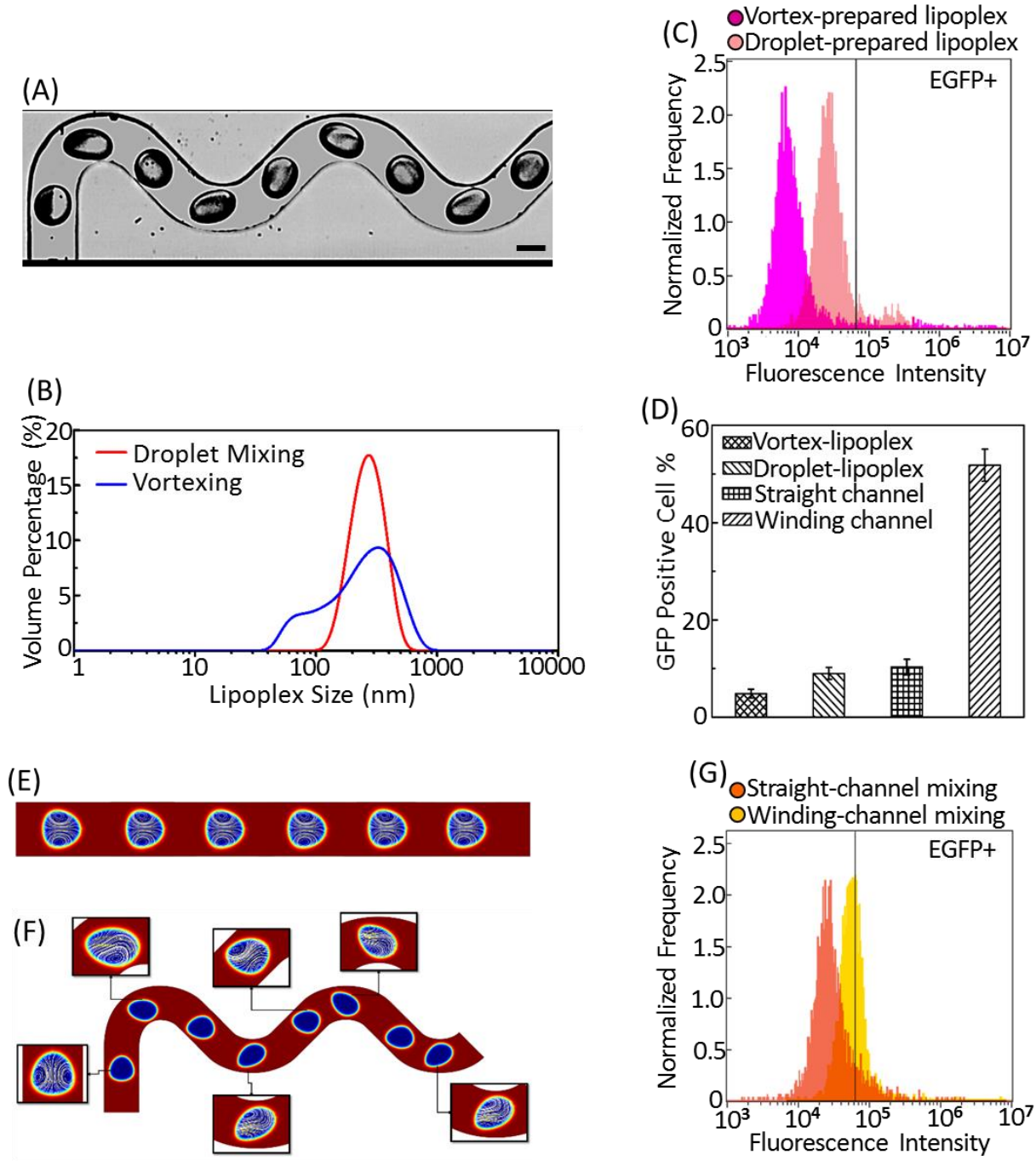

Figure 5.2 Improved lipofection efficiency via droplet chaotic advection in the winding channel.

(A) Chaotic mixing of dye and PBS during droplet advection in the winding channel. (B) DLS size measurement of lipoplexes generated by droplet mixing on our platform compared to the conventional vortexing. (C) Fluorescence intensity histogram of 1000 live single K562 cells analyzed via flow cytometry 48 hr after transfection with pcDNA3-EGFP plasmid using droplet microfluidics-prepared (pink) and vortexing-prepared (purple) lipoplexes following the standard lipofection protocol. (D) The average lipofection efficiencies of K562 cells, as indicated by the percentages of

EGFP positive cells, transfected via bulk lipofection protocol using either vortexing-prepared (▩) or droplet microfluidics-prepared (▨) lipoplexes, and via droplet lipofection using either a straight mixing channel (▦) or a winding mixing channel (▨). (E) Numerical simulation showing the symmetric and steady vortices when droplets moving in the straight channel. (F) Numerical simulation illustrating the asymmetric and constantly changing vortices during droplet advection in the winding channel. (G) Fluorescence intensity histogram of 1000 live single K562 cells analyzed via flow cytometry 48 hr after transfection with pcDNA3-EGFP plasmid using our droplet-lipofection platform with a winding channel (yellow) and a modified platform with an equal-length straight channel (orange). Scale bar: 50 μm

Cell deformation at the droplet pinch-off

As shown in Fig. 5.3A and Movie 5.3, an originally round and spherical suspension cell was deformed and stretched after passing through the droplet generation pinch-off orifice in our platform, since it was exposed to rapid constriction and shear. The shear stress at the droplet pinch-off was as high as 5.14×10^2 dyne/cm^2 as calculated by numerical simulation (Fig. 5.3B and Movie 5.4). Previous research has demonstrated that transient membrane disruptions or holes are caused by the rapid mechanical deformation of a cell, as it passes through a constriction smaller than the cell diameter or is subjected to high shear stresses. The degree of disruption and the size and frequency of the holes are determined by the imposed shear and compressive forces.[92, 110, 111] The membrane permeability is improved as a result, and many intra-cellular delivery approaches are developed based on this phenomenon. For example, Hallow et al. demonstrated successful intracellular delivery of 150~2000 kDa dextran molecules at the applied shear stress of 130 dyne/cm^2,[110] and Han et al. achieved transfection by squeezing cells through 4-μm physical constrictions.[111] Among the 3 barriers of lipoplex-mediated gene delivery, i.e., the cell, endosomal and nucleus membranes, our platform was capable of overcoming the cell membrane barrier by increasing membrane permeability through cell deformation at the droplet pinch-off.

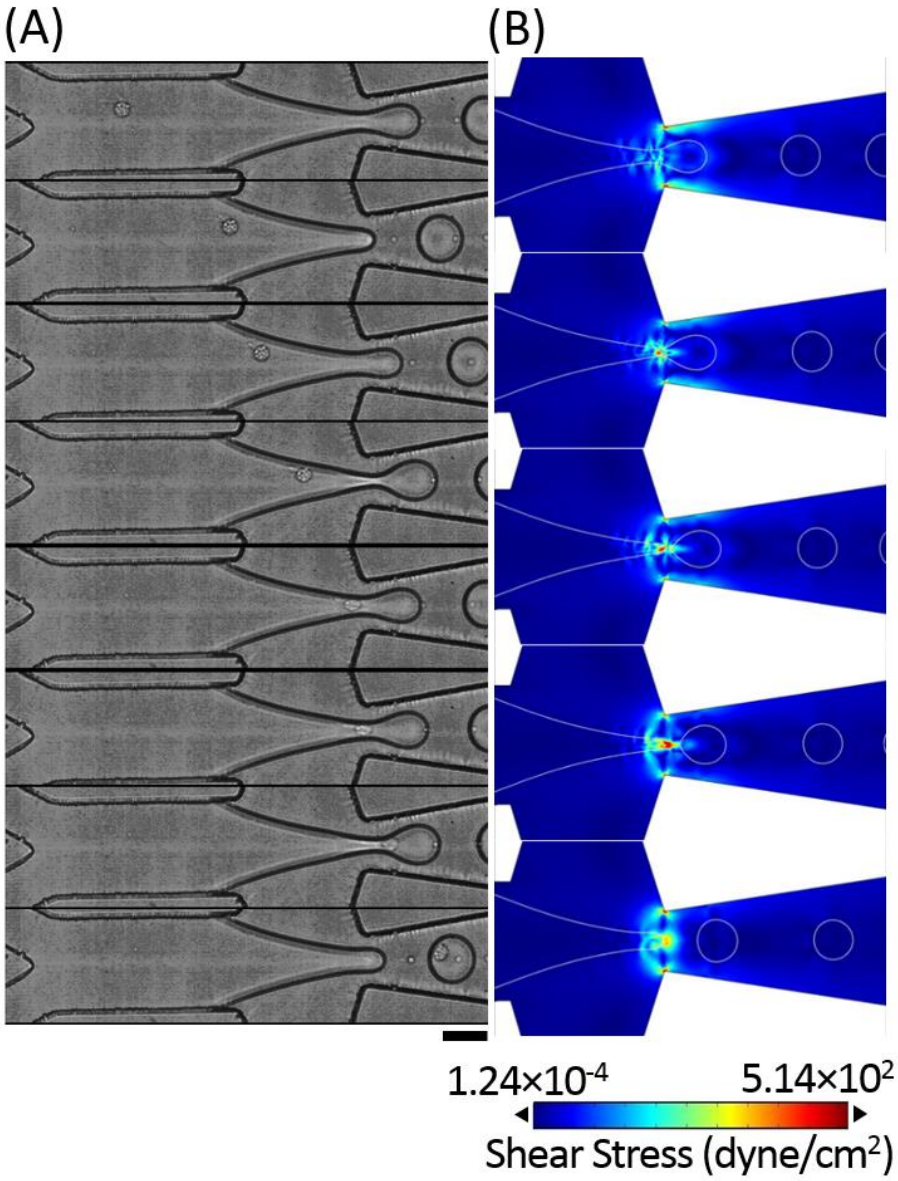

Figure 5.3 Cell deformation after experiencing the shear stress when squeezing through the droplet generation pinch-off.
(A) Time-lapse images showing the deformation of a K562 cell when it passed through the pinch-off of the flow-focusing droplet generation orifice. The pictures were taken at a frame rate of 45000 pictures per second. (B) Time-lapse images showing the shear stress at the pinch-off during the droplet generation calculated by numerical simulation. Scale bar: 50 μm.

Increased transfection efficiency and consistency for suspension cells

To compare the transfection efficiency between the droplet microfluidics-based single-cell lipofection and the conventional bulk lipofection, 3 types of suspension cells, i.e., K562, THP-

1, and Jurkat, were transfected via both approaches and analyzed by flow cytometry 48 hr after transfection with the pcDNA3-EGFP plasmid. As shown in the fluorescence intensity (x-axis) versus cell count (y-axis) plots of every 1,000 live transfected single cells for each cell lines (Fig. 5.4A), the droplet-lipofection histogram (yellow) was significantly shifted towards a higher fluorescence intensity compared to the bulk-lipofection histogram (purple), which demonstrated an overall higher expression level of the enhanced green fluorescence protein (EGFP), and therefore a higher transfection efficiency for the droplet-lipofection group. The exact transfection efficiencies were calculated and compared in Fig. 5.4C. Using our platform, the transfection efficiency increased from 2.3±0.4% to 52.5±5.7% for Jurkat cells, from 3.8±0.5% to 46.3±5.4% for THP-1 cells, and from 4.8±0.9% to 51.8±3.3% for K562 cells. In terms of cell viability (Fig. 5.4D), for Jurkat and K562 cells, there was no significant difference between the droplet lipofection (73.0±3.3%, 80.2±4.6%) and the bulk method (72.9±0.8%, 84.2±1.2%); and the viability of THP-1 cells transfected by droplet lipofection (67.8±3.7%) was slightly lower compared to those transfected with the bulk method (88.6±7.6%), which was probably due to the reason that THP-1 cells were sensitive to the surfactant Pluronic F-68 added in the cell suspension. But overall, our platform has realized a ~10 times increase in lipofection efficiency for hard-to-transfect suspension cells with a competitive cell viability compared to the standard bulk approach. We also ran HeLa cells through our droplet-lipofection device to transfect them with the same pcDNA3-EGFP plasmid, as an examination of our platform's performance on adherent cells, which are easier to transfect compared to suspension cells (Appendix C). There was a clear increase in transfection efficiency when using droplet lipofection (75.5±4.6%) compared to using the conventional bulk lipofection protocol (35.1±3.6%), which supported our hypothesis that rapid cell-

squeezing through droplet pinch-off together with chaotic mixing in the confined microdroplet improved transfection efficiency. However, the increase in lipofection efficiency for HeLa cells was not as significant as compared to suspension cells, which was probably due to the reason that HeLa cells are adherent cells, suspending them inside droplets is not as compatible as culturing them on the substrate for their appropriate function.

Previous efforts have been reported on transfection in droplet microfluidics platform. Chen et al. co-encapsulated a single cell with bulk-prepared PolyFect/DNA complexes in picoliter droplets, and achieved a transfection efficiency comparable to bulk transfection.[27] Benefit from the chaotic advection and cell-squeezing through the droplet pinch off, our platform enabled ~10 times higher transfection efficiency than bulk. Chen et al. also indicated that transfection benefited from the microscale confinement via having a higher probability for cell/complexes interaction which was coherent with our hypothesis, as they observed an increase in transfection efficiency for smaller droplets compared to bigger droplets. Zhan et al. passed droplets co-encapsulating single cells and DNAs through paired flat electrodes which replaced the pulse generator in bulk electroporation.[78] Their reported transfection efficiency (11% for CHO-1 cells) was relatively low, due to the reason that the oil phase was an insulator so that the electric field applied to the encapsulated cell was limited, and the field intensity was highly dependent on the relative location between the cell and the electrodes at the momentum when the droplet was in contact with the electrodes.

Our platform has also demonstrated a better performance compared with many other reported non-viral methods. Marit et al. cultured hematopoietic cells (TF-1, KG1a, and K562)

in adherent to a stromal (MS-5 cell line)/fibroblast (NIH-3T3 cell line) monolayer to increase the lipofection efficiency, but the reported transfection efficiency was only 11.2~25% (mean 18.3%) and complicated cell purification procedures were needed.[24] Zhao et al. achieved a 19~32% transfection efficiency for lymphoma/leukemia cells (K562, Karpas 299, and Jurkat) using ~200 nm nanocomplexes consisting of poly β-amino ester (PBAE) polymers and GFP plasmids, but this method required nanocomplex synthesis and cell pre-treatment by polybrene (a transduction enhancing reagent).[22] Sharei et al. enabled intracellular delivery by passing cells through a constriction 30~80% smaller than the cell diameter to mechanically deform the cells and generate transient holes on the cell membrane, which was a pure physical delivery method avoiding the use of vectors and bypassed endocytosis.[92] However, the demonstrated delivery molecules, i.e., 3kDa dextran, 70kDa dextran, quantum dots, carbon nanotubes, siRNA, were all smaller than plasmids. Therefore, although we deformed the cells at the droplet pinch off, we still incorporated Lipofectin to guarantee the intracellular delivery of the plasmids. Finally, Schakowski et al. utilized nucleofection, an electroporation-based technique, to transfect leukemic cells, but the cell viability was compromised for the efficiency.[112]

Another non-negligible result was that the histograms of the bulk transfected cells (Fig. 5.4A, purple) had a broad distribution ranging from a very low fluorescence intensity to an extremely high intensity, which was also verified by the single-cell bright-field and fluorescent images taken when they passed through the flow cytometer (Fig. 5.4B). On the contrary, cells transfected via droplet lipofection had a narrower fluorescence intensity distribution (Fig. 5.4A, yellow), and there were no super bright cells compared to the bulk method (Fig. 5.4E). Therefore, our platform provided a much lower cell-to-cell transfection

variability and a higher transfection consistency, which are important performance metrics in gene therapy. This desired transfection consistency was realized via droplet microfluidics and not the bulk process, as the cell-encapsulating micro-droplets generated on-chip were monodisperse with a size deviation less than 2%,[89] enabling quantitative and precise control of the reagents and manipulation applied to each individual cell.

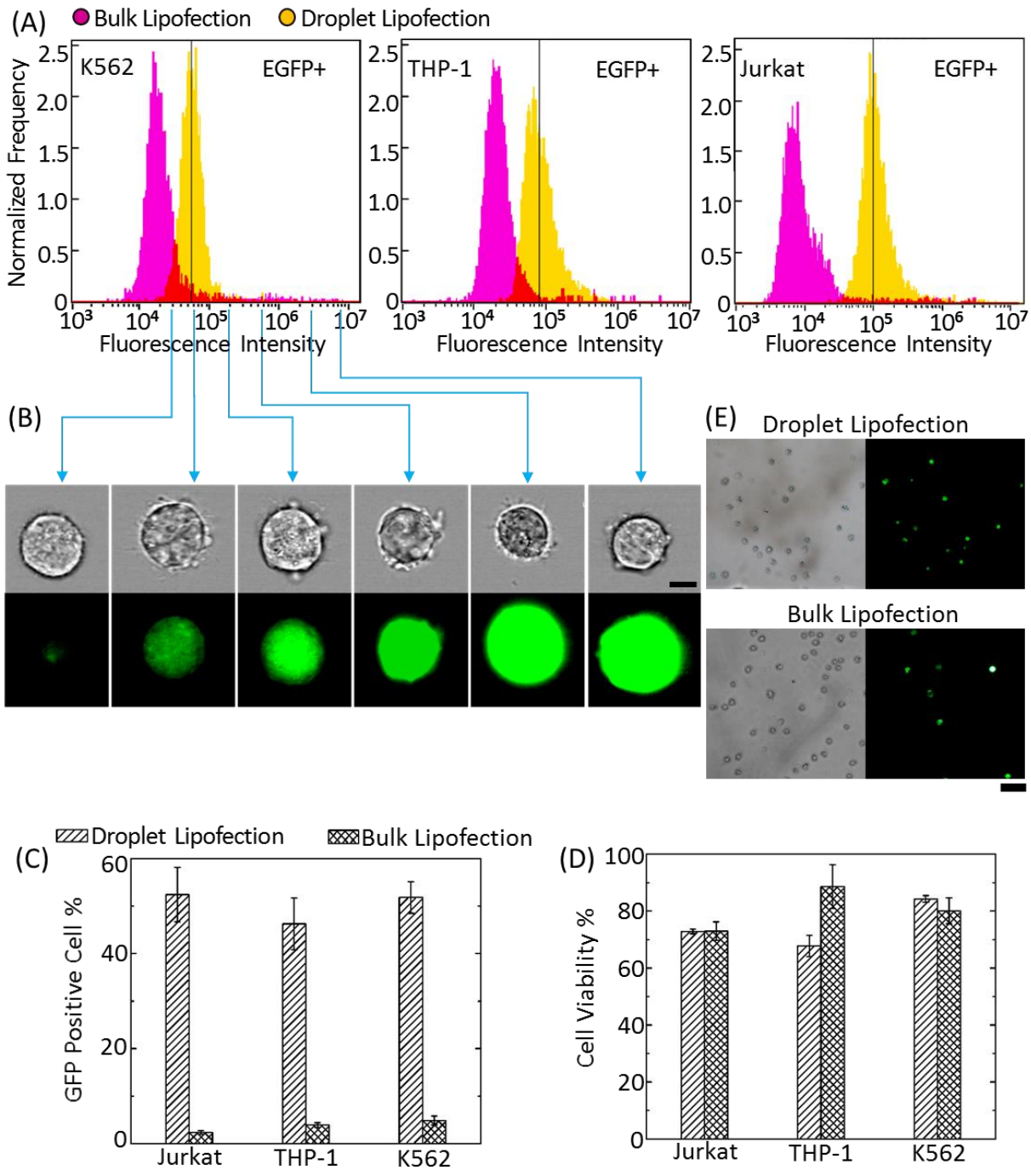

Figure 5.4 Transfection efficiency and consistency.
(A) Fluorescence intensity histograms of 1000 live single K562 (left), THP-1 (middle), and Jurkat (right) cells analyzed via flow cytometry 48 hr after transfection with pcDNA3-EGFP plasmid via either bulk lipofection using vortexing-prepared lipoplex (purple) or our droplet microfluidics-based single-cell lipofection platform (yellow). (B) Bright-field (top) and fluorescent (bottom) images of single EGFP-transfected K562 cells at different fluorescence intensity values. The images were taken when individual cells passed through the detector in the ImageStream flow cytometer. Cells in the bulk lipofection group had various fluorescence intensities over a broad range, whereas cells in the

droplet lipofection group had a much smaller intensity variation. Scale bar: 7 μm. (C) The average transfection efficiency and (D) cell viability were compared between our droplet lipofection approach and the conventional bulk lipofection as measured by the percentage of EGFP-positive cells and the percentage of propidium iodide-negative cells, respectively. Three repeating experiments were conducted for each cell line. (E) Bright-field and fluorescent images of K562 cells 48 hr after transfection of pcDNA3-EGFP plasmid via droplet lipofection (left) and bulk lipofection (right). Scale bar: 100 μm.

Targeted knockout of TP53BP1

We also explored the potential application of our platform in CRISPR-CAS9-mediated targeted gene editing. The CRISPR-CAS9 system has been broadly used in biomedical research and clinical applications because of its high-efficiency and high-specificity in targeting the locus of interest.[113] The 20-bp single-guide RNA (sgRNA) directs the CAS9 nuclease to introduce double-strand breaks at the sequence-specific genome locus,[96, 113] whereafter non-homologous end joining (NHEJ) DNA-repairing mechanism is triggered, which generates gene mutation at the target locus (Fig. 5.5A). The mutation will often block the normal gene expression and results in gene knockout. As a proof-of-concept, we have designed an sgRNA sequence (Fig. 5.5B) targeting the 2nd exon of TP53BP1 (tumor suppressor p53 binding protein 1, a critical protein involved in DNA damage responses) gene,[114, 115] and cloned it on and cloned it in between the U6 promoter sequence and the gRNA scaffold of the pLentiCRISPR v2 vector, which also carried the sequence of S. pyogenes CAS9 nuclease (Fig. 5.5C). The constructed plasmids were delivered into K562 cells via both droplet lipofection and the bulk method, and RT-qPCR of the targeted locus was performed for every 1,000 single cells 48 hr after the initial delivery. The RT-qPCR verification was repeated three times (Appendix C) with the representative amplification curves plotted in Fig. 5.5D. The Ct amplification curve of the bulk-lipofection group (black) was very close to that of the non-transfected group (red), whereas the amplification curve of the droplet-

lipofection group (blue) shifted towards a higher cycle-threshold (Ct) value, indicating a higher efficiency of gene-knockout. The Ct value was 31.3±0.2 for the non-transfected group, 31.8±0.3 for the bulk-lipofection group, and 33.9±0.6 for the droplet-lipofection group. Upon calibration using the established standard curve (Appendix C), wherein the correlation between the absolute number of TP53BP1 mRNA molecules (n), and the Ct value is: $Log_{10}{}^{n} = (41.35\text{-}Ct)/3.59$, the corresponding copy number of target mRNA molecules was 630±61 for the non-transfected group, 457±83 for the bulk-lipofection group, and 119±51 for the droplet-lipofection group. Therefore, the estimated TP53BP1 knockout efficiency through the delivery of pLentiCRISPR.v2-sgTP53BP1 plasmid was 27±13% when using bulk lipofection, and 81±8% when using droplet lipofection. However, as the Cells-to-CT™ 1-Step Power SYBR® Green Kit was used for this experiment, in which cell lysing, mRNA extraction and RT-qPCR were all integrated into one assay, there was unavoidable loss of mRNA molecules during cell lysing and mRNA extraction, which caused an over-estimation of gene knockout efficiency. Overall, the estimated knockout efficiency by droplet lipofection was satisfactory for this difficult-to-transfect lymphoma cell line that could not be achieved by current bulk lipofection methods.

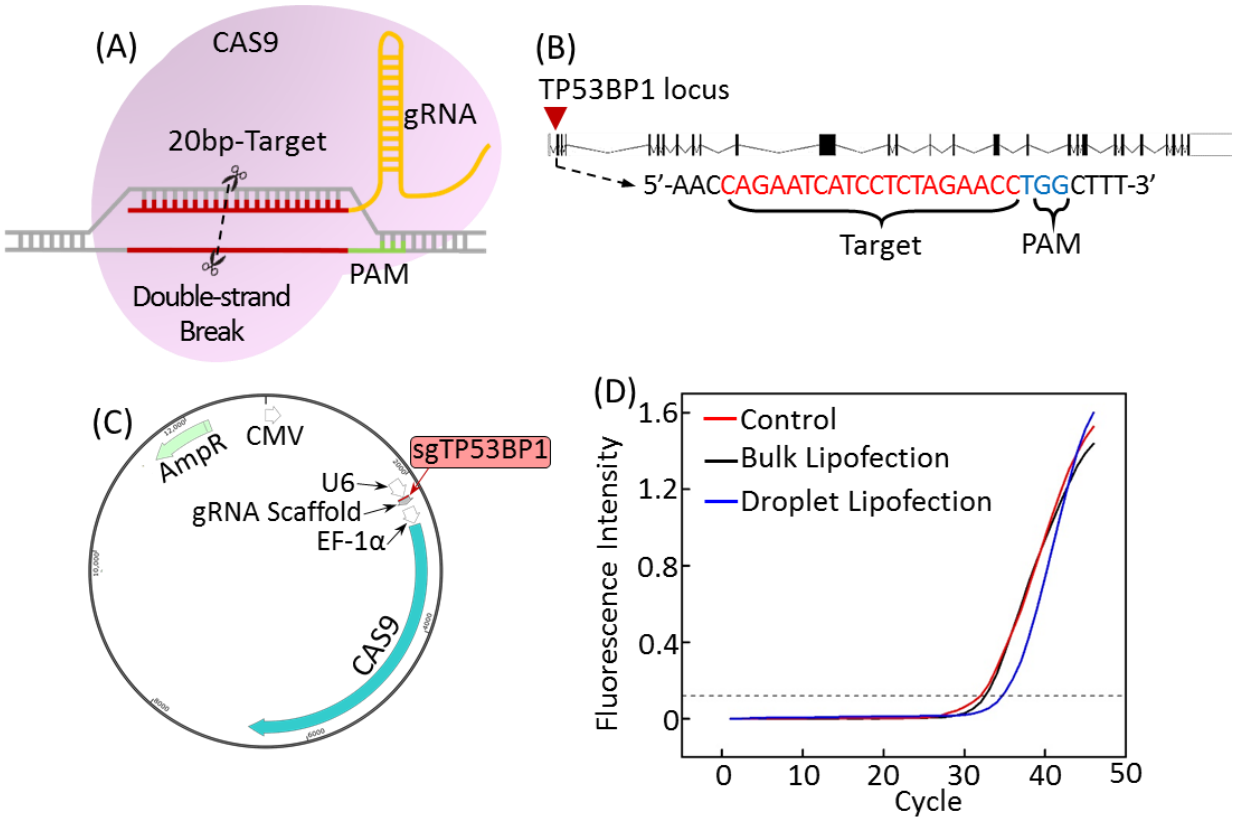

Figure 5.5 Targeted knockout of TP53BP1 in K562 cells through the delivery of pLentiCRISPR.v2-sgTP53BP1 plasmid via droplet lipofection.
(A) Schematic illustration of the targeted gene knockout via the CRISPR/CAS9 mechanism. (B) The sgRNA sequence and protospacer adjacent motif (PAM) sequence targeting the 2nd exon of TP53BP1 gene. (C) Annotated sequence map of the pLentiCRISPR.v2-sgTP53BP1 plasmid constructed for targeted knockout of the TP53BP1 gene in K562 cells. (D) The sample representative RT-qPCR amplification curves of every 1000 K562 cells after the TP53BP1 knockout by either droplet lipofection (blue) or bulk lipofection (black). The Ct value of the bulk-lipofection group was very close to that of the non-transfected group (red), whereas the Ct value of the droplet-lipofection group was significantly higher, indicating a higher efficiency of gene knockout.

CHAPTER 6: SINGLE-CELL PAIRING ARRAY FOR CELL-CELL INTERACTION STUDIES

For the last chapter before conclusion, we have explored the potential modification of the serpentine-shaped single-cell trapping array into a cell-pairing array, so that to study cell-cell interaction at the single-cell level.

Background

Cell-cell interaction plays a vital role in fundamental biological processes such as stem cell differentiation, adaptive immune responses, tumor progression, and embryogenesis.[116] For example, the interaction between sub-populations in the stem cell niche regulates the fate of stem cells.[117] Also, cancer immunology and immunotherapy are established based on the interaction between tumor cells, dendritic cells, and lymphocytes.[118] What is more, neural signals are transmitted via inter-cellular communication in the neural network.[119]

Despite the recognition of its importance, cell-cell interaction remains poorly understood due to its complexity. Conventional studies are often carried on mouse models and bulk cell co-culturing. As they are complex systems with various parameters, it is difficult to reveal the detailed mechanism of cell-cell interaction if only the bulk response is analyzed. On the contrary, if analyzing cell-cell interaction at the single-cell level by pairing the target single cells, complex irrelevant variables can be eliminated and the inter-cellular communication can be examined in detail. As a powerful tool for single-cell analysis, microfluidic technology has been explored for cell-cell interaction analysis at the single-cell level. However, besides complex designs/operations, current microfluidic cell-pairing

platforms are facing the unavoidable limitation of cross-pair interference,[120] as cell-pairs are kept in the shared microenvironment, which leads to high noise levels and false-positive readings, masking the true mechanism and population-heterogeneity.

Therefore in this chapter, we have established a microfluidic cell-pairing array based on the serpentine-shaped single-cell trapping array which pairs single cells in isolated compartments to avoid cross-pair interference in an easy-to-operate manner. As an initial proof of concept, the interaction between dendritic cells and cancer cells has been analyzed at the single-cell level using this cell-pairing array. We focus on dendritic cell - cancer cell interaction because understanding the cell-cell interaction of the immune system is the biological fundamental for cancer immunotherapy development, and especially the interaction between these two types of cells is a complex problem and still undefined. Both anti-tumor and pro-tumor discoveries of dendritic cells in responding to cancer cells have been reported, and actually, a lot of research shows contradictory findings.

Design and Working Principle

As illustrated in Fig. 6.1A, a cell-pairing unit is created by merging two single-cell traps facing the opposite direction to each other. The resulted cell-pairing array, a serpentine channel with 10 double-cell traps along each row (Fig. 6.1B), works by hydrodynamic sequential trapping and flow-induced cell deformability.[121] Traps in adjacent rows are in a mirrored configuration because of the serpentine shape. Each trapping unit, as shown in the SEM image (Fig. 6.1C), has one 1st-cell trap with a narrow opening facing the forward-flow direction, and one 2nd-cell trap with an opening facing the reverse-flow direction. The trap

size is similar to the target cell diameter to secure single-cell occupancy, and the two traps are connected by an opening in between to allow direct cell-cell contact for connexon formation. For mammalian cells with a diameter of ~15 μm, the empirically optimized channel height is 16 μm, trap size is 15 μm, narrow opening is 7 μm, and connection opening is 4 μm.

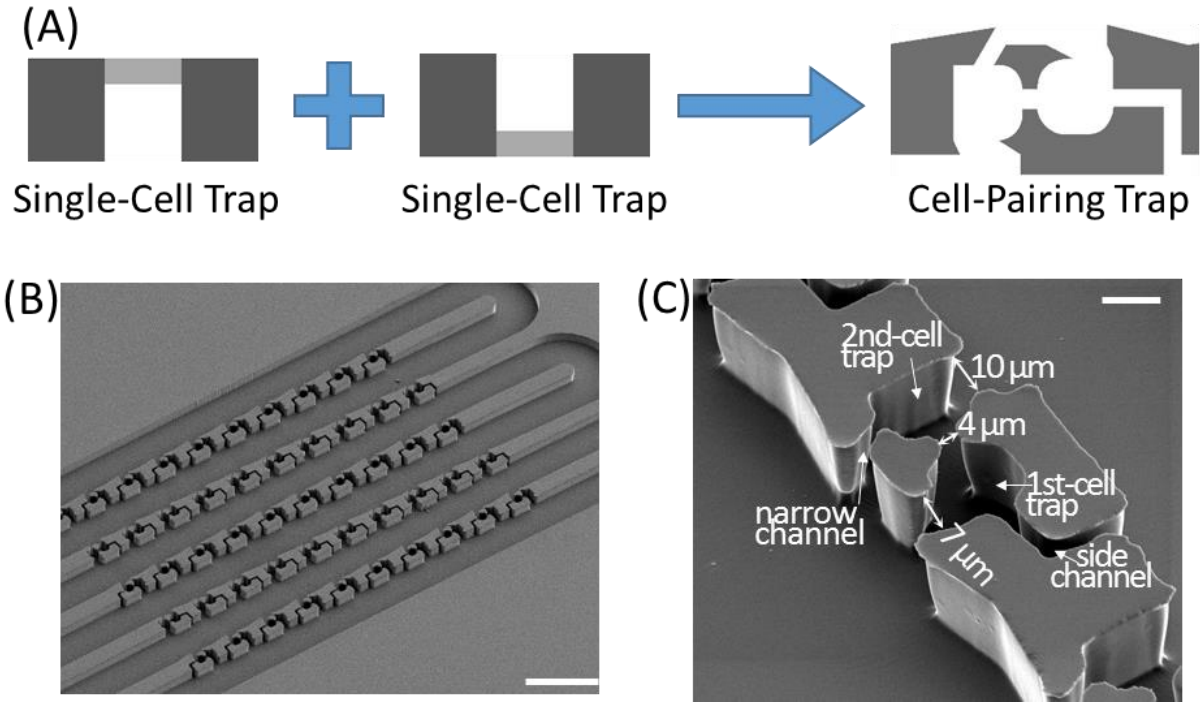

Figure 6.1 Design and structure of the cell-pairing array.
(A) The cell-pairing trap is created by combining two single-cell traps facing opposite directions. (B) SEM image of the cell-pairing array fabricated by PDMS replica molding. Traps in adjacent rows are mirrored as the channel is in a serpentine shape. Scale bar: 100 μm. (C) Zoom-in image showing the detailed structure of one trapping unit. Scale bar: 10 μm.

The first type of cells squeeze through the narrow openings when pushed and deformed by the strong forward-flow and sequentially enter the 1st-cell traps (Fig. 6.2A). A low-flow-rate reverse-flow introduces and pushes the second type of cells into the 2nd-cell traps with wider openings (Fig. 6.2B), while cells in the 1st-cell traps are locked by the narrow openings and not released. The double-cell pairs are then sealed by flowing oil phase

or hydrogel along the reverse-flow direction (Fig. 6.2C), so that each cell-pair is confined within an isolated compartment, blocking the interference from other pairs or the surrounding media.

In forward-flow, cells follow the laminar-flow streamlines (Fig. 6.2D) into the 1st-cell traps (Fig. 6.2E). The side channel (3.5-μm-wide) of the 1st-cell trap branches the flow to assist the cell to stay at the trap instead of squeezing through the connection opening. Although there are streamlines passing through the 2nd-cell trap's narrow channel (3.5-μm-wide) which faces the forward-flow direction, it is too narrow for cells to squeeze in. However, after all 1st-cell traps are filled, the reverse-flow streamlines pass through this narrow channel (Fig. 6.2F) and push the second type of cells into the 2nd-cell trap (Fig. 6.2G).

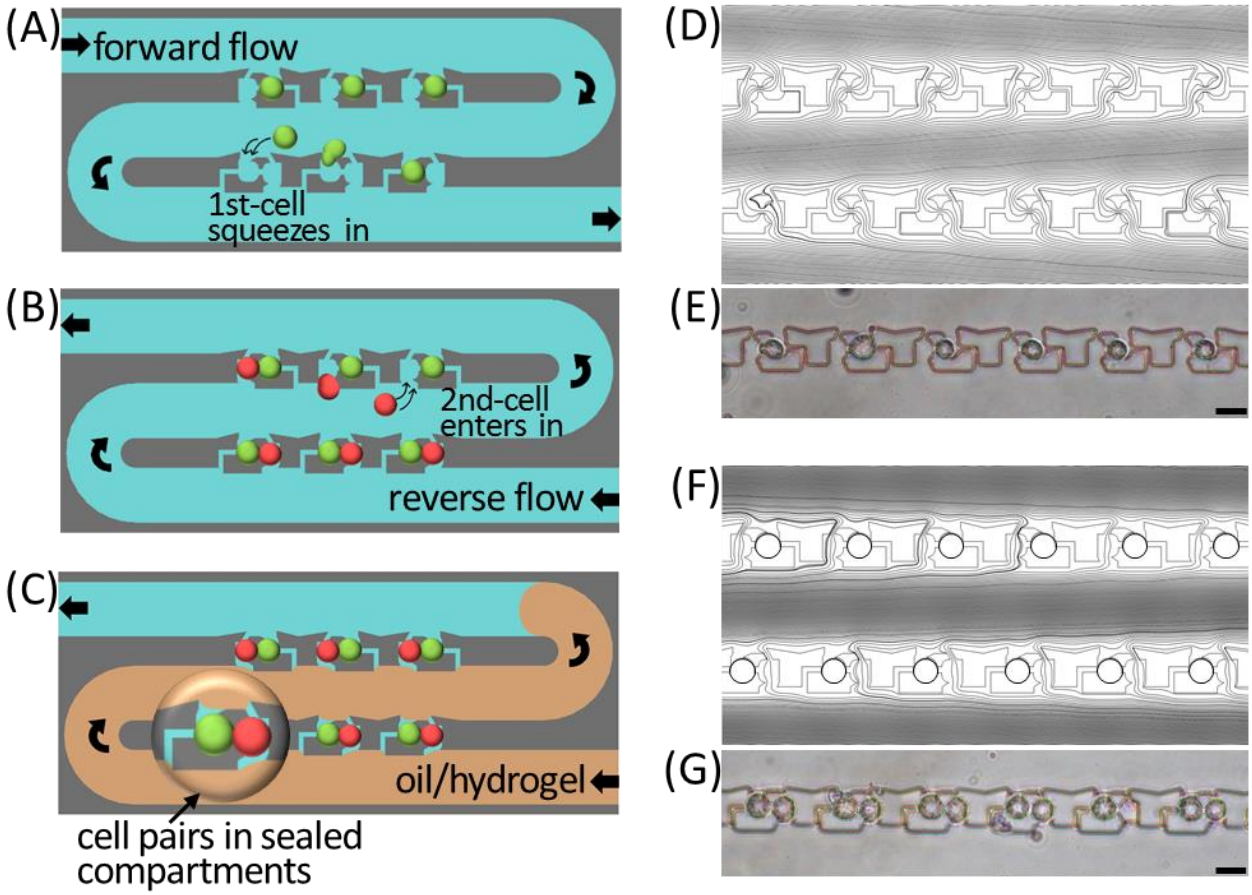

Figure 6.2 Operating principle of the cell-pairing array.
(A) The first type of cells (green) are loaded via the high-flow-rate forward-flow and squeeze into the

1st-cell traps. (B) The second type of cells (red) are loaded by the low-flow-rate reverse-flow and pushed into the 2nd-cell traps. (C) After the trapping array is filled by the double-cell pairs, oil phase or hydrogel is introduced via the reverse-flow to seal each trap by surface tension, so that every double-cell pairs are confined in isolated compartments. (D) Simulation of the forward-flow streamlines (mainly pass through the 1st-cell traps). (E) The first type of cells are pushed by the forward-flow and squeeze through the narrow openings into the 1st-cell traps. (F) Simulation of the reverse-flow streamlines when the 1st-cell traps are filled. (G) The second type of cells are pushed into the 2nd-cell traps, and cells in the 1st-cell traps are not released as they are locked by the 7-μm narrow openings. Scale bars: 20 μm.

Materials and Methods

Chip fabrication

The presented single-cell pairing array was fabricated via soft lithography following a similar procedure as explained in Chapter 2. As the minimum feature size was around 3~4 μm, chrome mask (instead of film mask) was used to guarantee the feature resolution.

Isolation and culture of human monocyte-derived dendritic cells

Dendritic cells were differentiated from monocytes isolated from healthy donors' blood. Peripheral blood mononuclear cells (PBMCs) were separated from blood and allowed to adhere to culture plates for 2 hr. Non-adherent cells were removed, whereas the resulting monocytes were cultured with granulocyte-macrophage colony-stimulating factor (GM-CSF) and IL-4 to initiate the differentiation into dendritic cells. Dendritic cells were collected after 6 days.

Hydrogel preparation

To establish long-term cell-cell interaction at the single-cell level within the microfluidic chip, paired single cells were cultured in photo-crosslinkable hydrogel gelatin methacryloyl

(GelMA, Sigma) compartments. Dry GelMA was dissolved in PBS at 10% w/v, and the photoinitiator, Irgacure 2959 (Sigma), was dissolved in dimethyl sulfoxide (DMSO) at 50% w/v. For every 200 μL experimental cell-in-GelMA suspension introduced into the chip, it consisted of 100 μL the above GelMA stock solution, 2 μL photoinitiator stock solution, and 98 μL cell-in-PBS suspension. As a result, the final concentration for GelMA was 5% w/v, and for the photoinitiator was 0.5% w/v.

Results and Discussion

Single-cell pairing efficiency

According to experimental observation and simulation validation, it is critical that the draining channel of the 1st-cell trap is on the side instead of at the bottom as illustrated in Fig. 6.3A. When the draining channel is at the bottom of the 1st-cell trap, as the reverse flow still goes through the draining channel, the 1st cell could still be pushed out although there is a constriction. By moving the draining channel from the bottom to the side of the 1st-cell trap, the reverse flow goes through the side of the 1st cell, and it is less likely that the 1st cell will be pushed out (Fig. 6.3B). The double-cell pairing efficiency with draining channel on the side is 52±10%, which is twice as high as that of the design with draining channel on the bottom (23±5%, Fig. 6.3C). Fig. 6.3D and E show the bright-field and fluorescent images of pairing single HeLa cells (Calcein-AM-labeled, green-fluorescent) and single K562 cells (CMTMR-labeled, orange-fluorescent) within FC-40 sealed separated compartments. Hela cells were loaded with a forward-flow rate of 5 μL/min, and K562 cells were loaded with a reverse-flow rate of 0.5 μL/min.

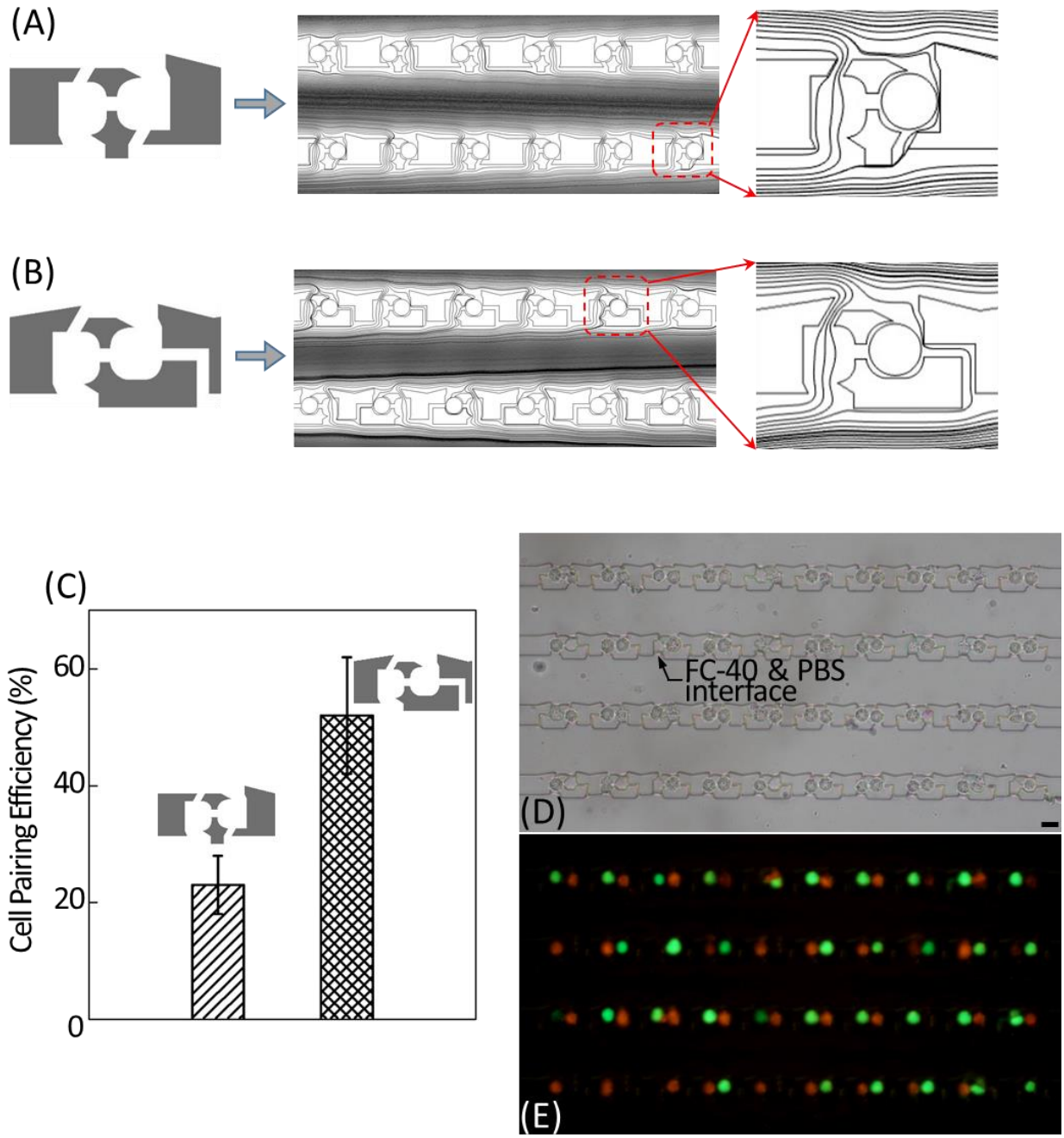

Figure 6.3 Pairing efficiency of the cell-pairing array.
(A) A cell-paring trap with the draining channel at the bottom of the 1st-cell trap. In this design, the reverse flow streamlines tend to push the 1st cell out with flow through the draining channel. (B) An optimized cell-pairing trap with the draining channel at the side of the 1st-cell trap. As the reverse flow goes through the side of the 1st cell, the 1st cell is less likely to be pushed out. (C) Comparison of the pairing efficiencies when the draining channel is on the bottom or on the side of the 1st-cell trap. (D) Bright-field and fluorescent images of single HeLa (green) and single K562 (orange) cells paired in the serpentine-shaped cell-pairing array. The double-cell pairs were sealed by the immiscible fluorocarbon oil FC-40. Scale bar: 20 μm.

Cell-pairs in hydrogel compartments

While sealing the cell-pairs by oil phase successfully creates isolated compartments, the oil sealing does not allow the continuous supply of media for long-term cell culturing, which is not suitable for continuously monitoring the dendritic cell – cancer interaction. To overcome this challenge, an alternative method to keep the paired cells in hydrogel compartments is developed using GelMA, gelatin modified by methacrylic anhydride. GelMA has shown biocompatibility for long-term cell culturing, and is photopolymerizable in a few seconds (Fig. 6.4A).[122] By simply shining the cell-pairing array with cells suspended in GelMA on a common fluorescence microscope, hydrogel compartments are generated in a second (as the mushroom shape highlighted by the white dotted line in Fig. 6.4B).

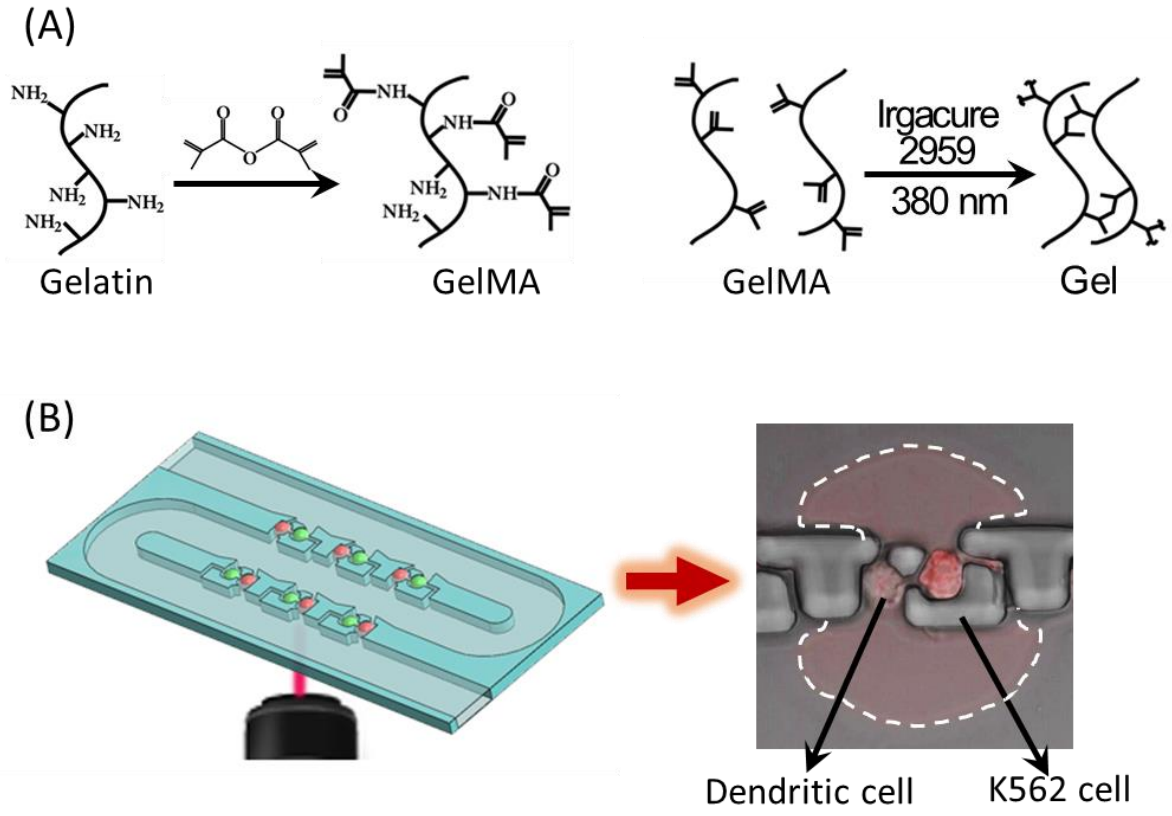

Figure 6.4 Paired cells in GelMA compartments.
(A) Composition and photo-crosslinking mechanism of GelMA. (B) Schematic illustration of creating GelMA compartments after dendritic cells and K562 cells are paired in the cell-pairing array.

Dendritic cell – cancer cell interaction at the single-cell level

K562 lymphoma cells in GelMA solution were introduced into the chip via forward flow, and dendritic cells suspending in GelMA were introduced by reverse flow. Each cell pairs were shined at 385 nm for 1 second and gelled. The paired cells in GelMA compartments were cultured for 12 hours inside the incubator with a continuous supply of RPMI medium. Thereafter, the metabolic patterns of dendritic cells were analyzed by fluorescence lifetime imaging microscopy following the same protocol explained in Chapter 3. As for the control group, dendritic cells were trapped in the single-cell array and cultured under the same condition in GelMA compartments.

The bright-field and auto-fluorescent images of the dendritic cells either paired with K562 lymphoma cells or in single-cell traps are plotted in Fig. 6.5A and B, with their corresponding phasor plots shown in Fig. 6.5C and D, respectively. As we can see from the phasor plots, there was a clear shift towards a shorter lifetime and a higher ratio of free-to-bound NADH for dendritic cells paired with K562 cells. This trend was also confirmed in the scatter plot (Fig. 6.5E), where the single-cell average phasor-FLIM values of 25 dendritic cells paired with lymphoma cells in comparison with 25 single dendritic cells were collected. The AUC value in distinguishing these two types of dendritic cells was 0.998 (Fig. 6.5F), showing the significant difference of the dendritic cells' metabolic status upon paring with cancer cells.

Based on the phasor-FLIM results of the single-cell paring array, it was clear that dendritic cells were more glycolytic upon pairing with cancer cells. To explore whether this metabolic shift was correlated with immunogenic or immunosuppressive responses of dendritic cells to cancer cells, surface-marker expression analysis was carried on dendritic

cells after bulk overnight co-culture with K562 cells (since the paired single cells were not easy to be retrieved from the cell-pairing array). According to the flow cytometry histograms (Fig. 6.5G), after bulk overnight co-culture with K562 cells, dendritic cells showed up-regulation of HLA-DR (Human Leukocyte Antigen – DR isotype, an MHC-II receptor responsible for the antigen presenting of dendritic cells to activate T cells), CD86, and CD80 (CD86 and CD80 are co-stimulatory proteins for dendritic cells to activate T cells). As these are surface markers expressed by dendritic cells upon activation,[123] one possible explanation could be that dendritic cells are activated upon pairing with K562 cells overnight, and dendritic cells rely on glycolysis for the rapid generation of ATP for antigen presenting and cytokine biosynthesis.[124] However, further experiments on gene and cytokine expressions are necessary to validate the correlation between the metabolic shift and the immuno-responses.

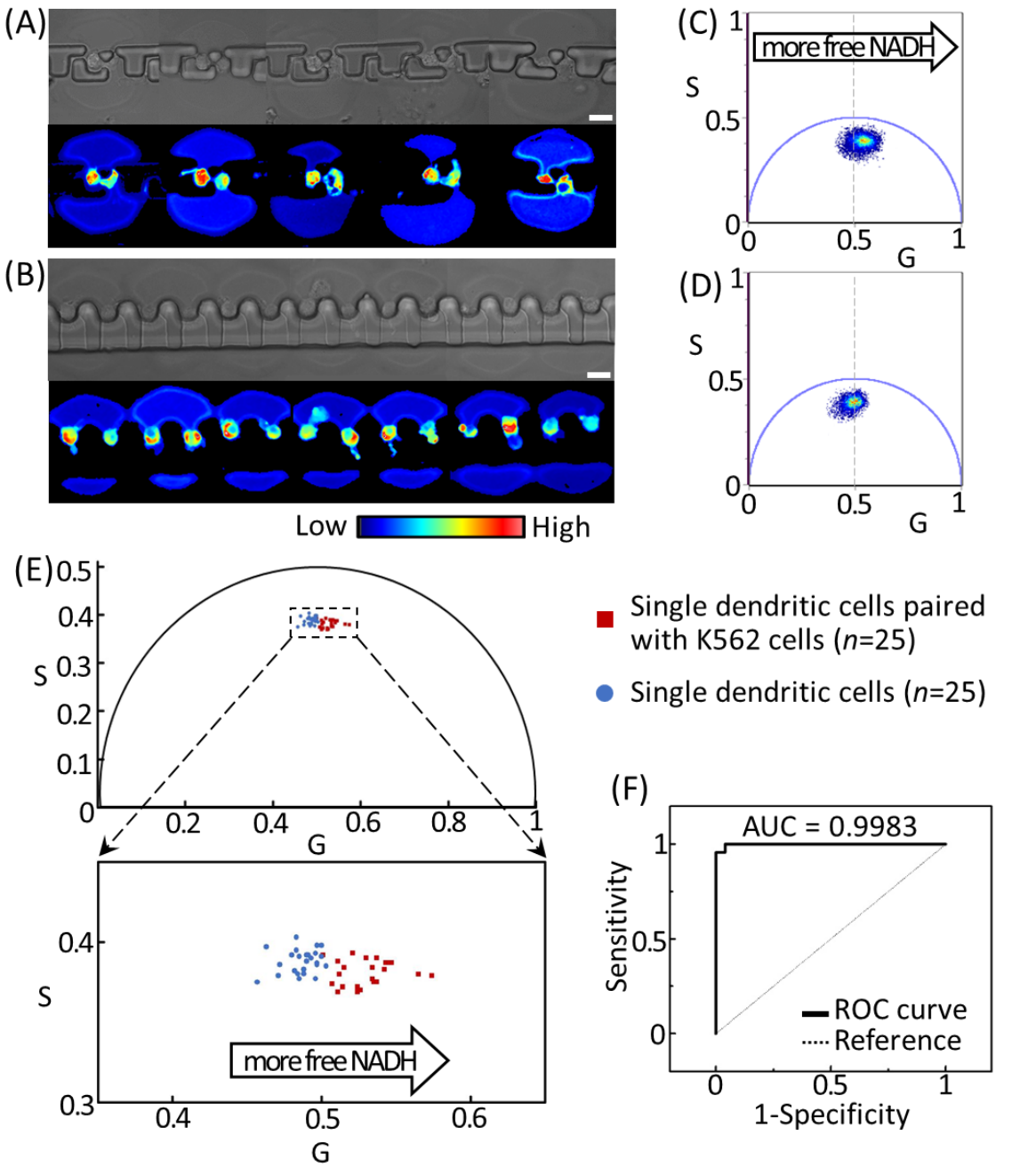
(A)
(B)
Low
High
(C)
more free NADH
S
G
(D)
(E)
Single dendritic cells paired with K562 cells (n=25)
Single dendritic cells (n=25)
more free NADH
(F)
AUC = 0.9983
Sensitivity
1-Specificity
ROC curve
Reference
(G)
Dendritic cells
Dendritic cells co-cultured with K562 cells
HLA-DR
CD86
CD86
% of the Cell Population
Fluorescence Intensity

Figure 6.5 Phasor-FLIM analysis of dendritic cells paired with K562 cells or in single-cell traps. Bright-field and auto-fluorescent images of the dendritic cells paired with K562 lymphoma cells in the cell-paring array (A) and single dendritic cells (B) after 12 hr on-chip culturing in GelMA compartments. Phasor plots of the NADH auto-fluorescence lifetime signatures of dendritic cells paired with K562 cells (C) and single dendritic cells (D). (E) Scatter plot of the average g and s phasor-FLIM values of individual dendritic cells either paired with K562 cells (red) or in the single-cell trapping array (blue). (F) The ROC curve differentiating the paired *vs.* un-paired dendritic cell pupations based on their phasor-FLIM values. The AUC value > 0.99, indicating a significant difference. (G) Flow cytometry analysis of HLA-DR, CD86, and CD80 expressions of dendritic cells after bulk overnight co-culture with (red dashed line) and without (blue dashed line) K562 cells.

Further Improvement of the Chip and Experimental Design

The double-cell pairing efficiency has been achieved so far is 52±10%, which still requires further effort for optimization. One problem with the current design is that, during the forward-flow cell loading, an extra cell is often trapped at the narrow draining channel of the 2nd-cell trap. Although this narrow channel is only 3.5-μm wide which is much smaller than the cell diameter, due to the intrinsic deformability of the mammalian cell, part of the cell can still squeeze and get stuck in the narrow channel. One possible solution for this problem is to reduce the height of the narrow draining channel by fabricating the master mold via two-layer photolithography. If the height of the narrow draining channel is adjusted to ~4 μm, which is 1/4 of the current height (16 μm), the resistance of the narrow channel will be increased (resulting in less flow pushing through), and the space for the cell to get stuck will also be reduced. In this way, the chance that an extra cell is stuck at the narrow draining channel during forward flow would be reduced.

Another limitation of the current platform is that the photo-crosslinking of the GelMA compartment is performed one by one, which is not suitable for high-throughput analysis. This can be solved by inserting a mask in the light pathway of the inverted microscope (e.g., in the filter lens slot). The mask should have an array of transparent dots matching the

arrangement of the cell-pairing array, so that all the cell-pairing sports can be gelled together. The dimension of the transparent dots needs to be calibrated according to the lens magnification scale.

Since we could not extract the paired single cells from the cell-pairing array so far to analyze their surface-marker expressions, we attempted to use bulk cell-culturing to find a clue. As a result, the cellular heterogeneity and specific characteristics of individual cells were not fully revealed. The ideal analysis method would be using the DENT probe to extract the marker genes' mRNAs of individual dendritic cells which are paired with single K562 lymphoma cells. In this way, we can correlate the gene-expression results with the FLIM measurement for every single cell. This would be a truly correlated microfluidic single-cell phenotype-to-genotype analysis, but has not yet been realized due to time limitation.

CHAPTER 7: CONCLUSION AND FUTURE PERSPECTIVE

To summarize, in this thesis we have developed an integrated microfluidic system capable of high-throughput single-cell manipulation and analysis from phenotype to genotype. This system is established upon a high-throughput microfluidic trapping array with up to 76800 highly-packed microwells, which can be filled in 5 min using 2% hematocrit blood with a single CTC/WBC occupying efficiency of > 80% and simultaneous RBC filtration.

By imaging the single-cell array at 740 nm two-photon excitation and getting the cells' fluorescence-lifetime signatures, the trapped single leukemia cells (THP-1, Jurkat and K562) were successfully distinguished from WBCs in the phasor-FLIM map based on their significant shift towards shorter fluorescence lifetime and a higher ratio of free/bound NADH due to the metabolic dependence on glycolysis. The quantitative separation between leukemia cells and WBCs (AUC = 1.00) as well as between different leukemia cell lines was achieved with good sensitivity and specificity (AUC > 0.95) via a multiparametric scheme comparing the 8 parameter-spectra of the phasor-FLIM signatures. This is the first time that single-cell imaging by the auto-fluorescence lifetime of metabolites is applied to CTC analysis, and has achieved rapid and label-free individual-leukemia-cell screening at a speed of 100 cells/min. Phasor-FLIM based screening on a high-density trapping array is label-free, cell-safe, quantitative, and has the potential to screen blood in clinical volumes through channel parallelization. It is expected to be widely used in early leukemia/tumor detection, tumor heterogeneity characterization, and personalized medicine.

By sealing the single-cell trapping array with an ultra-thin (~1 μm) PDMS membrane, the modified AFM probe, DENT, was able to penetrate through the membrane after aligned

with the target cell of interest, and extract mRNA molecules from cytoplasm with minimal damage by dielectrophoresis upon the application of AC field. The mRNA probing efficiency, which is related to the amplitude of the applied AC field, was analyzed based on the RT-qPCR results of 3 housekeeping genes, i.e., ACTB, GAPDH, and HPRT, after *in situ* mRNA extraction, with the post-probing cell viability verified by Calcein AM staining. Fingerprinting of the cell-specific marker-genes (EpCAM, HER2, and CD45), as well as differentiating SK-BR-3 breast cancer cells from U937 monocytes, were also successfully achieved using this platform. The integration of an external single-cell mRNA AFM DENT probe and the membrane-sealed microfluidic single-cell trapping array enables a powerful label-free and non-destructive single-cell probing platform with the capability of multi-step on-chip cell processing, which will have a myriad of applications such as drug response monitoring and cancer diagnostics.

As explained in Chapter 2, the single-cell occupying efficiency is independent of flow rate. Therefore, this single-cell trapping and FLIM imaging/mRNA probing unit can be easily integrated with other upstream microfluidic sample-processing units operating at various flow rates to form a sample-to-answer μTas platform. For solid tumors, a tissue dissociation unit could be integrated, such like digesting tumor tissues into cell suspensions via hydrodynamic shear forces and enzymatic canalization.[125] In terms of liquid biopsies like blood, a whole blood separation unit could be integrated, such as the contraction-expansion array which separates CTCs from whole blood by inertial microfluidics.[16]

Selective retrieving of the identified single cells of interest from the trapping array is also of great interest. There have been several approaches reported in the literature, such as laser-induced bubble formation to displace a trapped cell,[126] localized negative dielectrophoretic force,[127] and selective opening or closing of individual traps by

microfluidic OR logic gate[128]. By incorporating the selective releasing technique with the single-cell trapping array, targeted cells of interest can be collected for further culturing and analysis.

After identifying single CTCs from WBCs based on their metabolic differences and marker-gene expressions, the next step is to correct the aberrant genes in cancer cells, which is the typical procedure in cell therapy. However, suspension cells like the leukemia cells identified in the single-cell array, are extremely difficult to transfect using the existing protocol. Therefore, in this thesis, we have established a droplet-microfluidic single-cell transfection platform for lipoplex-mediated efficient and consistent plasmid delivery for hard-to-transfect suspension cells. In this platform, single cells are co-encapsulated with cationic lipids and plasmids in monodisperse micro-droplets, and chaotic mixing results in monodisperse lipoplexes for consistent and efficient transfection. Using this approach, the pcDNA3-EGFP plasmid delivery efficiency was improved from ~5% to ~50% for all of the three tested suspension cell lines, i.e., K562, THP-1, Jurkat, with significantly reduced cell-to-cell variation, compared to the bulk method. This methodology has also been tested for CRISPR/CAS9-mediated gene editing, and achieved a ~70% knockout of TP53BP1 gene in K562 cells. The three reasons that this droplet-microfluidic approach has an order of magnitude higher lipofection efficiency and much lower transfection variability (higher consistency) are: 1) the chaotic mixing generates monodisperse lipoplexes in the proper size range for endocytosis, 2) confining a single-cell with lipoplexes in a picoliter-droplet plus chaotic advection overcome the diffusion limitations in the bulk reaction volume while generating intensive lipoplex-cell collision, and 3) the membrane permeability is increased due to cell deformation resulted from the exerted shear stress as it passes through the

droplet pinch-off orifice. Lipoplex-mediated single-cell transfection via droplet microfluidics would have broad applications in gene therapy and regenerative medicine by providing significantly higher transfection efficiency and lower cell-to-cell variation for hard-to-transfect cells such as lymphoma and hematopoietic cells.

Further optimization of the CRISPR/CAS9 protocol on this platform is still needed, especially for clinically significant genes and cell types. A future perspective would be implanting this technique in CAR-T cell therapy, transfecting isolated T lymphocytes with the CAR gene using this single-cell droplet-lipofection approach. It would also be meaningful if the cell-encapsulating droplets can be gelled with the complete removal of the oil shell after transfection. This way, cells can be cultured and preserved in the hydrogel beads.

Apart from analyzing individual cells, microfluidic cell trapping array can also be employed for studying cell-cell interaction at the single-cell level. For this purpose, the single-cell trapping array is modified into a cell-pairing array, which pairs single cells in isolated compartments in an easy-to-operate manner. The dendritic cells' response to cancer cells was analyzed in this cell-pairing array with GelMA compartments, and results showed that dendritic cells became more glycolytic upon pairing with K562 lymphoma cells. While the detailed mechanism of this metabolic switch remains to be further identified by cytokine secretion experiments, the cell pairing array has demonstrated its capability for cell-cell interaction studies, and can be adapted in various cell-cell interaction studies, such as NK-T cell vs. tumor cell, dendritic cell vs. T cell, neural stem cell interactions, cardiomyocyte interactions, etc.

One innovative point of this thesis is integrating the state-of-art analytical tools (e.g., FLIM, DENT), which are powerful but not originally established for standard single-cell

analysis, with the powerful single-cell manipulation capability of microfluidics (e.g., single-cell trapping, encapsulation, pairing), so that innovative, cell-friendly, and high-throughput single-cell analysis can be established. Based on this concept, many cutting-edge techniques can be adapted for single-cell analysis leveraging the single-cell handling capability of microfluidic technology.

As stated in the introduction session, single-cell analysis has the power to reveal population heterogeneity and specific characteristics of individual cells. In the meantime, microfluidic technologies are capable of accomplishing single-cell analysis in a low cost, high throughput, and automated manner. Therefore, microfluidic single-cell analysis is expected to revolutionize disease diagnostics and personalized medicine. While the author here looks forward to having the presented microfluidic platforms implanted in real diagnostic and treatment settings, it is also the author's desire to inspire researchers in the field as well as the general public.

BIBLIOGRAPHY

[1] A. P. Patel, I. Tirosh, J. J. Trombetta, A. K. Shalek, S. M. Gillespie, H. Wakimoto, D. P. Cahill, B. V. Nahed, W. T. Curry, R. L. Martuza, *Science* **2014**, *344*, 1396.

[2] D. K. Singh, C. J. Ku, C. Wichaidit, R. J. Steininger, L. F. Wu, S. J. Altschuler, *Molecular systems biology* **2010**, *6*, 369.

[3] H. Yin, D. Marshall, *Current opinion in biotechnology* **2012**, *23*, 110.

[4] D. D. Carlo, L. P. Lee, Dynamic single-cell analysis for quantitative biology. ACS Publications: **2006**.

[5] D. Ramsköld, S. Luo, Y.-C. Wang, R. Li, Q. Deng, O. R. Faridani, G. A. Daniels, I. Khrebtukova, J. F. Loring, L. C. Laurent, *Nature biotechnology* **2012**, *30*, 777.

[6] C. Alix-Panabières, K. Pantel, *Cancer discovery* **2016**, *6*, 479.

[7] M. Yu, S. Stott, M. Toner, S. Maheswaran, D. A. Haber, *The Journal of Cell Biology* **2011**, *192*, 373.

[8] B. Alberter, C. A. Klein, B. Polzer, *Expert review of molecular diagnostics* **2016**, *16*, 25.

[9] F. Crick, *Nature* **1970**, *227*, 561.

[10] G. M. Whitesides, *Nature* **2006**, *442*, 368.

[11] K. Chung, C. A. Rivet, M. L. Kemp, H. Lu, *Analytical chemistry* **2011**, *83*, 7044.

[12] A. K. White, M. VanInsberghe, I. Petriv, M. Hamidi, D. Sikorski, M. A. Marra, J. Piret, S. Aparicio, C. L. Hansen, *Proceedings of the National Academy of Sciences* **2011**, *108*, 13999.

[13] A. M. Klein, L. Mazutis, I. Akartuna, N. Tallapragada, A. Veres, V. Li, L. Peshkin, D. A. Weitz, M. W. Kirschner, *Cell* **2015**, *161*, 1187.

[14] S. L. Stott, C.-H. Hsu, D. I. Tsukrov, M. Yu, D. T. Miyamoto, B. A. Waltman, S. M. Rothenberg, A. M. Shah, M. E. Smas, G. K. Korir, *Proceedings of the National Academy of Sciences* **2010**, *107*, 18392.

[15] A.-E. Saliba, L. Saias, E. Psychari, N. Minc, D. Simon, F.-C. Bidard, C. Mathiot, J.-Y. Pierga, V. Fraisier, J. Salamero, *Proceedings of the National Academy of Sciences* **2010**, *107*, 14524.

[16] M. G. Lee, J. H. Shin, C. Y. Bae, S. Choi, J.-K. Park, *Analytical chemistry* **2013**, *85*, 6213.

[17] E. Shapiro, T. Biezuner, S. Linnarsson, *Nature Reviews Genetics* **2013**, *14*, 618.

[18] Å. Segerstolpe, A. Palasantza, P. Eliasson, E.-M. Andersson, A.-C. Andréasson, X. Sun, S. Picelli, A. Sabirsh, M. Clausen, M. K. Bjursell, *Cell metabolism* **2016**, *24*, 593.

[19] A. J. Hughes, D. P. Spelke, Z. Xu, C.-C. Kang, D. V. Schaffer, A. E. Herr, *Nature methods* **2014**, *11*, 749.

[20] E. Uchida, H. Mizuguchi, A. Ishii-Watabe, T. Hayakawa, *Biological and Pharmaceutical Bulletin* **2002**, *25*, 891.

[21] R. Maurisse, D. De Semir, H. Emamekhoo, B. Bedayat, A. Abdolmohammadi, H. Parsi, D. C. Gruenert, *BMC biotechnology* **2010**, *10*, 9.

[22] N. Zhao, J. Qi, Z. Zeng, P. Parekh, C.-C. Chang, C.-H. Tung, Y. Zu, *Journal of controlled release* **2012**, *159*, 104.

[23] S. Palchetti, D. Pozzi, C. Marchini, A. Amici, C. Andreani, C. Bartolacci, L. Digiacomo, V. Gambini, F. Cardarelli, C. Di Rienzo, *Nanomedicine: Nanotechnology, Biology and Medicine* **2017**, *13*, 681.

[24] G. Marit, Y. Cao, P. Froussard, J. Ripoche, M. Dupouy, A. Elandaloussi, F. Lacombe, F. X. Mahon, H. Keller, M. Pla, *European journal of haematology* **2000**, *64*, 22.

[25] S. Brunner, T. Sauer, S. e. a. Carotta, M. Cotten, M. Saltik, E. Wagner, *Gene therapy* **2000**, *7*, 401.

[26] G. Esendagli, H. Canpinar, A. L. Dogan, M. Akkaya, E. Kansu, D. Guc, *Cytotechnology* **2009**, *61*, 45.

[27] H. N. Joensson, H. Andersson Svahn, *Angewandte Chemie International Edition* **2012**, *51*, 12176.

[28] S. H. Kim, T. Yamamoto, D. Fourmy, T. Fujii, *Small* **2011**, *7*, 3239.

[29] D. D. Carlo, L. Y. Wu, L. P. Lee, *Lab on a Chip* **2006**, *6*, 1445.

[30] T. J. Levario, M. Zhan, B. Lim, S. Y. Shvartsman, H. Lu, *Nature Protocols* **2013**, *8*, 721.

[31] H. Noguchi, G. Gompper, *Proceedings of the National Academy of Sciences* **2005**, *102*, 14159.

[32] M. E. Warkiani, B. L. Khoo, L. Wu, A. K. P. Tay, A. A. S. Bhagat, J. Han, C. T. Lim, *Nature protocols* **2016**, *11*, 134.

[33] P. Li, Z. Mao, Z. Peng, L. Zhou, Y. Chen, P.-H. Huang, C. I. Truica, J. J. Drabick, W. S. El-Deiry, M. Dao, *Proceedings of the National Academy of Sciences* **2015**, *112*, 4970.

[34] S. Shim, K. Stemke-Hale, A. M. Tsimberidou, J. Noshari, T. E. Anderson, P. R. Gascoyne, *Biomicrofluidics* **2013**, *7*, 011807.

[35] N. M. Karabacak, P. S. Spuhler, F. Fachin, E. J. Lim, V. Pai, E. Ozkumur, J. M. Martel, N. Kojic, K. Smith, P.-i. Chen, J. Yang, H. Hwang, B. Morgan, J. Trautwein, T. A. Barber, S. L. Stott, S. Maheswaran, R. Kapur, D. A. Haber, M. Toner, *Nature Protocols* **2014**, *9*, 694.

[36] F. A. Coumans, G. van Dalum, M. Beck, L. W. Terstappen, *PloS one* **2013**, *8*, e61770.

[37] M.-H. Park, E. Reátegui, W. Li, S. N. Tessier, K. H. K. Wong, A. E. Jensen, V. Thapar, D. Ting, M. Toner, S. L. Stott, P. T. Hammond, *Journal of the American Chemical Society* **2017**, *139*, 2741.

[38] W. Sheng, T. Chen, R. Kamath, X. Xiong, W. Tan, Z. H. Fan, *Analytical Chemistry* **2012**, *84*, 4199.

[39] J. M. Jackson, J. B. Taylor, M. A. Witek, S. A. Hunsucker, J. P. Waugh, Y. Fedoriw, T. C. Shea, S. A. Soper, P. M. Armistead, *Analyst* **2016**, *141*, 640.

[40] W. Li, Y. Zhang, C. P. Reynolds, D. Pappas, *Analytical chemistry* **2017**, *89*, 7340.

[41] M. Hassoun, J. Rüger, T. Kirchberger-Tolstik, I. W. Schie, T. Henkel, K. Weber, D. Cialla-May, C. Krafft, J. Popp, *Analytical and bioanalytical chemistry* **2018**, *410*, 999.

[42] A. Pallaoro, M. R. Hoonejani, G. B. Braun, C. D. Meinhart, M. Moskovits, *Acs Nano* **2015**, *9*, 4328.

[43] M. G. Vander Heiden, L. C. Cantley, C. B. Thompson, *science* **2009**, *324*, 1029.

[44] K. H. Vousden, K. M. Ryan, *Nature Reviews Cancer* **2009**, *9*, 691.

[45] B. K. Wright, L. M. Andrews, J. Markham, M. R. Jones, C. Stringari, M. A. Digman, E. Gratton, *Biophysical journal* **2012**, *103*, L7.

[46] M. A. Digman, V. R. Caiolfa, M. Zamai, E. Gratton, *Biophysical journal* **2008**, *94*, L14.

[47] C. Stringari, A. Cinquin, O. Cinquin, M. A. Digman, P. J. Donovan, E. Gratton, *Proceedings of the National Academy of Sciences* **2011**, *108*, 13582.

[48] S. Ranjit, A. Dvornikov, M. Levi, S. Furgeson, E. Gratton, *Biomedical optics express* **2016**, *7*, 3519.

[49] N. Ma, M. A. Digman, L. Malacrida, E. Gratton, *Biomedical optics express* **2016**, *7*, 2441.

[50] S. Ranjit, A. Dvornikov, E. Dobrinskikh, X. Wang, Y. Luo, M. Levi, E. Gratton, *Biomedical optics express* **2017**, *8*, 3143.

[51] S. Sameni, A. Syed, J. L. Marsh, M. A. Digman, *Scientific Reports* **2016**, *6*, 34755.

[52] A. Bai, A. Moss, S. Rothweiler, M. S. Longhi, Y. Wu, W. G. Junger, S. C. Robson, *Nature communications* **2015**, *6*, 8819.

[53] S. H. Jackson, S. Devadas, J. Kwon, L. A. Pinto, M. S. Williams, *Nature immunology* **2004**, *5*, 818.

[54] E. Hulleman, K. M. Kazemier, A. Holleman, D. J. VanderWeele, C. M. Rudin, M. J. Broekhuis, W. E. Evans, R. Pieters, M. L. Den Boer, *Blood* **2009**, *113*, 2014.

[55] H. Hwang, D.-H. Lee, W. Choi, J.-K. Park, *Biomicrofluidics* **2009**, *3*, 014103.

[56] B. Dura, M. M. Servos, R. M. Barry, H. L. Ploegh, S. K. Dougan, J. Voldman, *Proceedings of the National Academy of Sciences* **2016**, *113*, E3599.

[57] G. To'a Salazar, Y. Wang, G. Young, M. Bachman, C. E. Sims, G. Li, N. L. Allbritton, *Analytical chemistry* **2007**, *79*, 682.

[58] E. Z. Macosko, A. Basu, R. Satija, J. Nemesh, K. Shekhar, M. Goldman, I. Tirosh, A. R. Bialas, N. Kamitaki, E. M. Martersteck, *Cell* **2015**, *161*, 1202.

[59] M. Radmacher, R. Tillamnn, M. Fritz, H. Gaub, *Science* **1992**, *257*, 1900.

[60] K. Unal, J. Frommer, H. Kumar Wickramasinghe, *Applied physics letters* **2006**, *88*, 183105.

[61] O. Guillaume-Gentil, R. V. Grindberg, R. Kooger, L. Dorwling-Carter, V. Martinez, D. Ossola, M. Pilhofer, T. Zambelli, J. A. Vorholt, *Cell* **2016**, *166*, 506.

[62] D. Nawarathna, T. Turan, H. K. Wickramasinghe, *Applied physics letters* **2009**, *95*, 083117.

[63] A. L. Thangawng, M. A. Swartz, M. R. Glucksberg, R. S. Ruoff, *small* **2007**, *3*, 132.

[64] A. L. Thangawng, R. S. Ruoff, M. A. Swartz, M. R. Glucksberg, *Biomedical microdevices* **2007**, *9*, 587.

[65] G. Giraud, R. Pethig, H. Schulze, G. Henihan, J. G. Terry, A. Menachery, I. Ciani, D. Corrigan, C. J. Campbell, A. R. Mount, *Biomicrofluidics* **2011**, *5*, 024116.

[66] Y. Tao, H. Kumar Wickramasinghe, *Applied Physics Letters* **2017**, *110*, 073701.

[67] J. M. Rosano, N. Tousi, R. C. Scott, B. Krynska, V. Rizzo, B. Prabhakarpandian, K. Pant, S. Sundaram, M. F. Kiani, *Biomedical microdevices* **2009**, *11*, 1051.

[68] I. Wagner, E.-M. Materne, S. Brincker, U. Süßbier, C. Frädrich, M. Busek, F. Sonntag, D. A. Sakharov, E. V. Trushkin, A. G. Tonevitsky, *Lab on a Chip* **2013**, *13*, 3538.

[69] E. A. Punnoose, S. K. Atwal, J. M. Spoerke, H. Savage, A. Pandita, R.-F. Yeh, A. Pirzkall, B. M. Fine, L. C. Amler, D. S. Chen, *PloS one* **2010**, *5*, e12517.

[70] A. Roussidis, A. Theocharis, G. Tzanakakis, N. K. Karamanos, *Current medicinal chemistry* **2007**, *14*, 735.

[71] T. Stonehouse, V. Woodhead, P. Herridge, H. Ashrafian, M. George, B. Chain, D. Katz, *Immunology* **1999**, *96*, 35.

[72] T. Lorenzi, A. Turi, M. Lorenzi, F. Paolinelli, F. Mancioli, L. La Sala, M. Morroni, P. Ciarmela, A. Mantovani, A. L. Tranquilli, *PloS one* **2012**, *7*, e35232.

[73] P. Karagiannis, J. Singer, J. Hunt, S. K. Gan, S. M. Rudman, D. Mechtcheriakova, R. Knittelfelder, T. R. Daniels, P. S. Hobson, A. J. Beavil, *Cancer immunology, immunotherapy* **2009**, *58*, 915.

[74] E. R. Thomsen, J. K. Mich, Z. Yao, R. D. Hodge, A. M. Doyle, S. Jang, S. I. Shehata, A. M. Nelson, N. V. Shapovalova, B. P. Levi, *Nature methods* **2015**, *13*, 87.

[75] C. Y. Jin, M. H. Han, S. S. Lee, Y. H. Choi, *Biomedical microdevices* **2009**, *11*, 1195.

[76] M. C. Ramello, E. B. Haura, D. Abate-Daga, *Pharmacological research* **2017**.

[77] H. Yin, R. L. Kanasty, A. A. Eltoukhy, A. J. Vegas, J. R. Dorkin, D. G. Anderson, *Nature Reviews Genetics* **2014**, *15*, 541.

[78] T. Geng, Y. Zhan, J. Wang, C. Lu, *nature protocols* **2011**, *6*, 1192.

[79] D. W. Pack, A. S. Hoffman, S. Pun, P. S. Stayton, *Nature reviews Drug discovery* **2005**, *4*, 581.

[80] F. Labat-Moleur, A.-M. Steffan, C. Brisson, H. Perron, O. Feugeas, P. Furstenberger, F. Oberling, E. Brambilla, J. Behr, *Gene therapy* **1996**, *3*, 1010.

[81] A. L. Parker, C. Newman, S. Briggs, L. Seymour, P. J. Sheridan, *Expert reviews in molecular medicine* **2003**, *5*, 1.

[82] K. A. Mislick, J. D. Baldeschwieler, *Proceedings of the National Academy of Sciences* **1996**, *93*, 12349.

[83] M. Belting, P. Petersson, *Journal of Biological Chemistry* **1999**, *274*, 19375.

[84] P. Ross, S. Hui, *Gene therapy* **1999**, *6*.

[85] M. R. Almofti, H. Harashima, Y. Shinohara, A. Almofti, W. Li, H. Kiwada, *Molecular membrane biology* **2003**, *20*, 35.

[86] B. Ma, S. Zhang, H. Jiang, B. Zhao, H. Lv, *Journal of Controlled Release* **2007**, *123*, 184.

[87] J. P. Yang, L. Huang, *Gene Therapy* **1998**, *5*, 380.

[88] K. K. Son, D. H. Patel, D. Tkach, A. Park, *Biochimica et Biophysica Acta (BBA)-Biomembranes* **2000**, *1466*, 11.

[89] A. T.-H. Hsieh, N. Hori, R. Massoudi, P. J.-H. Pan, H. Sasaki, Y. A. Lin, A. P. Lee, *Lab on a Chip* **2009**, *9*, 2638.

[90] A. Colosimo, A. Serafino, F. Sangiuolo, S. Di Sario, E. Bruscia, P. Amicucci, G. Novelli, B. Dallapiccola, G. Mossa, *Biochimica et Biophysica Acta (BBA) - Biomembranes* **1999**, *1419*, 186.

[91] S.-Y. Teh, R. Lin, L.-H. Hung, A. P. Lee, *Lab on a Chip* **2008**, *8*, 198.

[92] A. Sharei, J. Zoldan, A. Adamo, W. Y. Sim, N. Cho, E. Jackson, S. Mao, S. Schneider, M.-J. Han, A. Lytton-Jean, *Proceedings of the National Academy of Sciences* **2013**, *110*, 2082.

[93] H. Song, M. R. Bringer, J. D. Tice, C. J. Gerdts, R. F. Ismagilov, *Applied Physics Letters* **2003**, *83*, 4664.

[94] H. C. Shum, A. R. Abate, D. Lee, A. R. Studart, B. Wang, C. H. Chen, J. Thiele, R. K. Shah, A. Krummel, D. A. Weitz, *Macromolecular rapid communications* **2010**, *31*, 108.

[95] S. Xu, Z. Nie, M. Seo, P. Lewis, E. Kumacheva, H. A. Stone, P. Garstecki, D. B. Weibel, I. Gitlin, G. M. Whitesides, *Angewandte Chemie* **2005**, *117*, 734.

[96] P. D. Hsu, E. S. Lander, F. Zhang, *Cell* **2014**, *157*, 1262.

[97] A. L. Markey, S. Mohr, P. J. Day, *Methods* **2010**, *50*, 277.

[98] J. Rejman, G. Tavernier, N. Bavarsad, J. Demeester, S. C. De Smedt, *Journal of Controlled Release* **2010**, *147*, 385.

[99] J. Wang, J. Wang, L. Feng, T. Lin, *RSC advances* **2015**, *5*, 104138.

[100] D. J. Collins, A. Neild, A.-Q. Liu, Y. Ai, *Lab on a Chip* **2015**, *15*, 3439.

[101] E. W. Kemna, R. M. Schoeman, F. Wolbers, I. Vermes, D. A. Weitz, A. Van Den Berg, *Lab on a Chip* **2012**, *12*, 2881.

[102] J. F. Edd, D. Di Carlo, K. J. Humphry, S. Köster, D. Irimia, D. A. Weitz, M. Toner, *Lab on a Chip* **2008**, *8*, 1262.

[103] G. Kamalakshakurup, A. P. Lee, *Lab on a Chip* **2017**, *17*, 4324.

[104] P. L. Felgner, In *Gene Transfer and Expression Protocols*, Eds: Murray, E. J., Humana Press: Totowa, NJ **1991**, pp 81.

[105] I. S. Zuhorn, V. Oberle, W. H. Visser, J. B. Engberts, U. Bakowsky, E. Polushkin, D. Hoekstra, *Biophysical journal* **2002**, *83*, 2096.

[106] Z. Du, M. M. Munye, A. D. Tagalakis, M. D. I. Manunta, S. L. Hart, *Scientific Reports* **2014**, *4*, 7107.

[107] M. R. Bringer, C. J. Gerdts, H. Song, J. D. Tice, R. F. Ismagilov, *Philosophical Transactions of the Royal Society of London A: Mathematical, Physical and Engineering Sciences* **2004**, *362*, 1087.

[108] C. N. Baroud, F. Gallaire, R. Dangla, *Lab on a Chip* **2010**, *10*, 2032.

[109] L. Jiang, Y. Zeng, H. Zhou, J. Y. Qu, S. Yao, *Biomicrofluidics* **2012**, *6*, 012810.

[110] D. M. Hallow, R. A. Seeger, P. P. Kamaev, G. R. Prado, M. C. LaPlaca, M. R. Prausnitz, *Biotechnology and bioengineering* **2008**, *99*, 846.

[111] X. Han, Z. Liu, M. c. Jo, K. Zhang, Y. Li, Z. Zeng, N. Li, Y. Zu, L. Qin, *Science Advances* **2015**, *1*.

[112] F. Schakowski, P. Buttgereit, M. Mazur, A. Märten, B. Schöttker, M. Gorschlüter, I. G. Schmidt-Wolf, *Genetic vaccines and therapy* **2004**, *2*, 1.

[113] J. A. Doudna, E. Charpentier, *Science* **2014**, *346*, 1258096.

[114] S. Panier, S. J. Boulton, *Nature reviews Molecular cell biology* **2014**, *15*, 7.

[115] M. Zimmermann, T. de Lange, *Trends in cell biology* **2014**, *24*, 108.

[116] S. Hong, Q. Pan, L. P. Lee, *Integrative biology* **2012**, *4*, 374.

[117] D. T. Scadden, *Nature* **2006**, *441*, 1075.

[118] C. Barnhart, *Journal of the advanced practitioner in oncology* **2015**, *6*, 234.

[119] J. Grosche, V. Matyash, T. Möller, A. Verkhratsky, A. Reichenbach, H. Kettenmann, *Nature Neuroscience* **1999**, *2*, 139.

[120] J.-P. Frimat, M. Becker, Y.-Y. Chiang, U. Marggraf, D. Janasek, J. G. Hengstler, J. Franzke, J. West, *Lab on a Chip* **2011**, *11*, 231.

[121] B. Dura, S. K. Dougan, M. Barisa, M. M. Hoehl, C. T. Lo, H. L. Ploegh, J. Voldman, *Nature communications* **2015**, *6*, 5940.

[122] J. W. Nichol, S. T. Koshy, H. Bae, C. M. Hwang, S. Yamanlar, A. Khademhosseini, *Biomaterials* **2010**, *31*, 5536.

[123] S. Agrawal, A. Agrawal, B. Doughty, A. Gerwitz, J. Blenis, T. Van Dyke, B. Pulendran, *The Journal of Immunology* **2003**, *171*, 4984.

[124] B. Everts, E. J. Pearce, *Frontiers in immunology* **2014**, *5*, 203.

[125] X. Qiu, T. M. Westerhof, A. A. Karunaratne, E. M. Werner, P. P. Pourfard, E. L. Nelson, E. E. Hui, J. B. Haun, *Lab on a Chip* **2017**, *17*, 3300.

[126] W.-H. Tan, S. Takeuchi, *Proceedings of the national academy of sciences* **2007**, *104*, 1146.

[127] Z. Zhu, O. Frey, D. S. Ottoz, F. Rudolf, A. Hierlemann, *Lab on a Chip* **2012**, *12*, 906.

[128] H. S. Kim, T. P. Devarenne, A. Han, *Lab on a Chip* **2015**, *15*, 2467.

APPENDIX A. MATHEMATICAL THEORY OF PHASOR-FLIM

Mathematic explanation of the phasor-FLIM approach

The fluorescence lifetime data are acquired in the time domain for every pixel (i, j) of the image, and Fourier-transformed by the two following equations:

$$g_{i,g}(\omega) = \frac{\int_0^\infty I_{i,j}(t)cos(\omega t)dt}{\int_0^\infty I_{i,j}(t)dt} \quad \text{(E1)}$$

$$s_{i,g}(\omega) = \frac{\int_0^\infty I_{i,j}(t)sin(\omega t)dt}{\int_0^\infty I_{i,j}(t)dt} \quad \text{(E2)}$$

where $g_{i,g}(\omega)$ and $s_{i,g}(\omega)$ are the x and y coordinates of the pixel's fluorescence lifetime decay data in the phasor plot; and $\omega = 2\pi f$ where f is the laser frequency (i.e., 80 MHz in our experiment). Therefore, every possible lifetime can be mapped into a specific point in the semicircle of the phasor plot.

For a single exponential fluorescence lifetime decay $I(t)=Ae^{-t/\tau}$, which is the case for many pure chemicals, e.g., pure NADH, its phasor coordinates are

$$g(\omega) = \frac{1}{1+(\omega\tau)^2} \quad \text{(E3)}$$

$$s(\omega) = \frac{\omega\tau}{1+(\omega\tau)^2} \quad \text{(E4)}$$

where τ is the decay lifetime and ω is the laser frequency. All single exponential lifetimes lie on the 'universal circle', defined as the semicircle going from (0, 0) to (1, 0), with a radius of 1/2. Point (0, 0) corresponds to $\tau = \infty$, and point (1, 0) corresponds to $\tau = 0$. Single-lifetime components can be added directly in the phasor coordinates as the phasor follows the vector algebra. Therefore, a mixture of two distinct single-lifetime components, each of which lies separately on the semicircle, lies along the line joining the two lifetime points (inside the semicircle).

As for a system with multiple fluorescent components, like a cell, the overall decay is a phasor that is the sum of the independent phasors of each fluorescence component:

$$G(\omega) = \sum_1^n f_n \, g_n(\omega) \qquad \text{(E5)}$$

$$S(\omega) = \sum_1^n f_n \, s_n(\omega) \qquad \text{(E6)}$$

where f_n is the fractional contribution of each component (g_n, s_n). A mixture of two multi-exponential decay species, i.e., two specific phasor points inside the semicircle, lies along the line joining the two points. Similarly, a mixture of three species locates inside a triangle connecting the three points, and etc.

Mathematic explanation of the multiparametric separation scheme

While WBCs were distinguished from leukemia cells by the average (*g,s*) values of each single cells' phasor plot, different types of leukemia cells were not fully separated through this simple approach, and there lacked of a quantitative description. To achieve a more precise and quantitative separation, the 2D phasor plot of each cell was viewed as a 3D phasor distribution by adding the counts of phasor points at each (*g,s*) location as the *z* axis. As illustrated in Fig. A1a and b, the phasor histogram was split in four equidistance segments based on the height of the peak, and the average (*g,s*) values were calculated in each segment, generating a spectrum of 8 parameters.

When separating two cell populations, T (test) and C (control), a training set was established, where each cell k has a spectrum *f(i,k)* consisted of 8 parameters. For every cell in the T group, its deviation from the average spectrum of the two groups was calculated by:

$$DT_T(k) = \sum_i \left(T_{av}(i) - f(i,k)\right)^2 w(i)/8 \qquad \text{(E7)}$$

$$DT_C(k) = \sum_i \left(C_{av}(i) - f(i,k)\right)^2 w(i)/8 \qquad \text{(E8)}$$

The same calculation was performed for each cell in the C group to get DC_T and DC_C. The weights *w(i)* for each parameter varied from 0 to 1 and were normalized so that the sum was a constant. The *w(i)* were used to emphasize which parameter was more important to achieve a better separation, and a quantity, Distance (D), was built to determine *w(i)* by minimization algorithm:

$$\mathrm{D} = \min\left[\sum_k \left(DT_T(k) + \frac{1}{DT_C(k)} + DC_C(k) + \frac{1}{DC_T(k)}\right)\right] \qquad \text{(E9)}$$

If *w(i)* = 0, the corresponding parameter did not influence D. If *w(i)* = 1, it had a maximum influence. This algorithm found parameter combinations to minimize the distance between the cells of one group from the group average and maximize the distance from the other group's average. After minimization, we got the values of the weights that best separated the two cell populations of the training set. An unknown sample was loaded to the training set, and its position was obtained using the separation index SI defined as:

$$SI(k) = 10 \times \frac{\left(DX_C(k) - DX_T(k)\right)}{\left(DX_C(k) + DX_T(k)\right)} \qquad \text{(E10)}$$

where X was the measurement of the unknown. In explain, if X was equal of the average of C group, then SI = -10; while if it was equal to the average of T group, then SI = +10. An SI histogram was plotted to determine if a cell was a true positive (below 0, same as the C group) or false positive (above 0, fell into the T group). Statistical methods such as the area-under-the-curve (AUC) values were used to determine the quality of the training set.

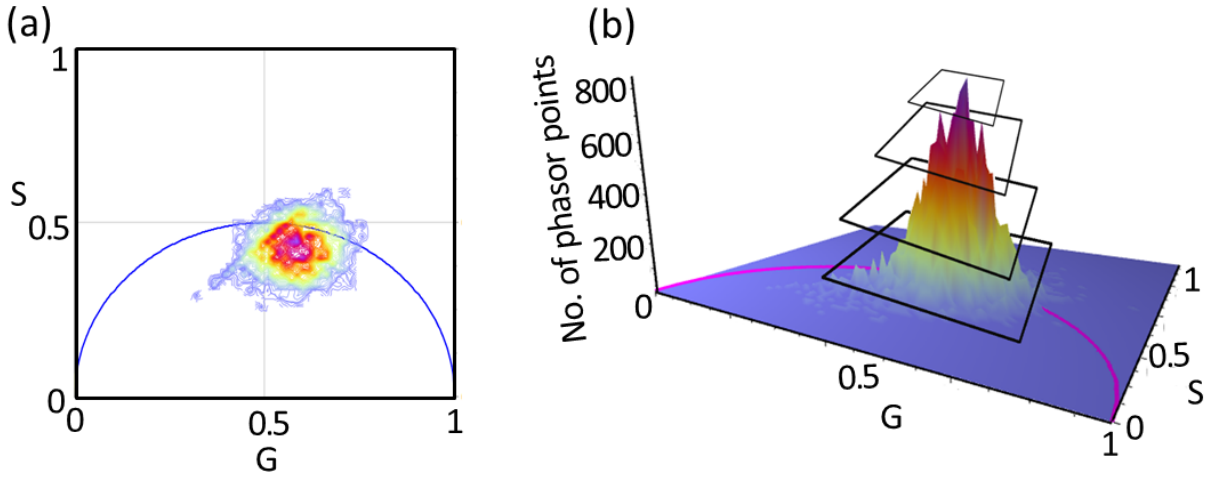

Figure A1 Transforming a 2D phasor plot into a 3D phasor distribution plot.
The phasor points in the 2D phasor heatmap (a) was plotted in a 3D format (b) where the count of phasor points at each (g, s) location was added as the z axis. The 3D phasor distribution was split in four equal height segments, and the average g and s values at each segments were calculated to collect a total of 8 parameters.

APPENDIX B. SETUP AND CHARACTERIZATION OF IN SITU MRNA PROBING

Standard curves used in RT-qPCR calibration

The absolute number of extracted mRNAs under an applied voltage from 1.1 to 1.9 Vpp was calculated based on the Ct values of the RT-qPCR experiment and the standard curves (Fig. B1), and the mRNA capturing efficiency at different probing voltages was compared with the standard cell-lysing mRNA extraction method (Fig. B2).

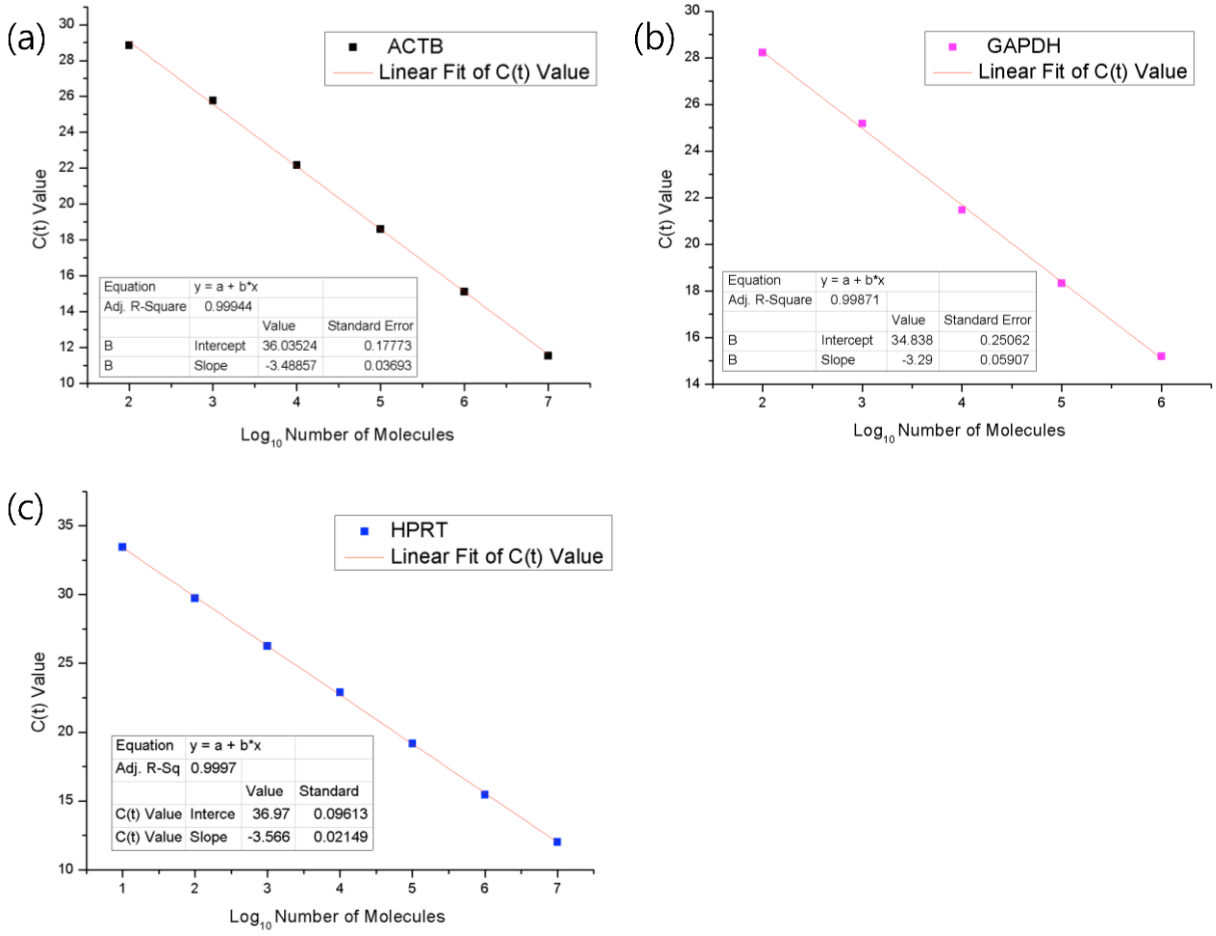

Figure B1 Standard curves used in RT-qPCR calibration.
The standard curves used to calibrate the absolute number of captured mRNA molecules for ACTB (a), GAPDH (b), and HPRT (c) were made using synthetic oligomers with the sequences of target genes' amplicons diluted in series as templates.

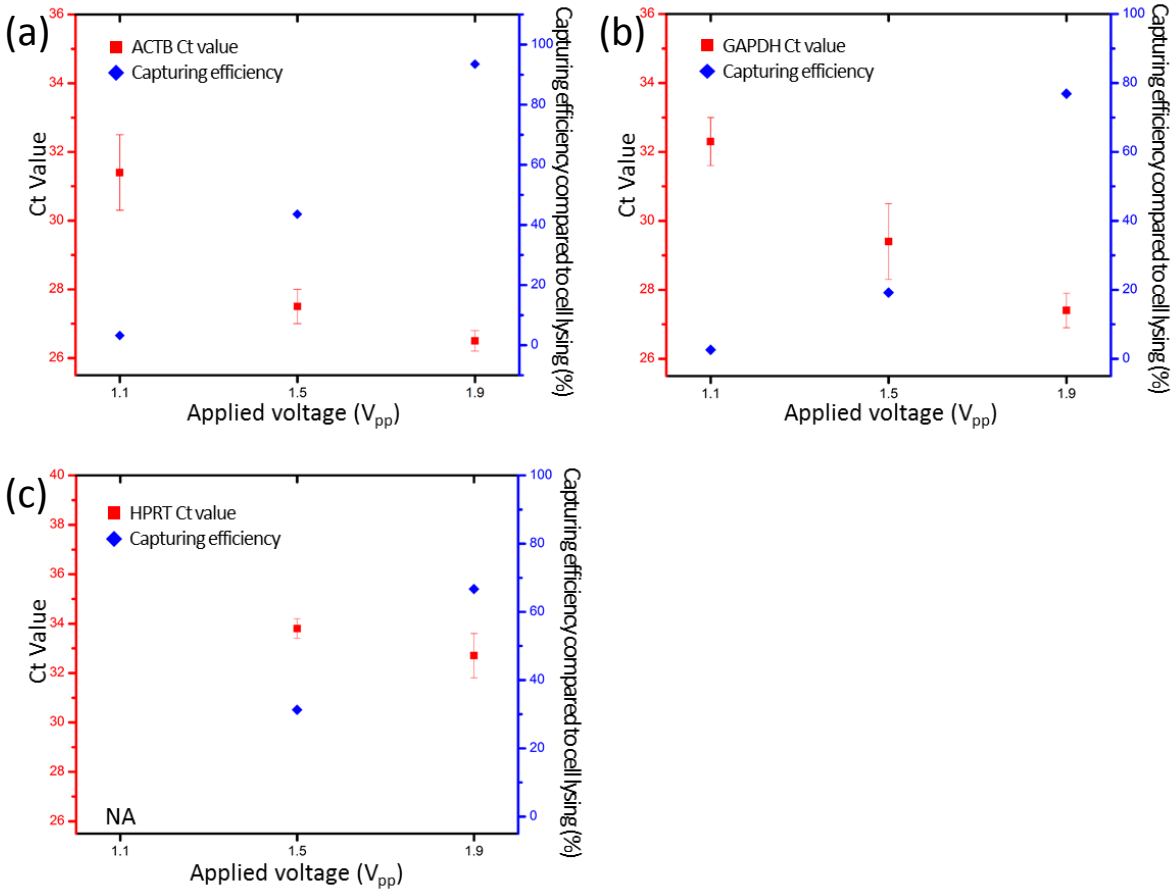

Figure B2 mRNA capturing efficiency at different probing voltages compared with the standard cell-lysing mRNA extraction method.
mRNAs extracted from bulk cell lysates using the cell-lysing RNA extraction kit (ISOLATE II RNA Mini Kit, Bioline) were diluted to a concentration of 10 cells' mRNA molecules per 5 µL distilled water, and were quantified following the same RT-qPCR process to derive the single-cell Ct values. The calculated ΔCt values at different probing voltages were used to calculate the capturing efficiency for the three housekeeping genes: ACTB (a), GAPDH (b), and HPRT (c).

Mechanically cutting the Au-coated tip-end to expose the inner Si core

Firstly, the Au-coated tip was placed in contact with the surface of a piece of Si_3N_4 wafer fixed on top of the AFM piezo scanner, with a contact force (set point) of 30 pN and a contact spot very close (≤ 90 µm) to the edge of the Si_3N_4 wafer. Secondly, the Si_3N_4 wafer was displaced away from its original position by controlling the AFM piezo scanner to move for 90 µm, so that the tip was no longer in contact with the Si_3N_4 wafer surface but was hanging in the air. This resulted in the relaxation of the AFM probe with no bending, thus the height of tip-end

was slightly below the wafer surface. In the final step, the wafer was moved back to its original position, during which the tip-end hit the edge of the wafer and was chopped along the wafer surface, exposing the inner silicon core. As we could control the amount of initial probe bending by controlling the contact force (set point), the relative height difference between the tip-end and the wafer surface after probe relaxation was also precisely controlled. We could therefore achieve relatively consistent exposure of the inner silicon core with a width ranging from 200 nm to 400 nm.

Microscopic setup of the integrated microfluidic-nanoprobing platform

The experimental setup of the integrated microfluidic-nanoprobing platform is shown in Fig. B3.

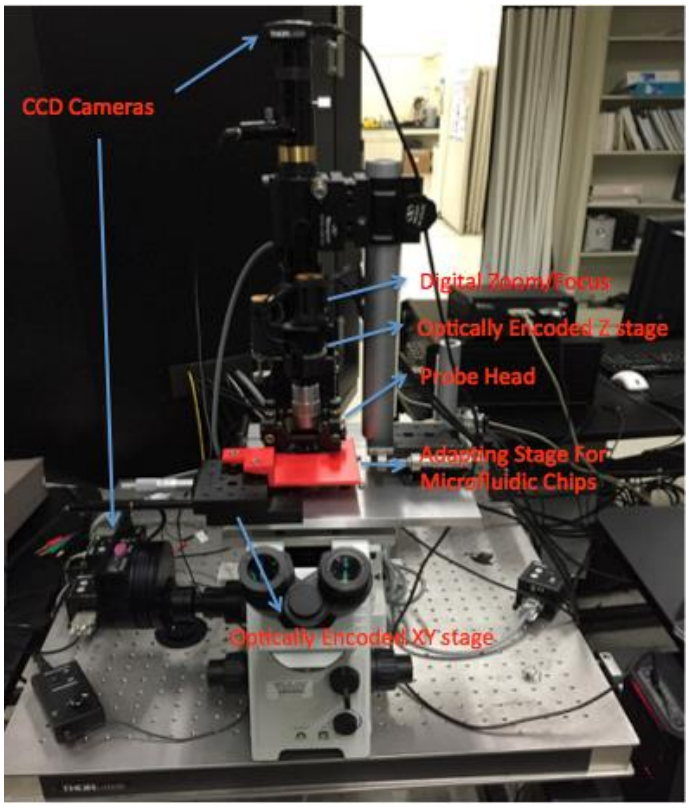

Figure B3 Microscopic setup of the integrated microfluidic-nanoprobing platform.

APPENDIX C. SUPPLEMENTARY ANALYSIS FOR DROPLET TRANSFECTION

Definition of the EGFP transfection efficiency

To compensate for auto-fluorescence, surface binding, and endocytosis, K562, THP-1, Jurkat, and HeLa cells were transfected with pcDNA3.1 plasmid, a vector without any fluorescence protein-encoding sequences, following the standard lipofection protocol as the negative control, and analyzed via flow cytometry 48 hr after transfection. The sample fluorescence intensity vs. normalized cell-count frequency histograms of the 4 types of cells in the negative control group were shown in Fig. C1a through d. The EGFP transfection threshold (vertical line in the histogram) was defined such that less than 1% of cells in the negative control fell into the effective EGFP transfection region (unshaded region) in the histogram. The EGFP transfection efficiency of a sample thus corresponded to the percentage of live cells that were in the effective transfection region.

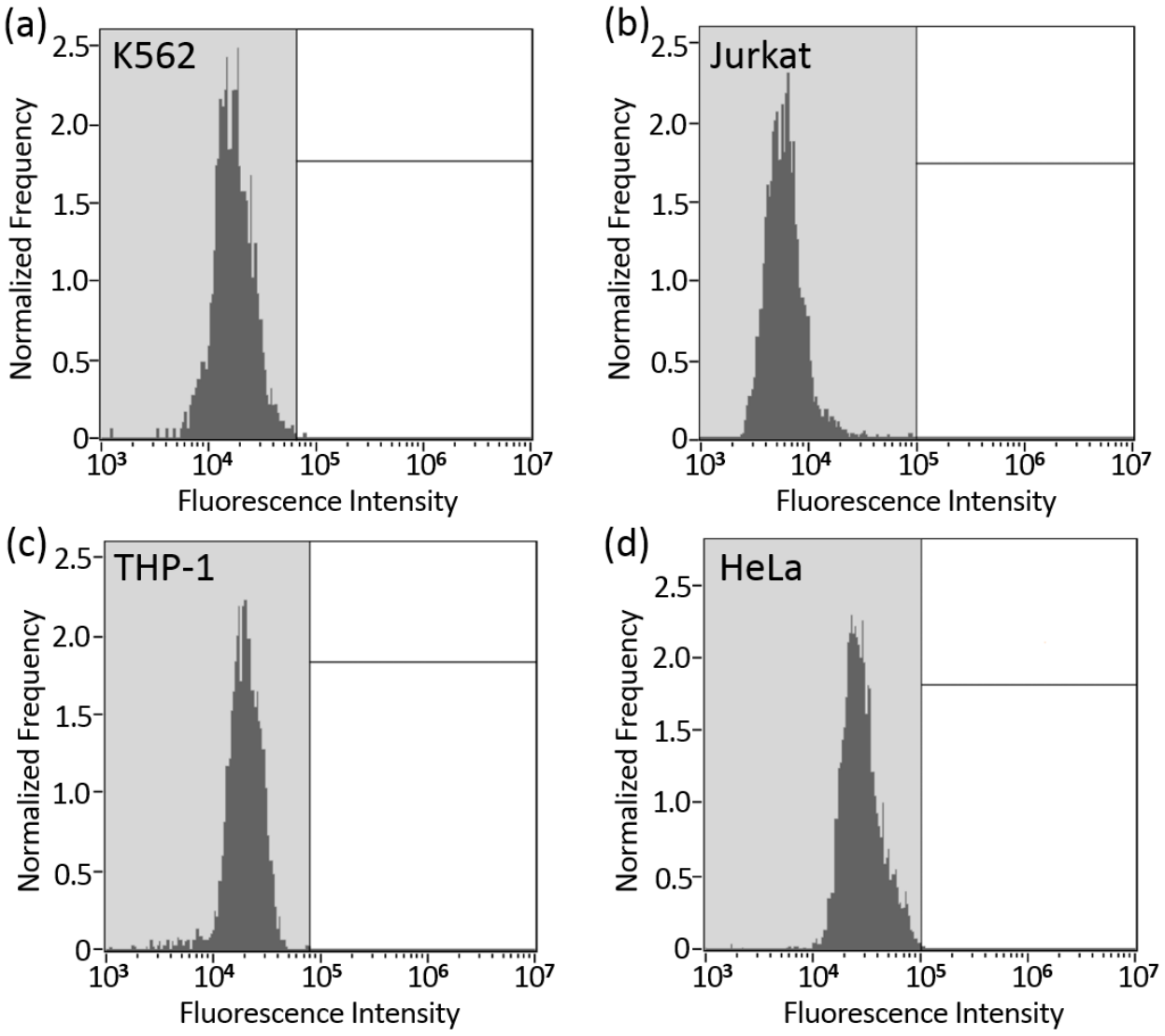

Figure C1 Fluorescence intensity histograms (from flow cytometry) of K562 (a), THP-1 (b), Jurkat (c), and HeLa (d) cells in the negative control group.

Droplet lipofection using a straight mixing channel

To compare the lipofection efficiency via droplet chaotic mixing in winding channel with droplet mixing in straight channel, our platform was modified so that the original winding channel was replaced by a straight channel of equal length for droplet mixing (Fig. C2a) after the co-encapsulation of single cells, plasmids and Lipofectin, K562 cells were transfected with pcDNA3-EGFP plasmids using this modified droplet-lipofection platform (Fig. C2b).

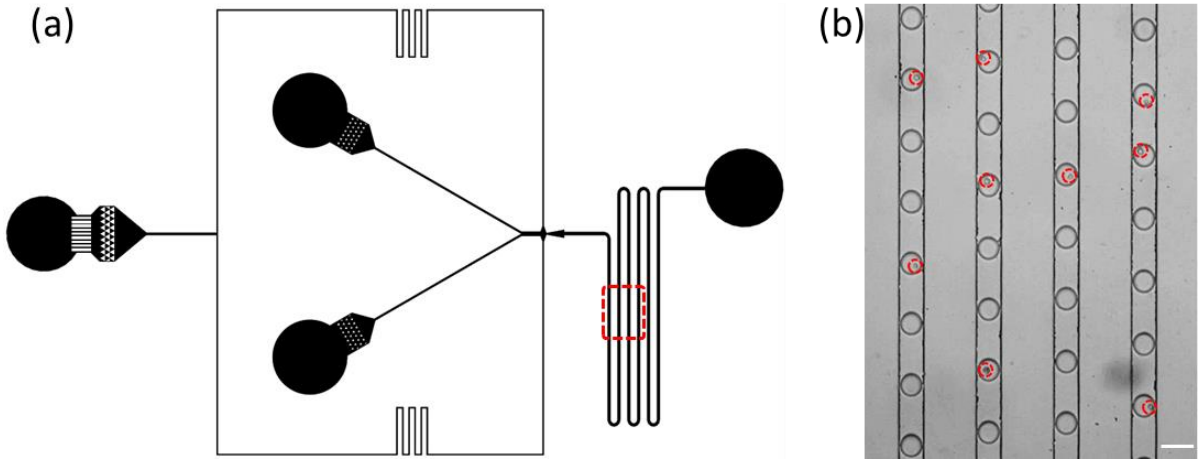

Figure C2 Design of the droplet-lipofection platform with a straight mixing channel (a) and droplets encapsulating single K562 cells + lipoplexes running through this straight channel. Scale bar: 100 μm.

Droplet lipofection of HeLa cells

To evaluate our platform's performance on adherent cells, which are easier to transfect compared to suspension cells, we ran HeLa cells through our droplet-lipofection device to transfect them with the same pcDNA3-EGFP plasmid. As shown in the flow cytometry histogram (Fig. C3a), there was a clear shift towards a higher fluorescence intensity from the bulk-lipofection group to the droplet-lipofection group. The average transfection efficiency of HeLa cells (Fig. C3b) using droplet lipofection was 75.5±4.6%, which was higher than using the conventional bulk lipofection protocol (35.1±3.6%).

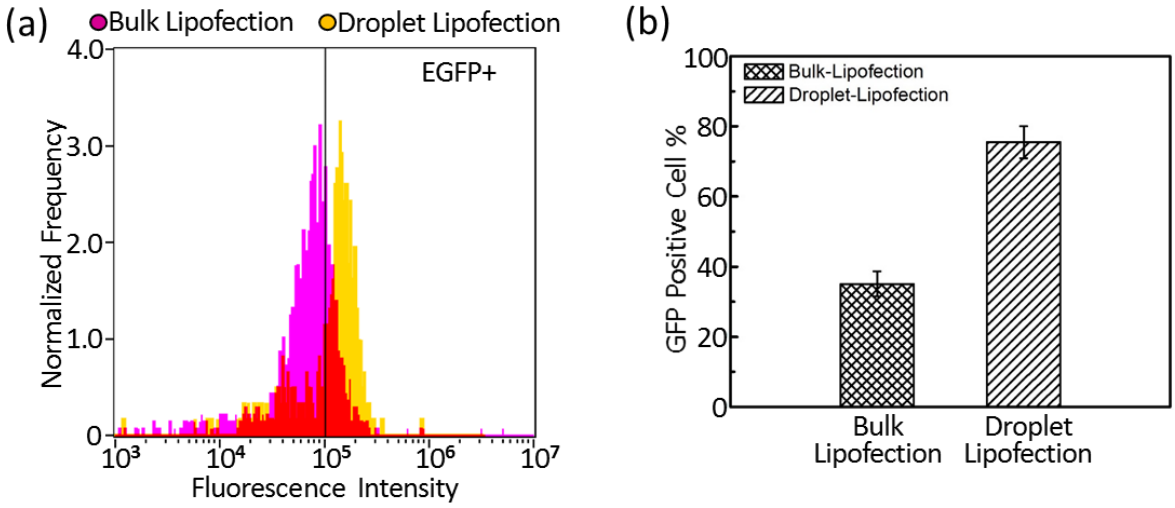

Figure C3 Fluorescence intensity vs. normalized cell-count frequency histograms (a) and the average EFGP transfection efficiencies (b) of HeLa cells transfected via droplet lipofection and conventional bulk lipofection.

RT-qPCR of K562 cells after TP53BP1 knockout

We repeated the RT-qPCR experiment three times to compare the TP53BP1 knockout efficiency between droplet lipofection and bulk lipofection. The qPCR amplification curves of the three repeats were plotted in Fig. C4a to c. DNA oligomer (Integrated DNA Technologies) with the same sequence as the target TP53BP1 amplicon was diluted in series to construct the standard curve (Fig. C4d) for calibrating the absolute molecule numbers from RT-qPCR results: the correlation between the absolute number of TP53BP1 mRNA molecules (n), and the Ct value is: Log10n = (41.35-Ct)/3.59. For every 1,000 single K562 cells analyzed 48 hr after initial plasmid delivery, the Ct value was 31.3±0.2 for the non-transfected group, 31.8±0.3 for the bulk-lipofection group, and 33.9±0.6 for the droplet-lipofection group. Upon calibration using the standard curve, the corresponding copy number of target mRNA molecules was 630±61 for the non-transfected group, 457±83 for the bulk-lipofection group, and 119±51 for the droplet-lipofection group. Therefore, the estimated TP53BP1 knockout efficiency through the delivery of pLentiCRISPR.v2-sgTP53BP1 plasmid was 27±13% when using bulk lipofection, and 81±8% when using droplet lipofection. However, as the Cells-to-CT™ 1-Step Power SYBR® Green Kit was used for this experiment, in which cell lysing, mRNA extraction and RT-qPCR were all integrated into one assay, there was unavoidable loss of mRNA molecules during cell lysing and mRNA extraction, which caused an over-estimation of gene knockout efficiency.

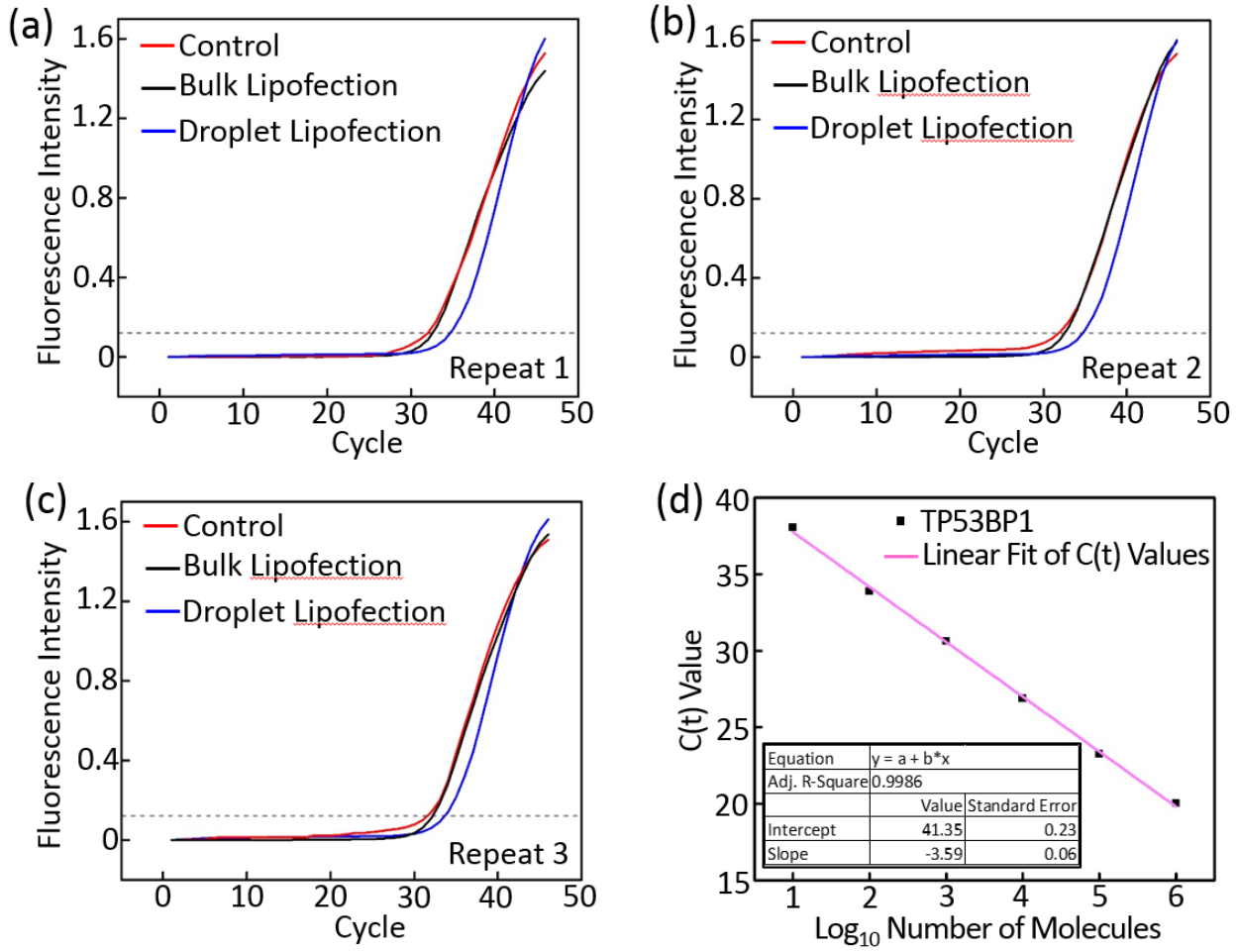

Figure C4 RT-qPCR results for analyzing the knockout efficiency of TP53BP1 in K562 cells via the CRISPR/CAS9 mechanism. (a ~ c) The RT-qPCR amplification curves of every 1,000 K562 cells after TB53BP1 knockout by either droplet lipofection (blue) or bulk lipofection (black) in three repeating experiments. The Ct value of the bulk-lipofection group was very close to that of the non-transfected group (red), whereas the Ct value of the droplet-lipofection group was significantly higher, indicating a higher efficiency of gene-knockout. (d) The standard curve for calibrating the absolute number of TP53BP1 mRNA molecules.

Annotated sequence maps

The annotated sequence maps of the pcDNA3-EGFP plasmid and the pLentiCRISPR.v2-sgTP53BP1 plasmid were plotted using SnapGene program, and shown in Fig. C5a and b, respectively.

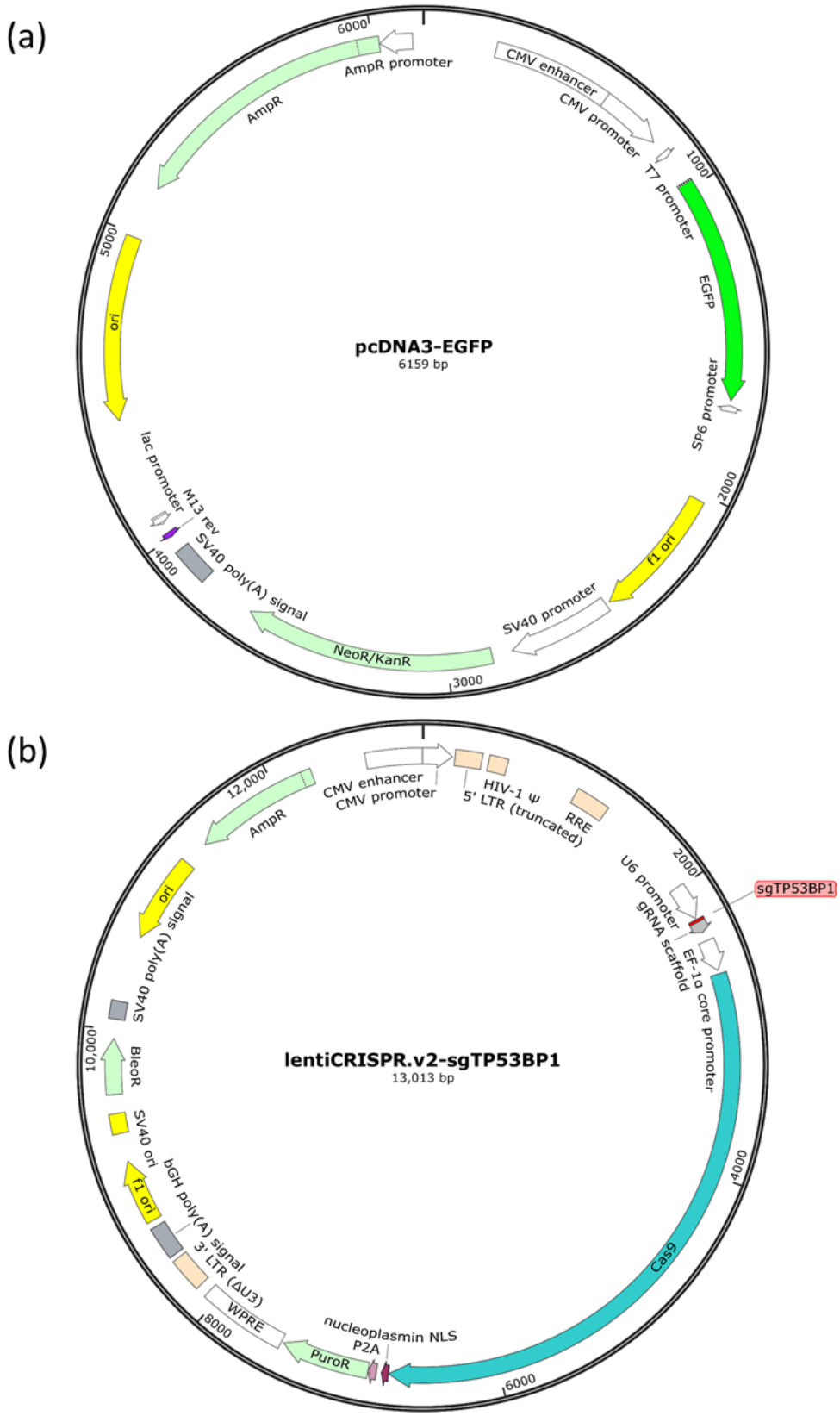

Figure C5 Annotated sequence maps of the pcDNA3-EGFP plasmid (a) and the pLentiCRISPR.v2-sgTP53BP1 plasmid (b).

APPENDIX D. DETAILED DESCRIPTION OF THE MOVIES

Movie 2.1 Trap 100 HeLa cells in the single-cell array.

Real-time video recording the trapping of 100 single HeLa cells in the ultra-thin membrane-sealed microfluidic array.

Movie 2.2 Simultaneous CTC/WBC trapping and RBC filtration.

Real-time recording of the isolation of single cancer cells and WBCs at a flow rate of 0.2 mL/h. The zoom-in video demonstrates the removal of RBCs via the gap area taken using a high-speed camera. The gap area makes the perpendicular flow to deform and migrate RBCs, while WBCs and leukemia cells can be pushed into traps, and the combination of perpendicular deformation and horizontal delivery flow enables the continuous blood cell filtration process.

Movie 4.1 *In situ* mRNA probing from a HeLa cell by DENT.

Real-time video recording the extraction of mRNA molecules from a trapped single HeLa cell using the modified AFM nanoprobe (DENT) via dielectrophoresis.

Movie 5.1 Co-encapsulation of single K562 cells, cationic lipids, plasmids.

Co-encapsulation of single K562 cells with cationic lipids and plasmids in monodisperse picoliter-droplets. The video was taken using Phantom high-speed camera at 10× magnification at a speed of 600 pictures-per-second, and played at a speed of 10 pictures-per-second.

Movie 5.2 Chaotic advection of droplets in the winding channel.

Chaotic advection of the droplets encapsulating single cells and lipoplexes in the winding channel. The video was taken using Phantom high-speed camera at 10× magnification at a speed of 600 pictures-per-second, and played at a speed of 10 pictures-per-second.

Movie 5.3 Cell deformation when passing the droplet pinch-off.

Squeezing and deformation of a K562 cell when it passed through the droplet pinch-off. The video was taken using Phantom high-speed camera at 40× magnification at a speed of 45,000 pictures-per-second, and played at a speed of 20 pictures-per-second.

Movie 5.4 Simulation of the shear stress at the droplet pinch-off.

Numerical simulation of the shear stress at the droplet pinch-off during flow-focusing droplet generation.